END-LAUNCHED COAXIAL AND MICROSTRIP TO PARTIAL H-PLANE WAVEGUIDE ADAPTERS

by

Kevin Hugh Kloke

Submitted in partial fulfilment of the requirements for the degree
Master of Engineering (Electronic Engineering)

in the

Department of Electrical, Electronic and Computer Engineering
Faculty of Engineering, Built Environment and Information Technology

UNIVERSITY OF PRETORIA

February 2014

SUMMARY

END-LAUNCHED COAXIAL AND MICROSTRIP TO PARTIAL H-PLANE WAVEGUIDE ADAPTERS

by

Kevin Hugh Kloke

Supervisor: Prof. J. Joubert

Co-Supervisor: Prof. J.W. Odendaal

Department: Electrical, Electronic and Computer Engineering

University: University of Pretoria

Degree: Master of Engineering (Electronic Engineering)

Keywords: Partial H-plane waveguide, microstrip adapter, waveguide transition, coaxial adapter, S-parameters, T-parameters.

Conventional rectangular waveguides are commonly used for high power and millimetre wave microwave applications. However their use at lower frequencies has been limited by their bulky nature at these frequencies. A new type of compact waveguide called a partial H-plane waveguide has previously been proposed that has only one quarter of the cross sectional area of a conventional waveguide. However, only limited information relating to the feeding of such waveguides is available.

This study focuses on the development of a practical end-launched coaxial and a microstrip to partial H-plane waveguide adapters with similar or larger achievable bandwidths compared to conventional waveguide probe feed adapters. The two proposed waveguide transition geometries are investigated to determine which parameters can be used to optimise the insertion and return losses. The prototype waveguide transitions were optimised using numerous simulations and fabricated in the back-to-back configuration. Simulated single ended and back-to-back S-parameters yield good performance over the entire H-band (3.95 to 5.85 GHz, also known as G-Band). De-embedding techniques are used to measure the approximate single ended response of the two waveguide adapters based on the back-to-back measurements. The measurement and simulation results compare favourably and validate the designs.

OPSOMMING

ENTGELANSEERDE KOAKSIALE- EN MIKROSTROOK- NA GEDEELTELIKE H-VLAK GOLFLEIEROORGANGE

deur

Kevin Hugh Kloke

Studieleier: Prof. J. Joubert

Mede-studieleier: Prof. J.W. Odendaal

Departement: Elektriese, Elektroniese en Rekenaaringenieurswese

Universiteit: Universiteit van Pretoria

Graad: Magister in Ingenieurswese (Elektroniese Ingenieurswese)

Sleutelwoorde: Gedeeltelike H-vlak golfleier, mikrostrook-aansluiting, golfleieroorgang, koaksiale-aansluiting, S-parameters, T-parameters.

Konvensionele reghoekige golfleiers word in die algemeen gebruik vir hoë drywing en millimetergolf-toepassings. Die gebruik van sulke golfleiers word beperk deur hulle fisiese grootte by lae frekwensies. ‘n Nuwe tipe kompakte golfleier, wat ‘n gedeeltelike H-vlak golfleier genoem word, is voorheen voorgestel, en beslaan net een kwart van die deursnit-area van die konvensionele golfleier. Ongelukkig is daar net beperkte inligting beskikbaar oor voermeganismes vir sulke golfleiers.

Hierdie studie handel oor die ontwikkeling van praktiese ent-gelanseerde koaksiale- en mikrostrook- na gedeeltelike H-vlak golfleieroorgange met gelykstaande of hoër bandwydtes met verwysing tot oorgange na konvensionele reghoekige golfleier. Die twee voorgestelde golfleieroorgange word ondersoek om te bepaal watter parameters gebruik kan word om die invoerverlies en weerkaatsverlies te optimeer. Die prototipe golfleieroorgange is geoptimeer deur gebruik te maak van verskeie simulasies en deur vervaardiging van ‘n rug-aan-rug konfigurasie. Gesimuleerde enkel-eindpunt en rug-aan-rug S-parameters het goeie werkverrigting oor die hele H-band (3.95 tot 5.85 GHz, ook bekend as G-Band) getoon. Ontkoppelingstegnieke is gebruik om die benaderde enkelweergawe van die twee golfleieroorgange te onttrek, gebaseer is op die rug-aan-rug metings. Die ooreenstemming tussen die metings en die simulasies is goed genoeg om die geldigheid van die ontwerp te bevestig.

ACKNOWLEDGEMENT

I would like to firstly thank the Lord for his guidance and strength that made this work possible. Secondly this dissertation would not have been completed without the support and understanding of my family.

My sincere thanks and gratitude are expressed towards my supervisors, Prof. Joubert and Prof. Odendaal for their insight, guidance and endless patience whilst conducting this research. In addition I would like to thank my internal examiner Prof. Malherbe and external examiner Prof. Williamson for making themselves available to examine my dissertation and for providing invaluable feedback and comments during the examination process.

I would also like to acknowledge the support shown to me by my colleagues at the CSIR and their encouragement whilst undertaking this research. Lastly I would like to express my appreciation to the National Research Foundation and University of Pretoria for their financial support to conduct this research.

TABLE OF CONTENTS

CHAPTER 1 INTRODUCTION

1.1 PROBLEM STATEMENT

1.1.1 Context of the problem

Conventional rectangular waveguides are commonly used for microwave applications including high power and millimetre wave applications [1]. Their widespread use at lower frequencies has however been limited by their bulky nature. A new type of compact waveguide called a partial H-plane waveguide has been proposed [2] that has only one quarter of the cross sectional area of a conventional waveguide. This new type of compact waveguide opens up numerous possibilities to use waveguides at lower frequencies where they could not be used previously due to space and weight limitations. However, only limited information relating to the feeding of such waveguides has been published.

1.1.2 Research gap

Often in microwave systems that employ waveguides there exists a need at some point to transition to and from waveguide and coaxial transmission mediums. The establishment of well defined end-launched coaxial and microstrip solutions could facilitate more wide spread use of the new compact partial H-plane waveguide in two ways. Firstly there only exists very limited information on partial H-plane waveguide to coaxial adapters; therefore this research will provide a well defined transition structure for the first time. Secondly since the one proposed adapter is end-launched it provides collinear advantages over the probe feeds which have been previously used [3].

As mentioned above the use of waveguide systems at lower frequencies has been limited by their bulky nature. Through the use of partial H-plane waveguides it is possible to reduce the required cross-sectional area by a factor of 4. This reduction will facilitate light weight and low cost microwave systems. Lastly substrate integrated waveguides can be used at lower frequencies since partial H-plane substrate integrated waveguides have a much lower cut-off frequency than conventional substrate integrated waveguides [4].

However, the current lack of suitable coaxial adapters has limited the widespread use of this compact waveguide in practice.

1.2 HYPOTHESIS AND APPROACH

1.2.1 Hypothesis

End-launched coaxial and microstrip to partial H-plane waveguide adapters can be developed with similar or larger achievable bandwidths compared to conventional probe feed adapters.

1.2.2 Approach

A literature study should be performed to determine the current knowledge base on partial H-plane waveguide coaxial and microstrip adapters, and conventional waveguide to microstrip and coaxial end-launchers. From the literature study it should be possible to propose a suitable end-launcher and microstrip structures which can be modified for the partial H-plane waveguide case. Once suitable partial H-plane structures have been identified a commercial full-wave electro-magnetic simulator will be used to simulate the performance of the adapters. Starting with the simplest adapter geometry a spiral development process will be followed to evaluate the achievable performance before increasing the complexity of the adapters to achieve the desired insertion and return loss results. This approach is followed as the final solutions should be practical and easy to manufacture. Once suitable final adapter geometries have been developed a parametric study will be conducted to determine the sensitivity and influence on input impedance of the various adapter components. Given the results of the parametric study the designs should be optimised to be realisable prototypes with mechanical constraints in mind, whilst still achieving reasonable performance. Lastly the prototypes should be manufactured and characterised. This will verify the designs and allow comparisons to the results obtained by Kim and Lee [3] using their probe feed.

1.3 RESEARCH GOALS

The ultimate research goal is the development of a practical coaxial end-launched and microstrip to partial H-plane waveguide adapters. Secondly the adapters should have similar or improved usable bandwidths compared to conventional probe feeds. Additionally a parametric study will determine which parameters (physical dimensions and material properties) affect the real or imaginary parts of the impedance and thus influence the achievable bandwidth.

1.4 RESEARCH CONTRIBUTION

Currently very limited information exists on coaxial and microstrip to partial H-plane waveguide adapters. Thus developing an end-launched coaxial adapter for this new type of compact waveguide will greatly supplement existing knowledge by not only providing a well defined adapter, but one with additional collinear advantages. The collinear nature of the end-launcher allows the compact nature of the partial H-plane waveguide to be maximally exploited; an example is inline filters. Additionally the end-launched feed avoids the need for connectors and cables on the radiating face of slot radiators, which prevents pattern degradation. In addition to the SMA end-launcher a microstrip adapter is also developed to enable close integration with other planar microwave components such as integrated circuits. Facilitating close integration of microwave components facilitates compact systems with reduced losses and lower noise figures.

Developing well defined end-launched coaxial and microstrip adapters for the partial H-plane waveguides could facilitate more widespread use of this new type of compact waveguide. Through the use of partial H-plane waveguides it is possible to reduce the required cross-sectional area by a factor of 4. This reduction could help realise light weight low cost microwave systems. An example could be a compact, low cost mobile 3D search radar antenna. Additionally substrate integrated waveguides can be used at lower frequencies since partial H-plane substrate integrated waveguides have a much lower cut-off frequency than conventional substrate integrated waveguides [5].

1.5 OVERVIEW OF STUDY

This chapter has provided context for the dissertation and set the objectives and research goals which will be discussed in the following chapters. The contributions to the field have also been briefly outlined.

Chapter 2 reports on the findings of a literature study aimed at finding published data on partial H-plane waveguides in general, and known feeding mechanisms. The literature study also identifies suitable conventional (rectangular) waveguide feeds that can be adapter for the partial H-plane waveguide's geometry and symmetry.

Chapter 3 details the requirements for and development of the end-launched coaxial to partial H-plane waveguide adapter. The incremental development of the feed geometry is discussed as the design evolved to satisfy the design criteria. The results of the parametric study are presented along with the final prototype's dimensions. The final simulated and measured results for the end-launcher are given and discussed.

Chapter 4 has a similar structure to Chapter 3 but details the development and results of the microstrip to partial H-plane waveguide adapter.

Chapter 5 concludes the dissertation with a summary of the study, results and conclusions. Lastly suggestions for future research are given based on the insights gained during this dissertation.

CHAPTER 2 LITERATURE STUDY

2.1 CHAPTER OBJECTIVES

This chapter presents a review of partial H-plane waveguides, conventional rectangular waveguide feeds, and existing partial H-plane waveguide coaxial feeds. Additionally conventional waveguide feed structures are identified that should be adaptable for use in partial H-plane waveguides.

2.2 PARTIAL H-PLANE WAVEGUIDES

Inspired by folded waveguides Kim and Lee [2] have proposed a new type of compact waveguide called a Partial H-plane waveguide. The partial H-plane waveguide is a rectangular waveguide with a reduced height that is transversely folded flat once, which results in a quarter reduction in the cross sectional area of the waveguide. Additionally partial H-plane waveguides also have attractive low cost and mass-producible properties [3] which more complex [6], [7] folded waveguides do not have.

The first two modes of a partial H-plane waveguide can have the same dispersion characteristics as those of a conventional rectangular waveguide [2]. This allows the same usable bandwidth as a rectangular conventional waveguide to be achieved. However an interesting feature of the partial H-plane structure is that the first two modes can be separately controlled if required for different applications [8]. The electric-field distribution of dominant $TE_{0(01)}$ mode is given in figure 2.1 (a) below [2].

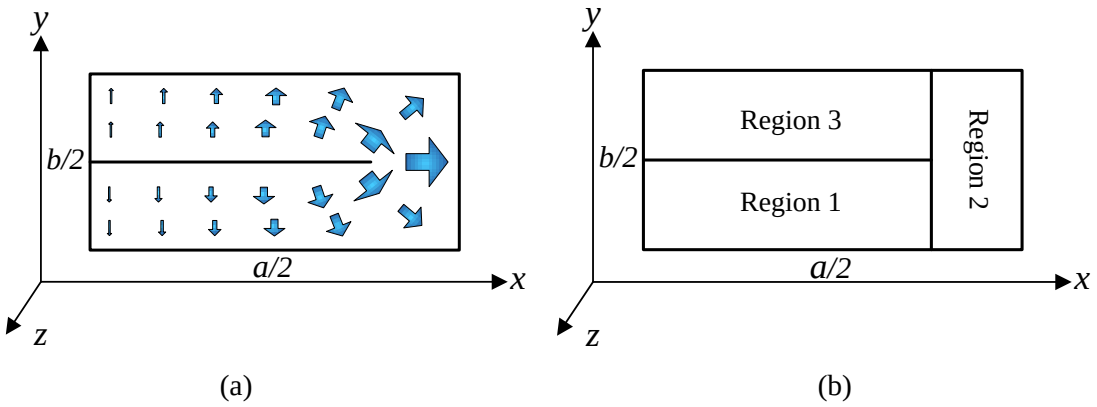

(a) (b)

Figure 2.1. Electric-field distribution of the $TE_{0(01)}$ dominant mode in a partial H-plane waveguide (a) and cross sectional regions (b) of a partial H-plane waveguide.

By dividing the partial H-plane waveguide into three sections as shown in figure 2.1 (b), analytic expressions for the electric and magnetic field distributions have been derived [2] based on the assumption that the metal vane is very thin. Additionally a suitable mode indexing scheme for the partial H-plane waveguides with the $TE_{l(m,n)}$ format has been defined [2]. Where *l* is the number of sinusoidal half-cycle variations in the x-direction of the entire structure, *m* is the number of variations in the y-direction of region 1 and *n* is the number of variations in the y-direction of region 2. Kim and Lee validated their field derivations by calculating the cut-off frequency by deriving equations 2.1-2.3 below [2] and comparing the results to a FDTD (Finite Difference Time Domain) simulation. The calculated results compared well with the simulated results and confirmed that the dispersion characteristics of first two modes are the same as in a conventional rectangular waveguide.

$$f_C = \frac{c}{2\pi}\sqrt{\beta_{x1}{}^2 + \left(\frac{2m\pi}{b}\right)^2} \qquad (\mathrm{m} = 0, 1, 2, \ldots), \qquad (2.1)$$

where c is the speed of light in free space and β_{x1} is calculated using equations 2.2 and 2.3.

$$\beta_0{}^2 = \beta_{x1}{}^2 + \left(\frac{2m\pi}{b}\right)^2 = \beta_{x2}{}^2 + \left(\frac{n\pi}{b}\right)^2 = \omega^2\mu_0\varepsilon_0 \qquad (\mathrm{m} = \mathrm{n} = 0, 1, 2, \ldots), \qquad (2.2)$$

where β_0 is the free space propagation constant, β_{x1} and β_{x2} are the phase constants for regions 1 and 2 respectfully in the *x* direction, ω is the radian frequency, μ_0 and ε_0 are the permeability and permittivity in free space.

$$-\beta_{x1}\tan(\beta_{x1}d) = \beta_{x2}\tan(\beta_{x2}(a-d)) \qquad (2.3)$$

The compact nature of the partial H-plane waveguide has facilitated the practical implementation of compact, lightweight and low cost waveguide filters [3], [9]-[12], substrate integrated folded waveguide filters [4], [5], [13] and high gain slot antennas [14]-

[16] at lower microwave and RF (Radio Frequency) frequencies. Unfortunately only limited published information exists on the subject of feeding these waveguides.

2.3 PARTIAL H-PLANE WAVEGUIDE ADAPTERS

The first published information related to coaxial to partial H-plane waveguide adapters was published in 2005 [3] where it was mentioned that a probe was inserted into a rectangular cut-out in the H-plane vane approximately a quarter wavelength from the end of the waveguide. However no drawings or dimensions of the adapter geometry were given. The probe adapter was mentioned again in [9] with geometry and dimensions given in 2006 [10]. Figure 2.2 shows the geometry given in a photo in [10] with dimension definitions. The adapter consists of a commercially available SMA (Sub-Miniature A) connector with extended dielectric and centre conductor. This forms the probe inserted into the cut-out of depth *de* and width *wi* in the H-plane metal vane. The adapter was optimised using a commercial full wave simulator (CST Microwave Studio) where the cut-out width *wi* and depth *de* were varied to minimise the insertion and maximise the return losses.

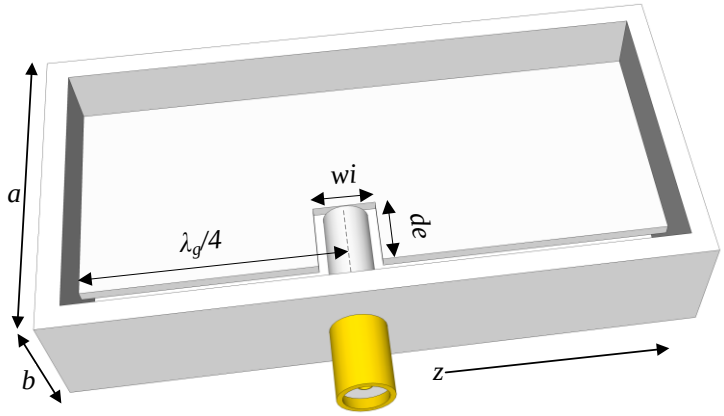

Figure 2.2. Probe adapter geometry.

The dimensions *a* and *b* in the figure are the standard waveguide definitions for width and height and are shown together with the propagation direction *z* for context. By unfolding the partial H-plane waveguide one can easily verify that the probe feed described above is equivalent to the classical probe feed used in conventional rectangular waveguides. It is interesting to note that a cut-out in the vane is required to achieve resonance. In [16] the probe adapter was used to feed an S-Band slot array antenna; it was noted that having the coaxial cable and connectors on the radiating face causes pattern degradation (increased

side lobe levels). The probe adapter's insertion and return losses were simulated using CST Microwave Studio given the dimensions in [10]. The resulting scattering parameters are given in figure 2.3. An ideal waveguide port was used as the second port to facilitate simulating the insertion loss.

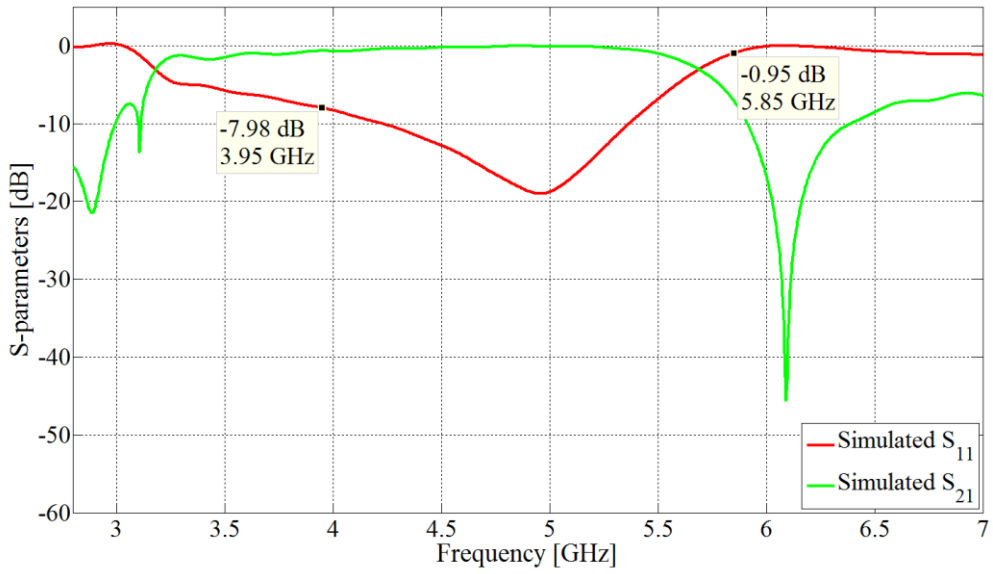

Figure 2.3. Simulated S-parameters of partial H-plane waveguide probe adapter.

From figure 2.3 it is clear that the adapter was optimised for operation around 5 GHz which is expected since the filter designed in [10] had a centre frequency of 5GHz. The insertion loss is 0.1 dB and return loss is 19 dB at 5 GHz. This was acceptable for the narrowband filter in [10] but may not be suitable for more general purpose wideband applications.

Also in 2005, a shielded stripline to substrate integrated folded waveguide (SIFW) adapter based on the partial H-plane waveguide adapter was published in [5]. The geometry of the feeding structure is shown in figure 2.4. As in figure 2.2 the direction of propagation is in the *z* direction and *a* is the waveguide width. Note that the standard waveguide dimension *b* is not shown in the figure, as it only shows the internal layer in the SIFW containing the H-plane vane, and is therefore an incomplete representation of the total waveguide height.

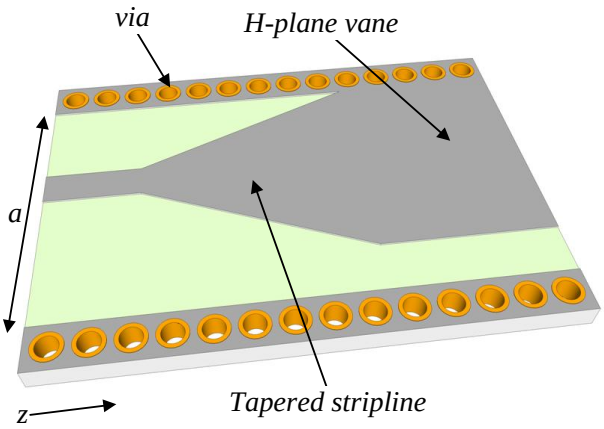

Figure 2.4. Shielded stripline to substrate integrated waveguide adapter.

Figure 2.4 is an internal layer of the multilayer SIFW in [5] showing the feed geometry, which consists of a tapered stripline which transitions from the stripline on the left to the H-plane vane on the right. The vias in the figure above form the sides of the SIFW and the ends which are not show in the figure. The back-to-back insertion and return losses were measured and found to be approximately 2.3 dB and 10.8 dB respectively [5]. The authors attribute the high insertion loss to not de-embedding the SMA adapters required to obtain the measurements. The SIFW transition in figure 2.4 was refined in [13] where it was used in a novel folded multilayer SIFW structure to construct an X-band bandpass filter. Although this type of transition is naturally end-launched it was bent to the left and right in [13] as the input and output ports were on the same end of the modified SIFW in [13]. The simulated insertion loss is 0.6 dB and the simulated return loss was 11 dB [13]. Whilst the insertion loss is acceptable the return loss could be better. Similar adapters have been used in SIFW X-band filters in [4] and [17].

2.4 WAVEGUIDE ADAPTERS

In order for a waveguide to be useful in practical applications EM energy has to be coupled into and out of the waveguide [1]. Additionally as previously mentioned there often arises the need to transition between coaxial and waveguide transmission mediums. Therefore the discussion below will focus on coaxial adapters although numerous other adapters and transition techniques exist such as aperture coupling [1]; they are not considered here as coaxial adapters are one of the most widely used waveguide adapters. In theory it is

possible to excite only a specific waveguide mode though an ideal electric or magnetic current sheet extending across the waveguide aperture. However such ideal current sheets are not practically realisable which leads to the excitation of evanescent modes which present a reactive component to the input impedance as they store energy close to the feeding mechanism [1]. The two classic coaxial to waveguide transitions are the probe and small loop feeds shown in figure 2.5 and figure 2.6 respectively [18].

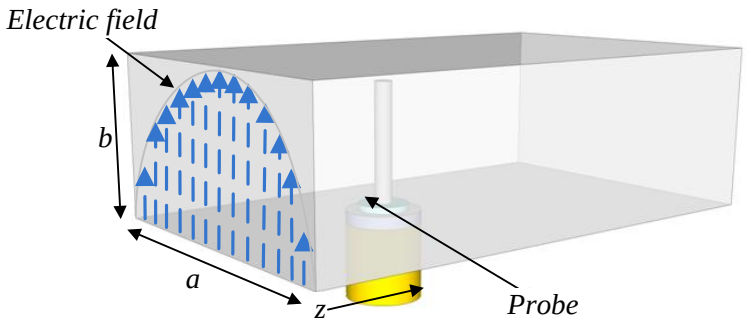

Figure 2.5. Classic probe feed geometry with Electric field indicated in blue.

The blue lines in figure 2.5 show the half sinusoidal electric field distribution; the probe is typically located along the centre line of the waveguide where the electric field is a maximum for the dominant mode [18]. The probe is located a quarter wave away from the shorting end of the waveguide ($z = 0$), this is to ensure that the wave reflected from the shorting wall does not cancel out the wave generated at the probe (they are in phase). The size and shape of the probe determines the bandwidth and power handling capacity, where thicker probes have a broader bandwidth and higher power capabilities [18].

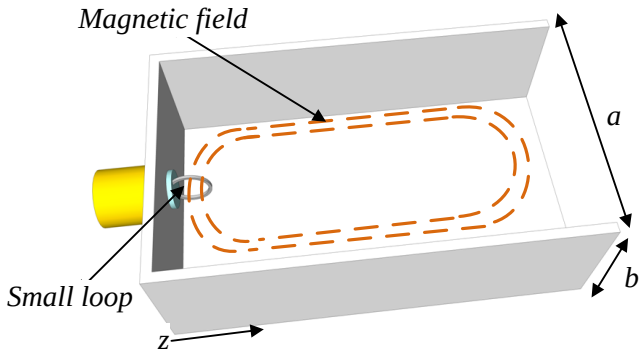

Figure 2.6. Classic small loop feed geometry with Magnetic field indicated in brown.

The small loop feed shown in figure 2.6 couples energy into waveguides by exciting a magnetic field within the waveguide whereas the probe feed excites an electric field [18].

Therefore the small loop is inserted into the waveguide where the magnetic field is at a maximum and electromagnetic energy is launched down the waveguide in the *z* direction. The diameter of the wire used to construct the loop determines the bandwidth and power handling capability of the coaxial transition. As in the probe feed larger wire diameters result in high power handling capacities and larger bandwidths. Approximate input impedance equations and graphs of input impedance against feed geometry dimensions for the classic probe and small loop feeds can be found in [19] and [20]. These equations for input impedance are rarely used in practise as they are limited to simple models that use thin probes or loops and are not accurate enough for general design use [20].

2.4.1 Practical Probe Feeds

Although the classic probe feed from the previous subsection has been adapted for use with partial H-plane waveguides [10] it is not ideal for general purpose applications as it is typically narrow band as shown in figure 2.3. Additionally the classic probe feed typically has usable bandwidths of less than 10% [21]. Percentage bandwidth is defined as the absolute bandwidth divided by the centre frequency. Therefore it is desirable to identify other possible adapter geometries that will offer a broader match whilst still being adaptable for the partial H-plane scenario. Three common methods of increasing the usable bandwidth of the classic probe are to shape the probe, dielectric coat the probe or introduce a tuning post [22]. One way of increasing the bandwidth of the classic probe is by shaping the probe is to taper the probe from a large diameter at the top to a smaller one at the connector as shown in figure 2.7 [18]. This type of probe feed is often referred to as the doorknob probe due to its similar shape to household doorknobs [18].

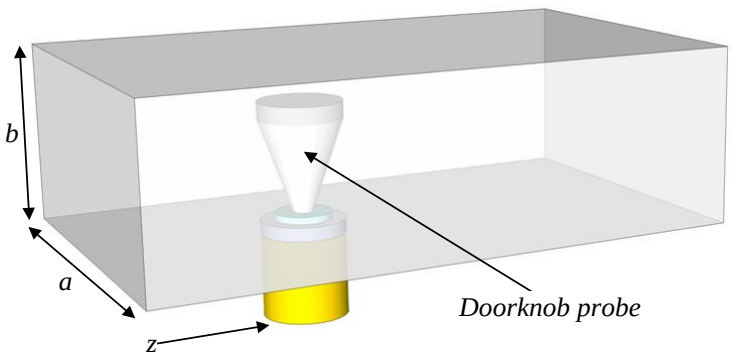

Figure 2.7. Doorknob probe feed.

The top loading of the doorknob probe enables broader band operation by cancelling some of the reactance components of the input impedance [23]. These top loaded transitions can achieve bandwidths of over 50% where the return loss is greater than 20 dB [23], [24]. Additionally these adapters can be used in reduced height waveguides [24] which makes them attractive for possible use in the partial H-plane waveguides. A similar broadband probe is the disc-ended probe which is a variant of the doorknob that contains the top part of the doorknob without the tapered section [22]. As previously mentioned the bandwidth of the classic probe can also be increased by coating the probe with a dielectric as shown in figure 2.8 below [25].

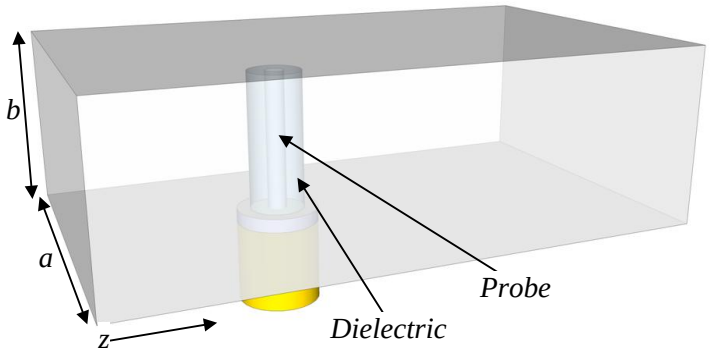

Figure 2.8. Dielectric coated probe adapter.

A maximum usable bandwidth of approximately 30 – 40% can be achieved with a dielectric coated probe feed [25]. Lastly the bandwidth of the classic probe can be extended by introducing a tuning post [26] as shown in figure 2.9.

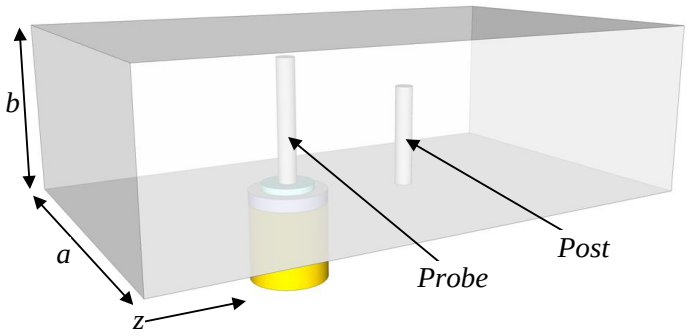

Figure 2.9. Coaxial to Waveguide probe adapter with tuning post.

If the length of the tuning post is short the shunt susceptance is capacitive and longer posts have an inductive effect [27]. The post can also achieve resonance when in the region of three quarters of the height in standard rectangular waveguide [27]. The resonance effect can be used to realise doubly tuned waveguide transitions with wider bandwidths than the classic probe feed [28].

2.4.2 Practical End Launchers

The classic small loop feed offers the attractive collinear advantages of an end-launcher but it has limited bandwidth. One way of increasing the bandwidth is to bend the centre conductor of the connector to join one of the broad walls, thus forming a coupling loop as shown in figure 2.10 [29].

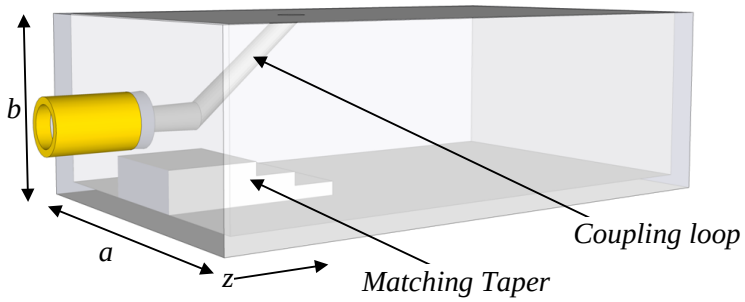

Figure 2.10. Tapered coupling loop end-launcher.

In order to achieve a match a tapered ridge is located underneath the coupling loop; due to manufacturing limitations the matching taper was realised with a stepped approximation in [29]. Ideally the matching section should be a smooth taper. The tapered coupling loop end-launcher in [29] achieved a bandwidth in excess of 30%. Unfortunately this adapter would be difficult to adapt to the partial H-plane waveguide scenario due to the limited available space between the H-plane vane and side wall. The most common end-launcher is the L-shaped loop [30] given in figure 2.11. Note that the L-shaped loop transition does not require the post for operation [30] and it is only used when wider bandwidths are required from a doubly tuned structure [28].

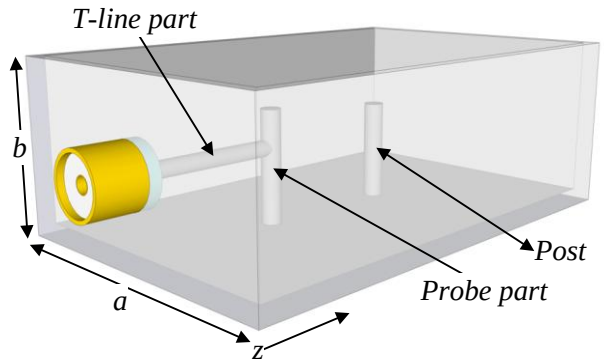

Figure 2.11. L-shaped loop with post.

The operation of the L-shaped loop is explained by the Probe Coupling Model in [30] where the L-shaped loop is broken into two parts, namely the transmission line (T-line part in figure 2.11) and probe part. The transmission line part is essentially a coaxial line with an offset rectangular outer conductor [30] which is similar to the well defined trough line [31]. A match can be achieved using three different methods; firstly the L-shaped loop can be move slightly off the centre line [30], the T-line part can be extended slightly beyond the probe part [32] and lastly the contact position of the transmission line and probe parts can be varied up and down the probe's length to achieve a match [28]. The resonant frequency of the probe part and post are controlled by their length and are typically different lengths to achieve an overall wideband match. The bandwidth achieved with the extended transmission line matching technique (no tuning post) is less than 5% [32]; with the offset feed geometry (no tuning post) a bandwidth of over 15% can be achieved [33]. Finally with the varied contact position of the transmission line and probe parts a typical bandwidth of more than 15% can be achieved with a single tuning post [28]. A novel end-launched method of coupling energy into a waveguide is to use a patch antenna inside the waveguide [34]. This is possible since most coaxial to waveguide transitions can be viewed as antennas inside of waveguides fed by coaxial lines [18]. A three dimensional representation of the patch fed end-launcher given in [34] is shown in figure 2.12.

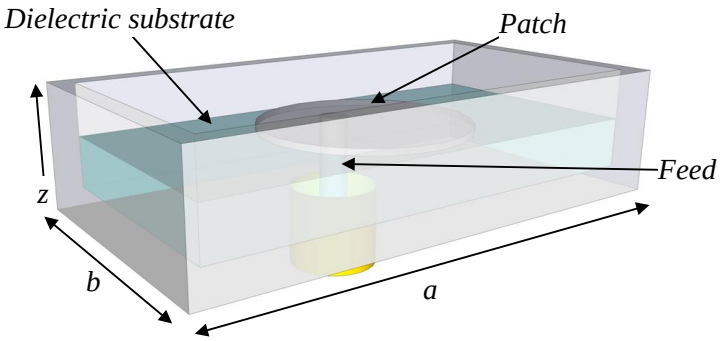

Figure 2.12. Patch fed end-launcher.

The end-launched patch feed in figure 2.12 consists of a coaxial connector feeding a circular patch above a dielectric substrate. An RT/Duroid substrate with a relative permittivity of 2.20 and a thickness of 1.575 mm was used in [34] for the X-band transition. The adapter in [34] achieved a bandwidth of 14% which is respectable considering that patch antennas are typically regarded as very narrow band antennas [35]. Note that the patch end-launcher is much more compact than the commonly used L-shaped loop which must be at least a quarter wavelength long and is even longer when a tuning post is included. Therefore the patch end-launcher is significantly more compact which offers additional advantages to the adapter.

Lastly note that the SIFW launcher in figure 2.4 is in fact also an end-launcher that directly couples energy from stripline into the SIFW partial H-plane waveguide. This SIFW adapter achieved a bandwidth of over 40% [5].

2.4.3 Microstrip

The microstrip transmission line is commonly used in microwave planar circuits; therefore adapters between microstrip lines and waveguides have previously been designed to facilitate interconnections between these two widely used transmission mediums [36]. Two microstrip launchers are discussed below, namely an end-launcher and broad side probe feed. Both of these waveguide transitions are based on the classic probe feed previously discussed. Figure 2.13 [36], gives the geometry of an end-launched microstrip to waveguide probe adapter. Note there is a small coaxial section between the inside of the

waveguide and microstrip substrate, this reduces insertion loss and facilitates realising hermetically sealed adapters which are useful in some applications [37].

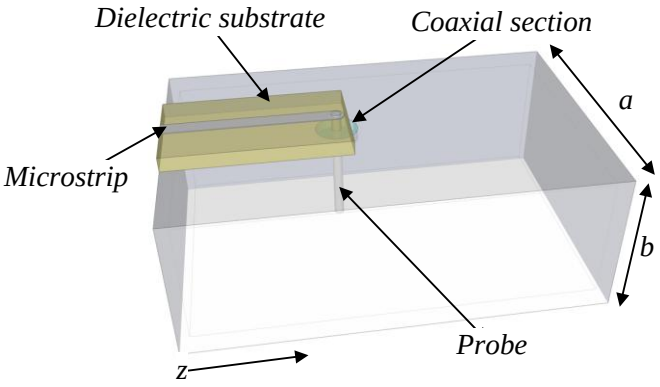

Figure 2.13. Microstrip probe adapter.

The probe is inserted approximately a quarter wavelength away from the back short and protrudes approximately half of the waveguide height (dimension b in the figure) into the waveguide [37]. The typical insertion loss for this type of adapter is given as 0.5 dB in [36] and [37] and the typical achievable bandwidth is approximately 12% [37]. The performance of this adapter is therefore comparable to the classic probe feed. Approximate input impedance equations for this type of microstrip transitions can be found in [37].

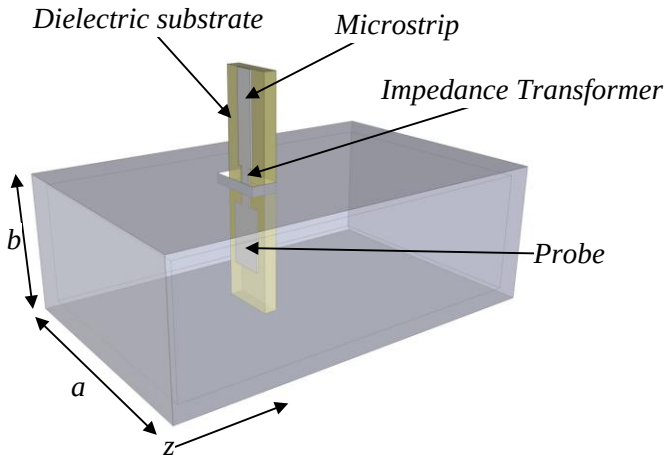

Figure 2.14. Integrated broadside microstrip adapter.

A broadside microstrip to waveguide adapter which is typically integrated with the rest of the microstrip circuit is shown in figure 2.14 [38]. This transition typically has a 40% bandwidth and a low insertion loss of less than 0.5 dB [38]. Note that the transition makes full use of the waveguide height (dimension *b*) to facilitate simple alignment during fabricat1ion [38]. The aperture size is kept as small as possible to keep its effect on the

field distribution inside the waveguide minimal whilst still achieving an acceptable insertion loss [38]. An impedance matching quarter wave transformer is located between the microstrip line and metallic probe that is supported by the substrate inside the waveguide [38]. This type of transition can also be fabricated using Low Temperature Co-fired Ceramic (LTCC) technology for compact Millimeter-wave applications [39]. A variant of the adapter given in figure 2.14 appears in [40] which has two impedance matching sections that yields a usable bandwidth of more than 40%.

2.5 INPUT IMPEDANCE CALCULATION

Input impedance is defined as the voltage divided by the input current for the dominant TEM mode at the input terminal of the waveguide transition [41]. It is desired to know the input impedance of waveguide adapters to ensure that there is a good match between the transition and the two transmission line mediums. A poor match results in reflection coefficients that reduce power delivered to and from the waveguide [27].

Three classic methods of deriving the input impedance for a waveguide transition are given below:

- The free space electric field resulting from the current in the probe can be expressed as a contour integral which is summed with a similar integral for another electric field that once summed satisfies the waveguide boundary equation [41]. The contour integrals are then evaluated and the input impedance given by the ratio of the electric field and input current [41].
- The total resulting electric field resulting from the superposition of the free space field resulting from the input current of the feed and the infinite number of images of this field resulting from reflections off of the waveguide walls [41].
- If the probe is thin the current on the probe can be considered equivalent to an infinitely thin current filament on the probe's axis which represents a discontinuity in the magnetic field that can be expressed by a series expansion of the magnetic field [41]. This series expansion is used to calculate the resulting electric field from the input current [41]. Once again the input impedance is calculated from the ratio between the electric field and input current [41].

The use of the word “probe” above is to represent the feeding element within the waveguide. The classic methods above can only give the real component of the input impedance when considering a transition placed a quarter wave from the shorting wall [41]. Their use in practise is therefore limited and the reactance has previously (before modern software packages) been determined empirically from experiments [32].

The classic methods described above and the input impedance equations given in [20] and [41] are difficult to modify for the partial H-plane waveguide scenario as they are derived for a rectangular waveguide cross section. A rectangular cross section represents a significantly simpler mathematical problem, when compared to the equations required to express the fields within the partial H-plane waveguide's geometry. Additionally these methods do not yield results that are sufficiently accurate for design purposes [32] and are not suitable for thick probes [42], which have superior bandwidths. This coupled with the advances in commercially available full wave electromagnetic software packages means that the substantial effort required to derive the input impedance for a partial H-plane waveguide adapter would be futile as the commercial software would yield superior results.

2.6 SIMULATION SOFTWARE

CST Microwave Studio (MWS) was selected as the EM simulation software for this study as it has native support [43] for waveguide ports and has previously been used with the partial H-plane waveguide geometry [3], [10], [14], [16], [17]. To facilitate simulated insertion loss results the concept adapters were terminated with ideal waveguide ports.

The time domain solver was utilised exclusively throughout this study as the results obtained compared well with those of the alternative frequency domain solver; however the time domain solver completed simulation tasks significantly faster than the frequency domain solver. Additionally the time domain solver allowed the accuracy of the simulations runs to easily be adjusted to facilitate rapid investigations where the final accuracy was not crucial, and later increased to verify the performance of the final concepts. In general an accuracy of -35dB was selected for the concept development

phases of the coaxial and microstrip transitions. For the parameter study the simulation convergence accuracies were set to -50dB for the coaxial case and -40dB for the microstrip case. Higher accuracies were required when performing the parameter study on the optimised designs which had return losses in excess of 35dB in certain instances. The microstrip prototype was simulated at an accuracy of -40dB instead of -50dB (like the coaxial case) as the microstrip geometry was represented by approximately five times the number of mesh cells and therefore would have taken significantly longer to also simulate at an accuracy of -50 dB. Additionally to reduce simulation times of both adapters, the lengths of waveguide between the prototype adapters and ideal waveguide ports was set to the minimum lengths that would yield consistent results with minimal effects from evanescent modes. Lastly multi-threading acceleration was also enabled to minimise simulation run times.

The background mediums were selected as perfect electrical conductor (PEC) and vacuum for the coaxial and microstrip adapters respectively. The PEC background simplifies the waveguide geometry in the coaxial case, but cannot be used in the microstrip case as the microstrip substrate would be short circuited if the background was PEC. The adapter geometries were meshed using the default Hexahedral mesh settings with the following changes from default settings, the lines per wavelength was increased from 10 to 18 to facilitate more accurate representation of the two feed geometries. Additionally the minimum step sizes were set to 0.05 and 0.01 mm for the coaxial and microstrip geometries respectively. It was empirically found that these values yielded consistent results that converged from the default more coarse settings. Note that the microstrip adapter geometry required a smaller minimum step size as the changes in microstrip line widths was more sensitive than other parameters in the coaxial geometry. Hence the microstrip adapter has five times the number of mesh cells as previously mentioned.

In summary the CST MWS solver settings were selected to yield consistently accurate results without unnecessarily increasing the time required to simulate the prototype adapters.

2.7 ADAPTER PERFORMANCE MEASUREMENT

This subsection describes the measurement setup and methodology that was used to characterise the performance of the prototype partial H-plane waveguide adapters. As stated above very limited information exists in open literature regarding partial H-plane waveguide transitions and certainly no commercially available adapters are available for measurements. Therefore for every prototype waveguide transition investigated in this study two adapters have to be fabricated to facilitate back-to-back measurements as vector network analysers (VNA) typically have coaxial terminals [44]. Whilst this measurement setup shown in figure 2.15 does facilitate measurements of the scattering matrix (S-parameters) it does not directly give the performance of the individual adapters.

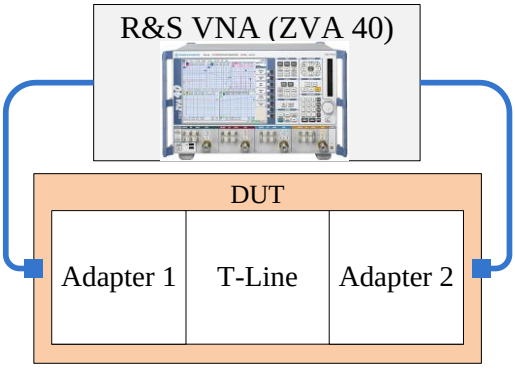

Figure 2.15. Measurement setup.

Figure 2.15 above shows that the two port VNA measurement of the device under test (DUT) is actually a measurement of the combined scattering matrix of the two adapters and a section of transmission line between them. Since this study is concerned with realising coaxial adapters for general use the single ended response of the individual adapters is desired as not all applications require two adapters, such as antennas. The process of extracting the approximate single ended response from the combined back-to-back is referred to as de-embedding as the single ended response is so-called “embedded” in the total response [45].

The intervening transmission line between the two adapters represents a known structure with scattering matrix given in equation 2.4 for a lossless line [47]. Note that the scattering matrix only depends on the propagation constant and length of the transmission line.

$$[S] = \begin{bmatrix} 0 & e^{-j\beta l} \\ e^{-j\beta l} & 0 \end{bmatrix} \tag{2.4}$$

Given the known transmission line scattering matrix, an equation for de-embedding the approximate single ended scattering matrices can be derived for a fixed length transmission line if the two prototype adapters are assumed to have approximately identical responses. Ideally multiple measurements with different lengths of intervening transmission lines could be used to yield the accurate individual S-parameters of the two transitions without having to assume that the two adapters have identical responses [44]. However this would require that multiple physical hardware prototypes would have to be realised (to achieve different lengths) which would drastically increase the cost of performing this study. Since this study only seeks to verify the simulation results with the measured response of the prototypes some inaccuracy due to this assumption can be tolerated. Since the two back-to-back transitions will be manufactured with identical dimensions and manufacturing techniques it is believed that the error induced by this assumption will be minimal.

The de-embedding equation can be derived using either the ABCD parameters or the transfer scattering matrix (T-parameters) [46], (also known as chain scattering parameters) [48]. The T-parameters are similar to the S-Parameters in that they also work with the voltages of waves reflected and transmitted at ports. However they can easily be cascaded to determine the result of a cascaded network, which is not possible to do directly with S-parameters [46]. The T-parameters are more suitable for de-embedding than the ABCD parameters as working with T-parameters does not require knowledge of the reference characteristic impedance [46]. This is beneficial as the characteristic impedance varies in the transition from coaxial and microstrip mediums to the partial H-plane waveguide medium. Equation 2.5 shows the form of the de-embedding equation using T-parameters to relate the measurements made with the VNA in figure 2.15 to the two adapter's T-parameters and length of the intervening transmission line.

$$[T_{VNA}] = [T_{adapter1}][T_{line}][T_{adapter2}] \tag{2.5}$$

The T-parameters can be related to the S-parameters using equations 2.6 to 2.9 below [46].

$$[T] = \begin{bmatrix} \frac{-\Delta S}{S_{21}} & \frac{S_{11}}{S_{21}} \\ \frac{-S_{22}}{S_{21}} & \frac{1}{S_{21}} \end{bmatrix}, \tag{2.6}$$

where ΔS is the determinant of the matrix as defined in equation 2.7 [46].

$$\Delta S = S_{11}S_{22} - S_{12}S_{21} \tag{2.7}$$

Equation 2.8 relates the S-parameters to the T-parameters [46].

$$[S] = \begin{bmatrix} \frac{T_{12}}{T_{22}} & \frac{\Delta T}{T_{22}} \\ \frac{1}{T_{22}} & \frac{-T_{21}}{T_{22}} \end{bmatrix}, \tag{2.8}$$

where ΔT is the determinant of the matrix as defined in equation 2.9 [46].

$$\Delta T = T_{11}T_{22} - T_{12}T_{21} \tag{2.9}$$

Since this study is concerned with characterising the S-parameter performance of the realised prototypes using the measured S-parameters from the VNA in figure 2.15, equation 2.5 should be expressed using S-parameters. The de-embedding equation can be therefore be expressed in equation 2.10 in terms of S-parameters using equations 2.6 and 2.7.

$$\begin{bmatrix} \frac{-\Delta S_{VNA}}{S_{VNA_{21}}} & \frac{S_{VNA_{11}}}{S_{VNA_{21}}} \\ \frac{-S_{VNA_{22}}}{S_{VNA_{21}}} & \frac{1}{S_{VNA_{21}}} \end{bmatrix} = \begin{bmatrix} \frac{-\Delta S_a}{S_{a_{21}}} & \frac{S_{a_{11}}}{S_{a_{21}}} \\ \frac{-S_{a_{22}}}{S_{a_{21}}} & \frac{1}{S_{a_{21}}} \end{bmatrix} \begin{bmatrix} e^{-j\beta l} & 0 \\ 0 & \frac{1}{e^{-j\beta l}} \end{bmatrix} \begin{bmatrix} \frac{-\Delta S_b}{S_{b_{21}}} & \frac{S_{b_{11}}}{S_{b_{21}}} \\ \frac{-S_{b_{22}}}{S_{b_{21}}} & \frac{1}{S_{b_{21}}} \end{bmatrix} \tag{2.10}$$

In equation 2.10 S_a and S_b denote the two S-parameters of the back-to-back adapters, which are assumed to have identical S-parameters. Equation 2.10 was implemented in Matlab to facilitate the de-embedding of measured results given later in this study.

2.8 SUMMARY

An overview of the partial H-plane waveguide and existing waveguide transitions was given in previous subsections. Previously existing partial H-plane adapters were mentioned in eight publications [3]-[5], [9], [10], [13], [16], [17] with the dimensions and geometry only given with sufficient detail to allow reproduction in six of the eight publications [4], [5], [10], [13], [16], [17]. It should be noted that only two types of partial H-plane waveguide transitions currently exist with one being for the more specialised SIFW scenario which terminates in either stripline or microstrip. Thus there currently only exists the probe feed for general coaxial applications. Additionally the insertion losses and return losses of the existing transitions are not ideal and could be better.

A brief overview of how the input impedance of waveguide adapters is derived is also given and reasons given why such a derivation for a partial H-plane waveguide adapter would be difficult and mostly futile. Lastly the back-to-back measurement setup and single ended de-embedding equation has been given and discussed.

In summary one can say that current partial H-plane waveguide research is mainly focused at realising compact filters and slot array antennas with little to no effort being spent on developing well defined and effective waveguide adapters.

The lowest reflection coefficient and insertion loss achieved in existing partial H-plane waveguide adapters are -19 dB and 0.1 dB respectively for narrow band filter applications [10]. Additionally the practical conventional rectangular waveguide adapters mentioned in this section can achieve better than -20 dB reflection coefficient [23]-[25] and 0.5 dB insertion loss [36]-[38] for the coaxial and microstrip transitions. Therefore the design goals for this study will be to achieve a -20 dB reflection coefficient and 0.5 dB insertion loss.

CHAPTER 3 END-LAUNCHED COAXIAL TO WAVEGUIDE ADAPTER

3.1 INTRODUCTION

In chapter 1 the motivation for realising practical partial H-plane waveguide transitions was discussed as a research gap. This chapter details the development of the end-launched waveguide adapter discussed in the research goals and the microstrip adapter is discussed in the following chapter. The majority of the previously existing partial H-plane waveguide transitions operated in H-band (3.95 to 5.85 GHz) and therefore this study will also focus on H-band adapters to allow comparison with those adapters.

3.2 CONCEPT DEVELOPMENT

The L-shaped loop from chapter 2 was selected as the conventional rectangular transition that would be adapted to the partial H-plane waveguide configuration. Since the L-shaped loop (consisting of a transmission line part and a probe part) is inserted at the maximum of the E-field and all of its geometry lies along the centre-line of the waveguide it lends itself to being adapted for the partial H-plane scenario. This is because a rectangular waveguide is transformed into a partial H-plane waveguide by bending it similar to a horseshoe as previously shown in figure 2.1. Given that the E-field is at a maximum at the edge of the H-plane vane [2], the probe part of the L-shaped loop would have to be inserted here.

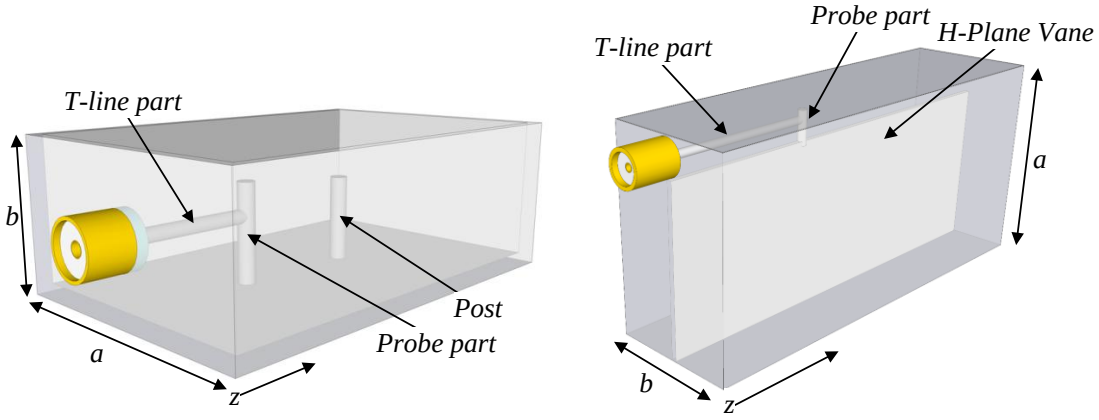

(a) (b)

Figure 3.1. L-shaped loop in rectangular (a) and partial H-plane (b) waveguides.

Figure 3.1 shows the L-shaped loop in conventional rectangular waveguide (same as figure 2.11) and in the partial H-plane waveguide. Note that the *a* and *b* dimensions are not equivalent in the two different waveguides in the figure and therefore the figures are not to scale. The partial H-plane waveguide is smaller with a quarter reduction of the cross-sectional area since it's *a* and *b* dimensions are approximately half of the *a* and *b* of the conventional waveguide. Note that the tuning post from the conventional waveguide has not been carried over to the initial partial H-plane geometry. The reason for this is because the approach was to determine what is achievable before unnecessarily complicating the design. Therefore this study will follow the spiral development process of continually updating the design until it achieves the desired performance of a -20 dB reflection coefficient and 0.5 dB insertion loss.

3.2.1 L-shaped loop

The geometry given in figure 3.1 (b), with a waveguide width *a* and height *b* of 23.8 mm and 12 mm respectively for H-band was simulated and S-parameters were obtained after some optimisation in CST MWS, and are shown in figure 3.2.

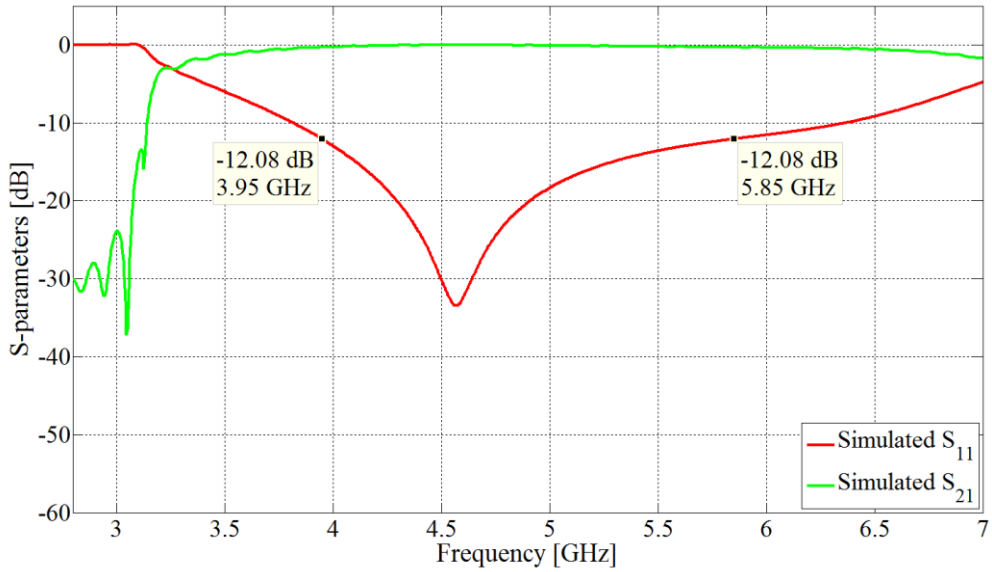

Figure 3.2. Simulated S-parameters for L-shaped loop adapter in partial H-plane waveguide.

Figure 3.2 shows that a minimum (worst case) return loss of 12.08 dB is achieved over the band; the highest insertion loss is 0.27 at the lower edge of the band. Since the insertion loss is already satisfactory the focus will be on improving the return loss of the prototype.

3.2.2 With cut-out

As discussed in section 2.4.2 the L-shaped loop consists of a transmission line (T-line in figure 3.3) part and a probe part as given below for the partial H-plane geometry.

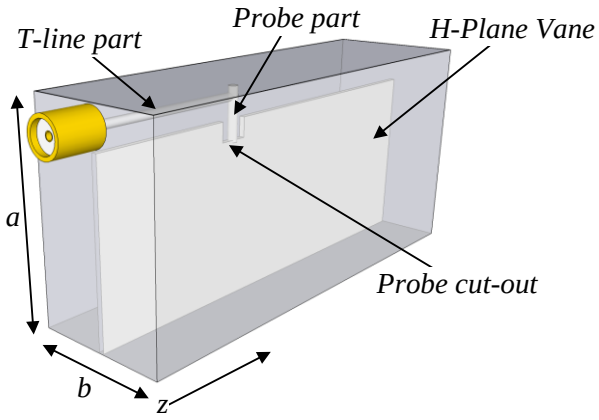

Figure 3.3. L-shaped loop with probe cut-out.

Since the distance between the H-plane vane and side wall is quite small, a cut-out or notch in the vane can allow for a longer probe part of the loop which is required to achieve resonance. The effect of a longer probe which is much closer to resonance is given in figure 3.4, which has been optimised for absolute minimum S_{11} which is inherently narrow band as the structure is singly tuned.

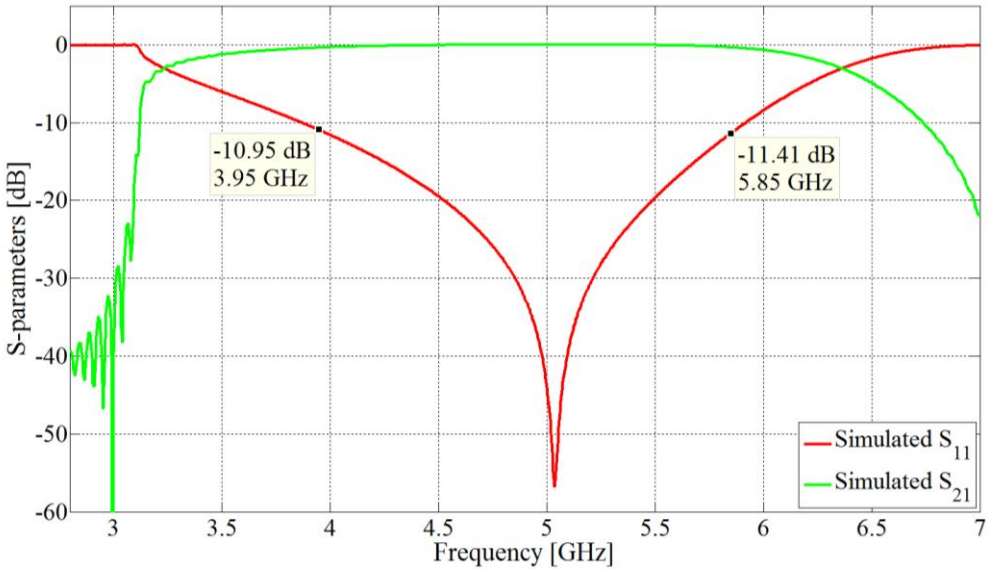

Figure 3.4. Simulated S-parameters for L-shaped loop with cut-out optimised for narrow band operation.

This study is primarily concerned with the design of waveguide transitions that perform over the entire H-band, but it is interesting to note that the narrow band match in figure 3.4 achieves an S_{11} of more than -50 dB. This extremely deep null is a result of the longer probe which is significantly closer to resonance than the probe without the cut-out previously given in figure 3.2. Optimising the prototype with the cut-out for full band operation yields a minimum return loss of 14.45 dB over the band as shown in figure 3.5.

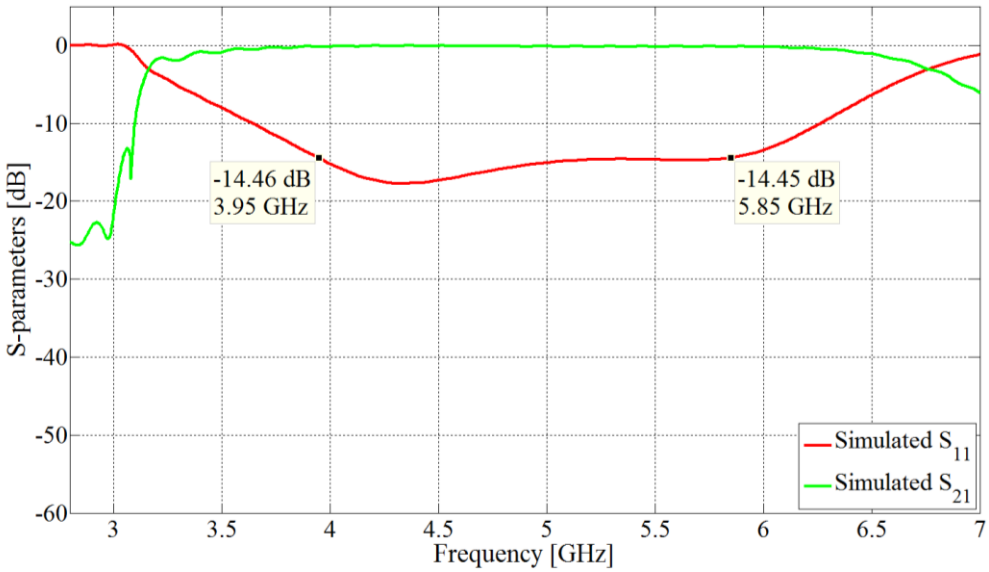

Figure 3.5. Simulated S-parameters for L-shaped loop with cut-out optimised for wideband operation.

This is an improvement over the 12.08 dB achieved without the cut-out, but is still not satisfactory for general purpose use.

3.2.3 With Impedance matching section

Since the T-line part of the feed geometry is similar to a trough transmission line [31] the characteristic impedance of the T-line can be varied by changing the distance between the side wall and centre conductor. Therefore an impedance matching section of transmission line can be introduced as shown in figure 3.6 through the addition of a bend in the T-line. The first section of the transmission line can be kept at 50 Ω to ensure continuity through the shorting waveguide wall, whilst the second part can have a different characteristic impedance to facilitate impedance matching. Since the probe part is typically located at a quarter wavelength from the shorting wall a quarter-wave transformer can be realised.

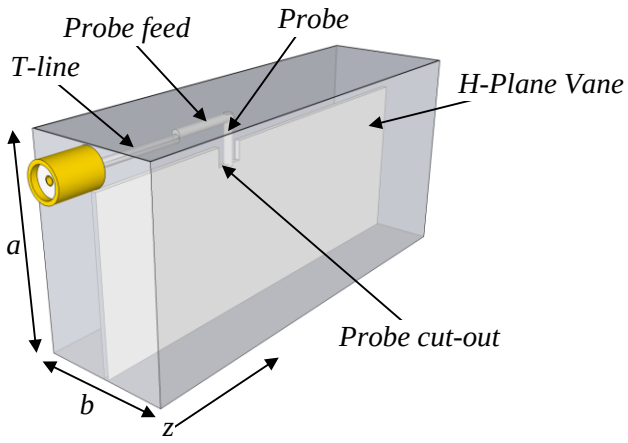

Figure 3.6. Prototype transition with an additional impedance matching section (probe feed).

The resulting insertion and return losses of the concept adapter with the additional impedance matching section is given in figure 3.7. The worst in-band return loss is 15.44 dB at the lower frequency limit.

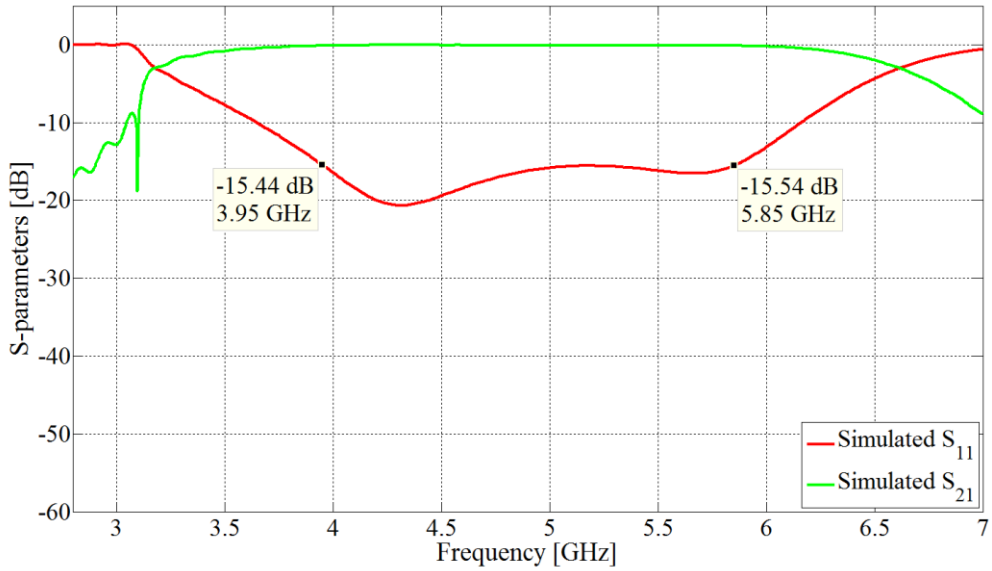

Figure 3.7. Simulated S-parameters for L-shaped loop with cut-out and matching section optimised for wideband operation.

Whilst the improvement achieved through the addition of the impedance matching section is minimal it is required to maximise the performance achieved with the addition of a tuning post in the following subsection.

3.2.4 With tuning post

The concept adapter up to this point has been singly tuned as it only has the single resonance of the probe part which can yield a very deep single notch as shown in figure 3.4. By optimising for a wideband solution the deep notch can be spread over a wider frequency range through some deliberate mismatching to not yield a perfect match at a single frequency but rather a best effort over the entire band.

The addition of a tuning post makes the structure doubly tuned with two resonances resulting in two deep notches at two different frequencies (since the length and positions of the probe and tuning post are different). Figure 3.8 shows the concept adapter geometry with the addition of a tuning post. Note that the tuning post, similar to the probe, does not short against the waveguide side wall.

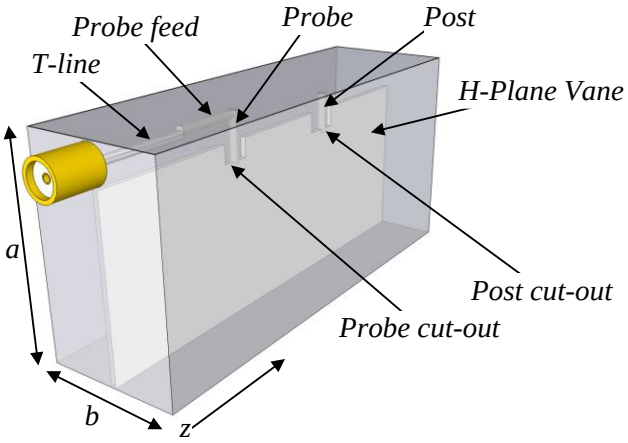

Figure 3.8. Prototype transition with a tuning post.

The resulting adapter performance is given in figure 3.9 below in terms of insertion and return losses. The addition of the tuning post has significantly improved the reflection coefficient which is now -20.38 dB and the insertion loss is 0.05 dB which is acceptable for general purpose use. The concept can achieve even better results through the use of more tuning posts, but this increases the complexity in manufacturing and tuning.

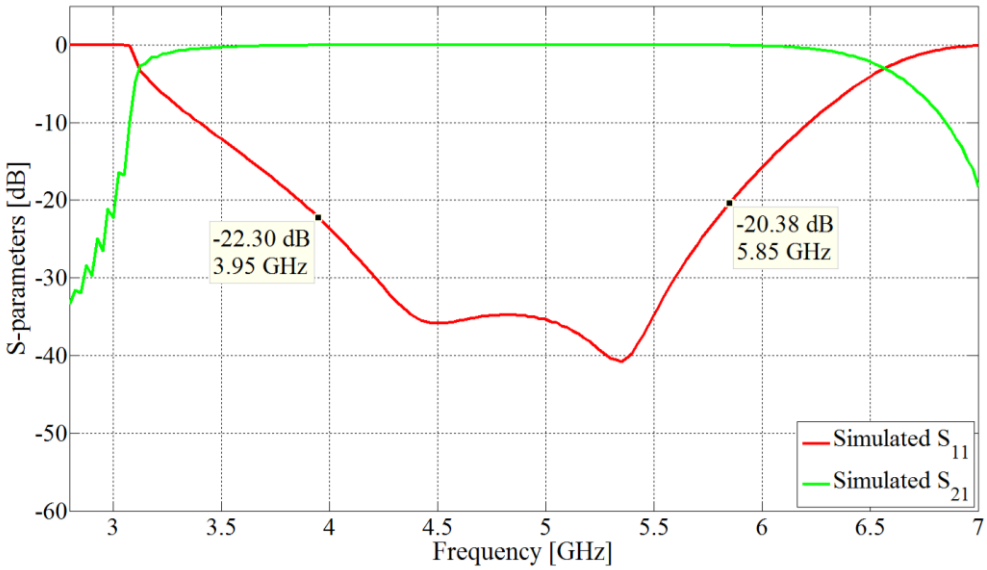

Figure 3.9. Simulated S-parameters for L-shaped loop with cut-out, matching section and tuning post optimised for wideband operation.

The concept with the addition of the tuning post is the final end-launched prototype as it satisfies the requirements for insertion and return losses. The final geometry will be further explored in the following parametric study.

3.3 PARAMETRIC STUDY

The purpose of the parametric study is to determine which parameters (physical dimensions and material properties) affect the real or imaginary parts of the impedance and the insertion and return losses and therefore influencing the achievable bandwidth. The parameters will be swept 10% above and below their initial values to perform the parameter study. Highly insensitive parameters are swept over more than 10% to yield sufficient variation for plotting purposes.

3.3.1 Waveguide dimensions

The dimension definitions of the partial H-plane waveguide are given in figure 3.10 below.

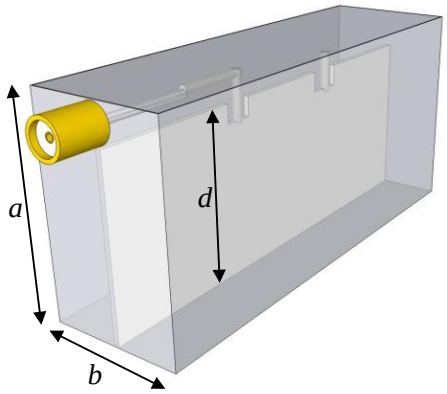

Figure 3.10. Partial H-plane waveguide dimension definitions.

The dimensions *a* and *b* are similar to the conventional waveguide definitions as they denote the long and short sides of the waveguide. However it is important to note that in the partial H-plane geometry they are approximately half of the width and height in a conventional rectangular waveguide for the same frequency band. The H-plane vane depth is denoted *d* in figure 3.10. For this study the same waveguide dimensions previously used in [3], [9], [10] for H-band (3.95 to 5.85 GHz) are utilised to facilitate comparisons with the previously published results reported in section 2.3. These dimensions are 23.8 mm for *a*, 12 mm for *b* and 20.2 mm for *d*.

The fundamental partial H-plane waveguide mode $TE_{0(01)}$ resembles a horseshoe as previously shown in figure 2.1 (a); the second mode $TE_{1(00)}$ resembles the TE_{10} in a conventional waveguide with a single sinusoidal variation above and below the vane along

the width of the waveguide (*a* dimension). By varying the waveguide dimensions (*a*, *b* and *d*) the cut-off frequencies for the fundamental and second mode can be adjusted independently. This is possible since the cut-off frequency for the fundamental mode depends on the length of the "horseshoe" which can be varied by changing the depth *d* of the H-plane vane and the waveguide height *b*. The second mode depends on the width *a* of the waveguide and is independent of the other parameters. It is interesting to note that the cut off frequency of the second mode is the same as the fundamental TE_{10} of a conventional waveguide of the same (reduced *a* and *b*) size if the vane was removed. Figure 3.11 below shows the effect of changing the *d/a* and *a/b* ratios for a hypothetical L-band (1.12 - 1.7 GHz) waveguide. Note that the coloured lines are the resulting $TE_{0(01)}$ cut-off frequencies.

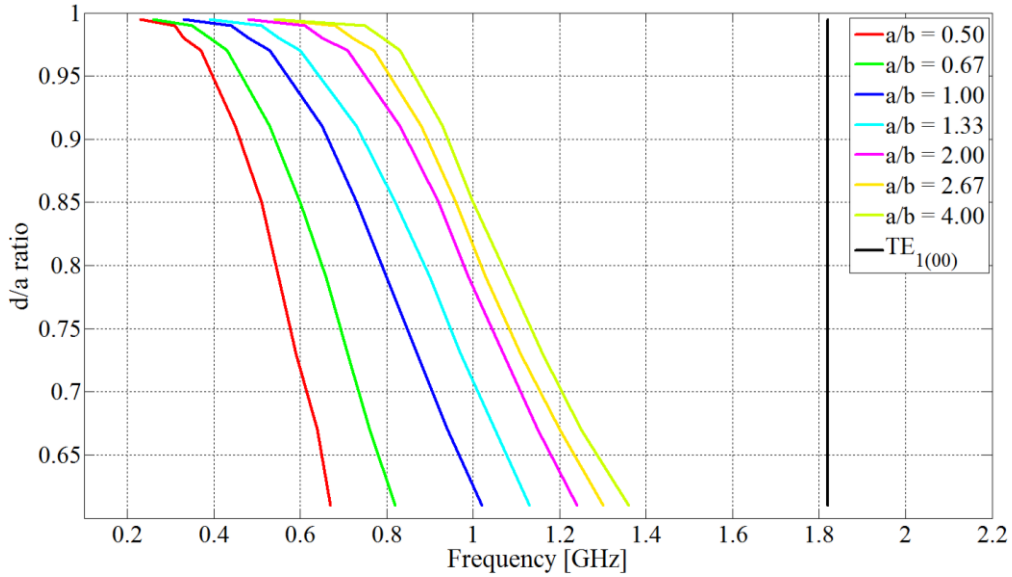

Figure 3.11. Partial H-plane waveguide $TE_{0(01)}$ and $TE_{1(00)}$ modes cut-off frequencies.

Note that the *a* parameter is kept constant and *d* and *b* are varied, which is why the $TE_{1(00)}$ mode remains unchanged when the *b* and *d* parameters are changed in figure 3.11. Increasing the *d/a* ratio (wider vane) decreases the fundamental cut off frequency as expected as it increases the length of the "horseshoe". Similarly increasing *b* results in a decreased fundamental frequency but has diminishing returns if it is made much larger than dimension *a*. Another way to represent the advantage of being able to independently control the cut-off frequencies of the $TE_{0(01)}$ and $TE_{1(00)}$ modes is to calculate the achievable percentage bandwidth (defined in section 2.4.1) of the waveguide when the *a*,

b and *d* parameters are changed. Figure 3.12 gives the percentage bandwidth in an image format, with percentage bandwidth to colour mapping on the right hand side.

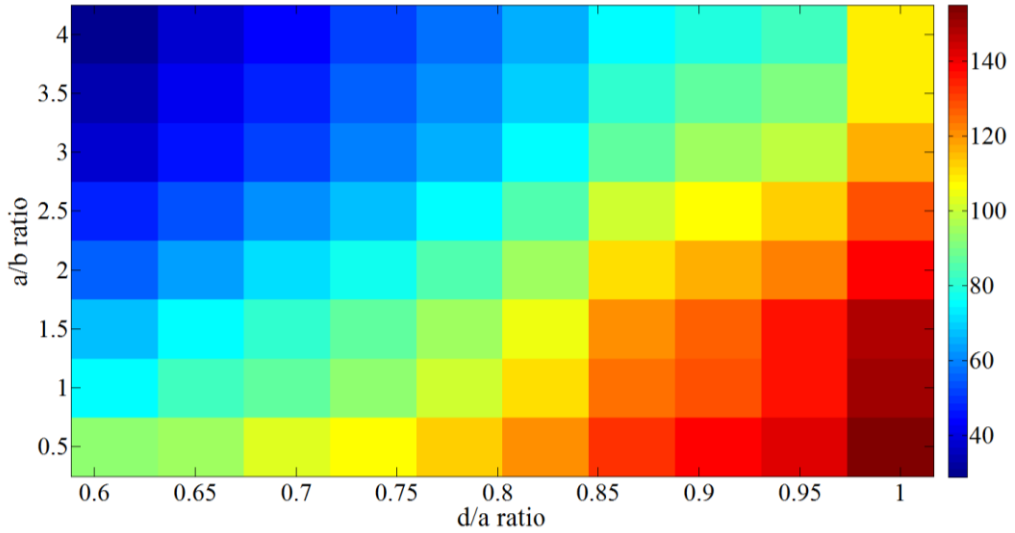

Figure 3.12. Percentage bandwidth versus a/b and d/a ratios.

The achievable bandwidth of the partial H-plane waveguide increases when either of the dimensions *d* or *b* is increased. The width parameter *a* is again not varied in figure 3.12 as it effects both the fundamental and second modes. Note that a percentage bandwidth of over 150% is achievable with the partial H-plane waveguide when *b* is twice *a* and *d* approaches *a*. However it is important to note that having *b* twice as big as *a* results in a overall cross-sectional area that is the same size as a conventional waveguide for the original desired band. Granted that the bandwidth is significantly more than that of a conventional waveguide, however this study is concerned with enabling the size advantage of using a partial H-plane waveguide over a conventional waveguide where the same bandwidth as a conventional waveguide is sufficient for the application. However it is interesting to note that it is possible to achieve high bandwidths if desired in other applications.

3.3.2 Trough transmission line

As previously mentioned the transmission line section of the feed geometry is similar to the well defined trough line in [31]. The transmission line would be very close to a trough line if the vane is sufficiently far away from the wire forming the transmission line section. Figure 3.13 shows the field density around the centre conductor of the transmission line.

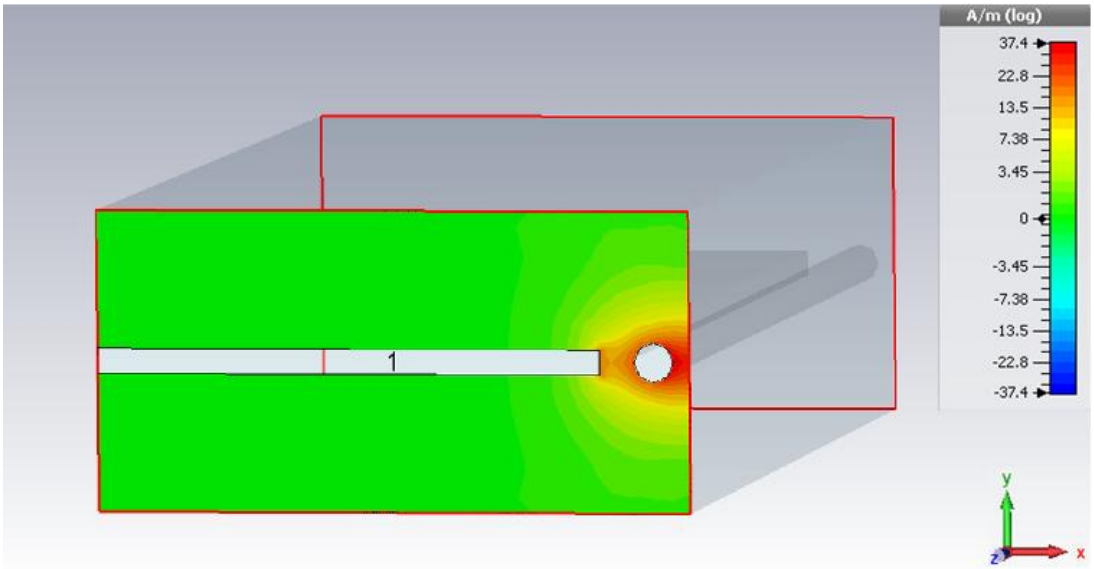

Figure 3.13. Partial H-plane waveguide trough transmission line field density around centre conductor.

Note that most of the field intensity (log scale) is concentrated between the centre conductor and waveguide wall rather than between the centre conductor and vane. Therefore the transmission line part of the feed geometry behaves similar to a trough line. Figure 3.14 below gives the characteristic impedance of the trough line in figure 3.13 for various centre line thicknesses and offset from side wall using a CST MWS simulation.

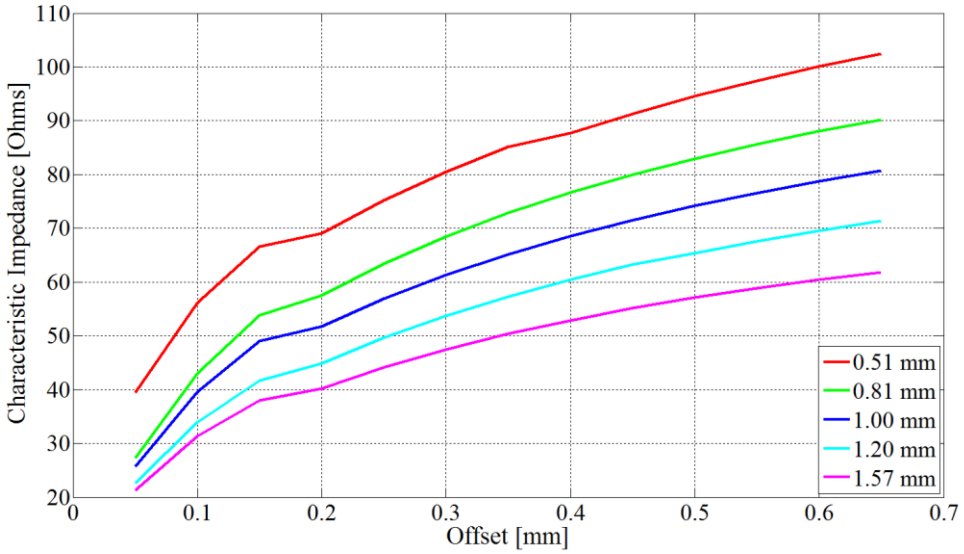

Figure 3.14. Partial H-plane waveguide trough characteristic impedance vs. the offset from the side wall for various centre line thicknesses.

3.3.3 SMA offset

The SMA offset parameter is defined as the distance between the extended centre conductor of the SMA connected and the inside side wall of the partial H-plane waveguide, as show in figure 3.15.

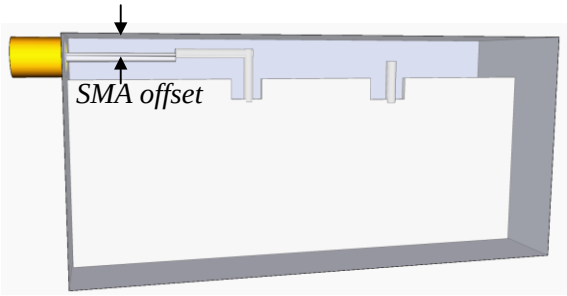

Figure 3.15. SMA offset dimension definition.

For manufacturing and power handling reasons the minimum acceptable offset was selected as 0.5 mm from the edge of the centre conductor. The power levels considered in this study is in the order of a few watts to realise low power filters and antennas using the waveguide adapters. Figure 3.16 below gives the input impedance for different offsets. The real and imaginary components are shown with the abbreviation "Re" and "Im" in the figure's legend. The real components are the bright colours, whilst the corresponding dull colours represent the imaginary components.

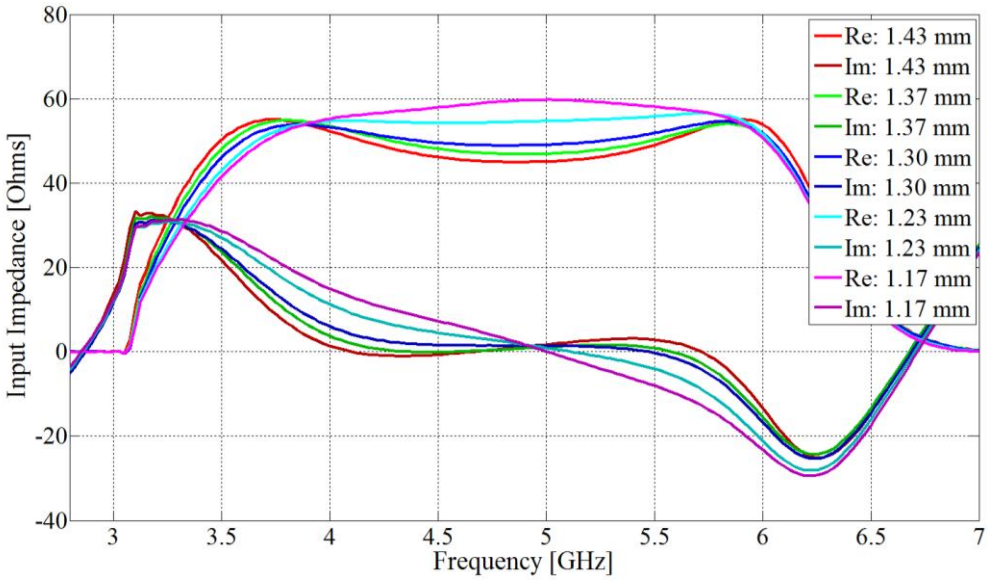

Figure 3.16. Complex input impedance for different SMA offsets.

Note that smaller SMA offsets result in larger real component values and vice versa; therefore the input impedance is quite sensitive to variations in the SMA offset. The reflection coefficient for the various offsets is given in figure 3.17, where the parameter sensitivity can also be seen.

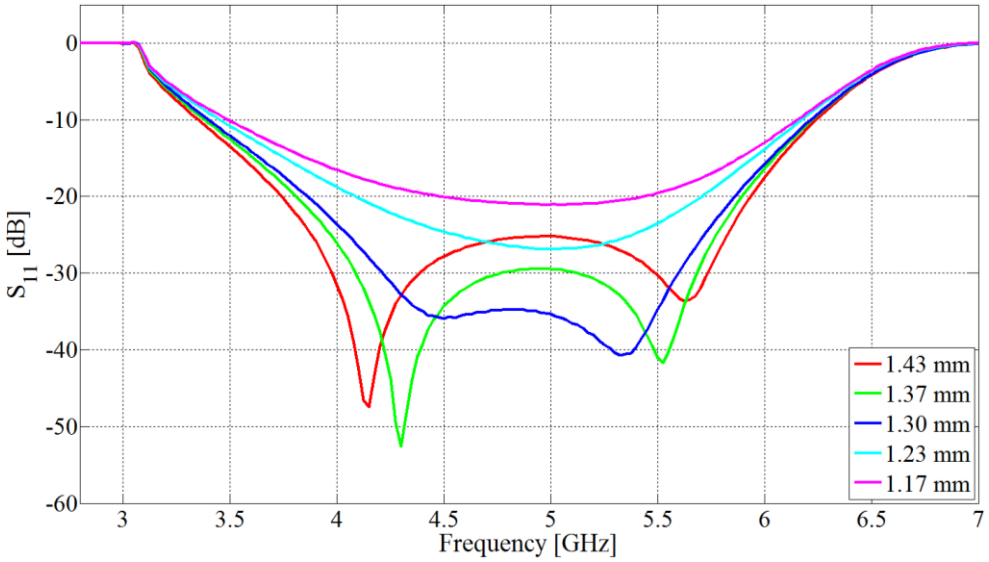

Figure 3.17. Simulated reflection coefficient for different SMA offsets.

The simulated insertion losses for the various SMA offsets are given below in figure 3.18.

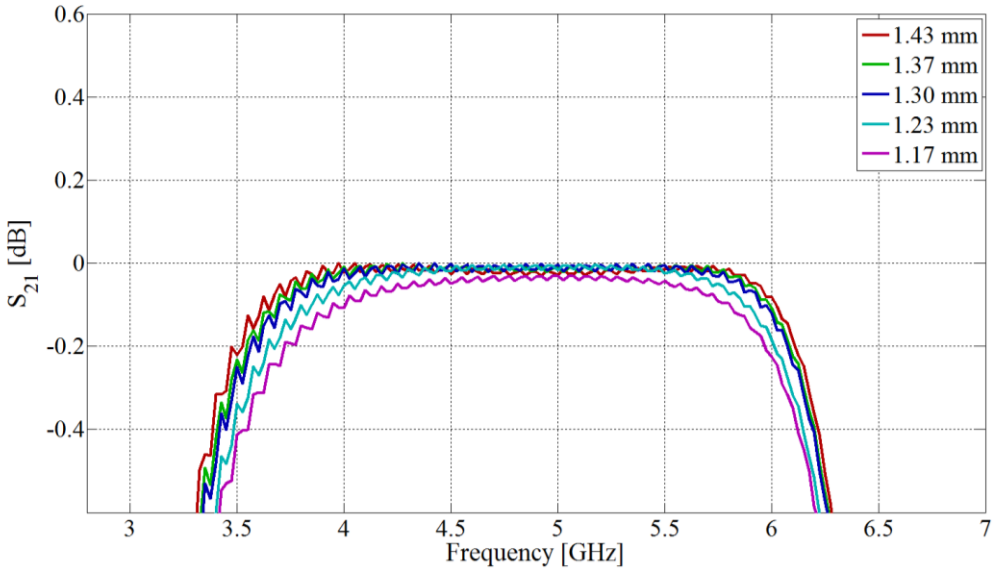

Figure 3.18. Simulated transmission coefficient for different SMA offsets.

The small ripple in the figure above and other insertion loss figures in this chapter are the result of a simulation artefact. If the CST time domain solver accuracy is increased the ripple can be decreased at the expense of significantly increased simulation time.

3.3.4 Feed-line length

The feed-line length is defined as the length of the transmission line inside the waveguide between the shorting wall and impedance matching section as shown in figure 3.19.

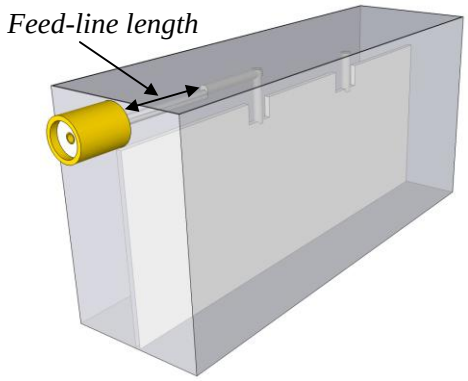

Figure 3.19. Feed-line length dimension definition.

The feed-line is realised by utilising a commercially available SMA connector with extended centre pin and dielectric. The dielectric is extended through the waveguide's shorting wall to have a seamless 50 ohm coaxial transmission medium through the shorting wall. The centre conductor forms the feed-line and connects to the matching section via a solder joint. Figure 3.20 gives the input impedance for different feed-line lengths.

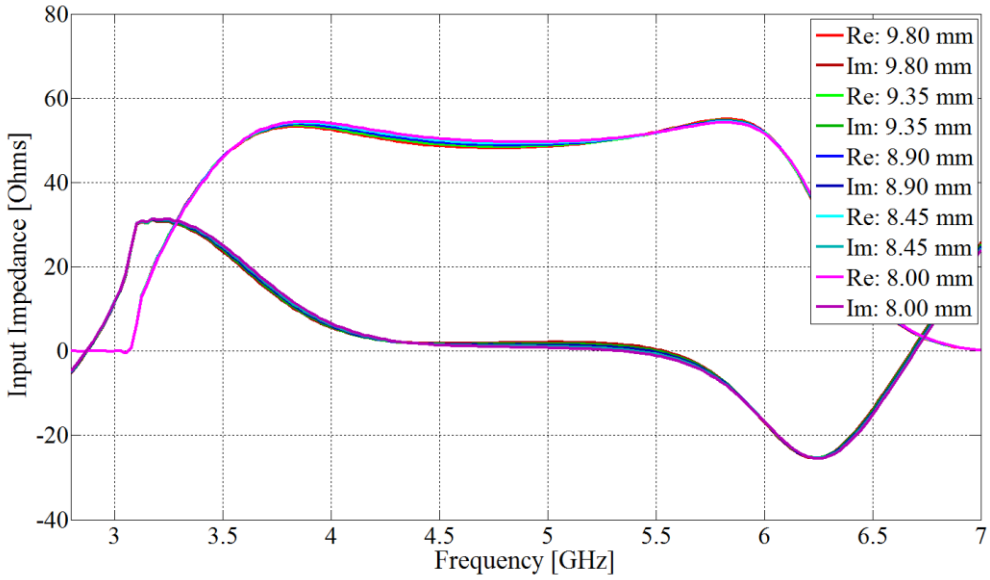

Figure 3.20. Complex input impedance for different feed-line lengths.

Note that the input impedance appears to be reasonably insensitive to changing the feed-line length; which is expected as it is essentially a continuation of the 50 Ω coaxial transmission line into the partial H-plane waveguide. The reflection coefficient for varying feed-line lengths is given in figure 3.21 below.

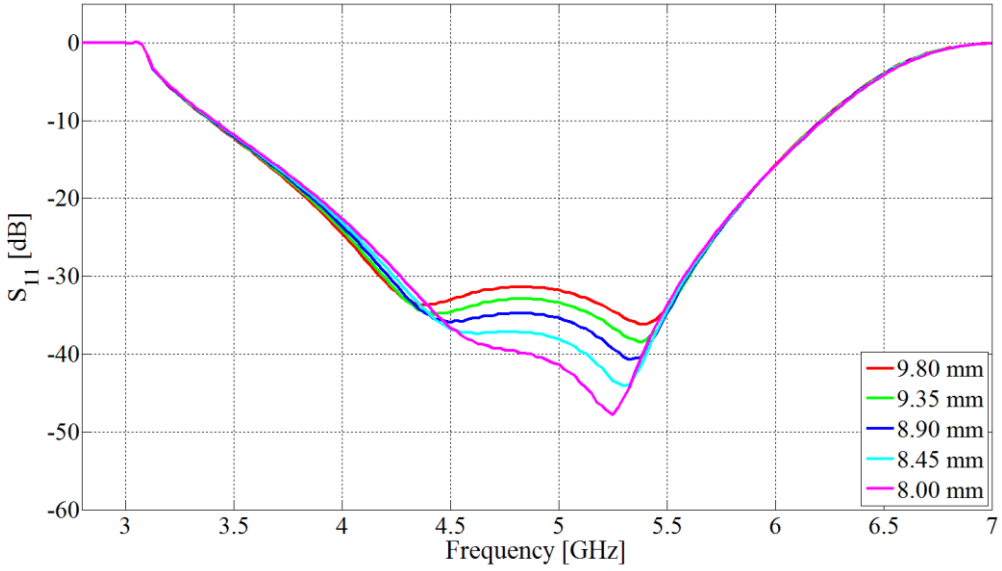

Figure 3.21. Simulated reflection coefficient for different feed-line lengths.

Figure 3.22 shows the effect of different feed-line lengths on the simulated insertion loss.

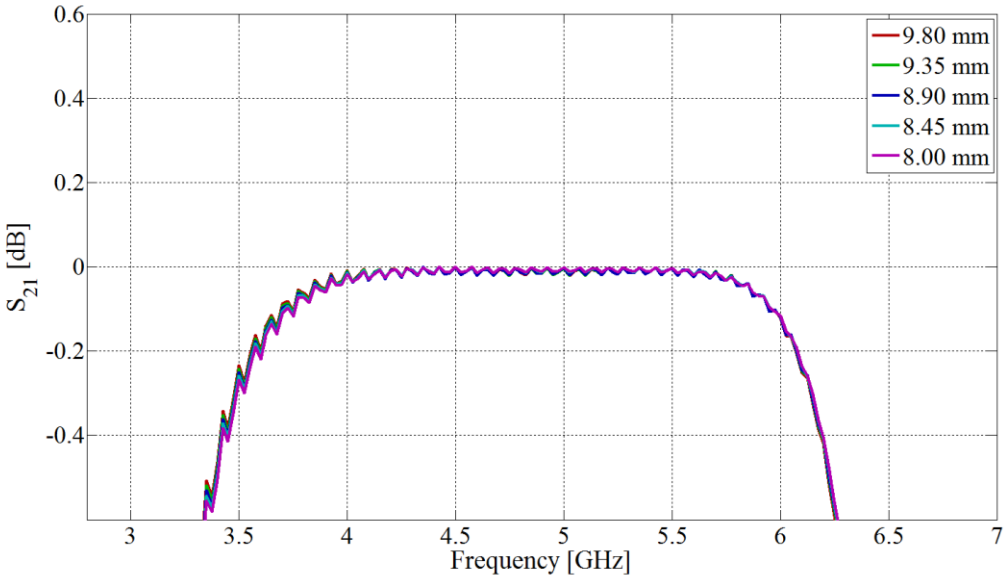

Figure 3.22. Simulated transmission coefficient for different feed-line lengths.

3.3.5 Probe feeder offset

The probe feeder offset is the distance between the centre of the impedance matching section of trough transmission line and the waveguide's side wall as shown in figure 3.23.

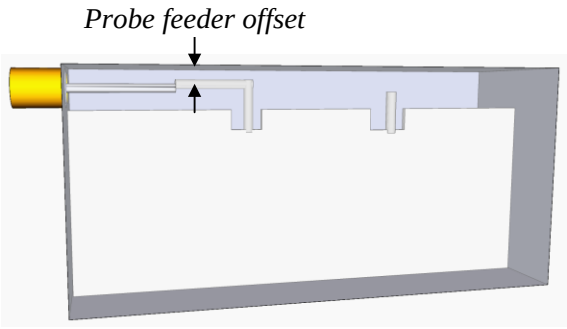

Figure 3.23. Probe feeder offset definition.

As in the SMA offset parameter, the minimum acceptable offset was selected as 0.5 mm from the edge of the conductor for manufacturing tolerances and power handling. The complex input impedance for the various offsets is given below in figure 3.24.

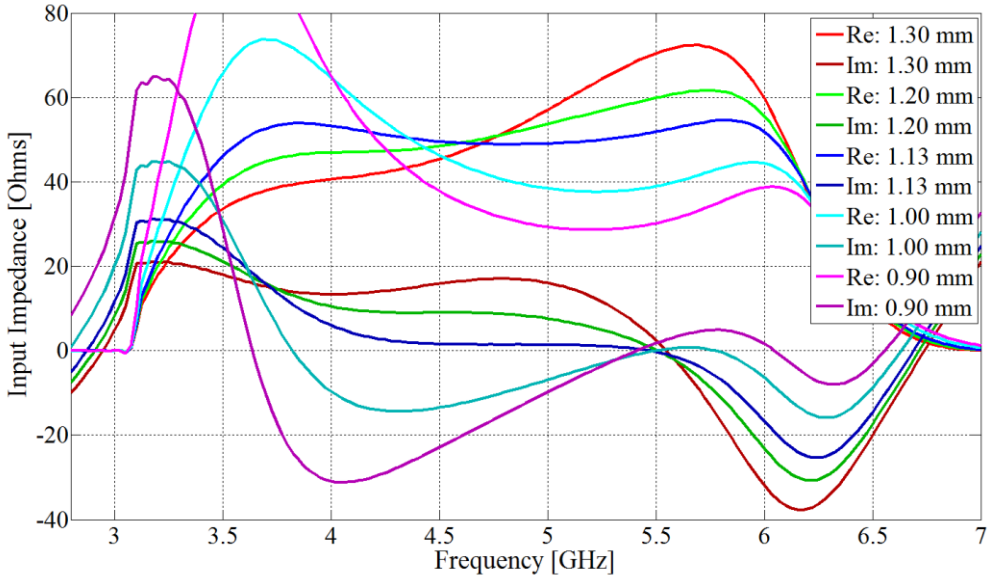

Figure 3.24. Complex input impedance for different probe feeder offset values.

Note that the input impedance is extremely sensitive to changes in the parameter with large variations in both the real and imaginary components visible in figure 3.24.

The reflection coefficient for the different probe feeder offsets is given in figure 3.25. As with the input impedance plot, the reflection coefficient plot also shows that the prototype is extremely sensitive to changes in the probe feeder offset parameter.

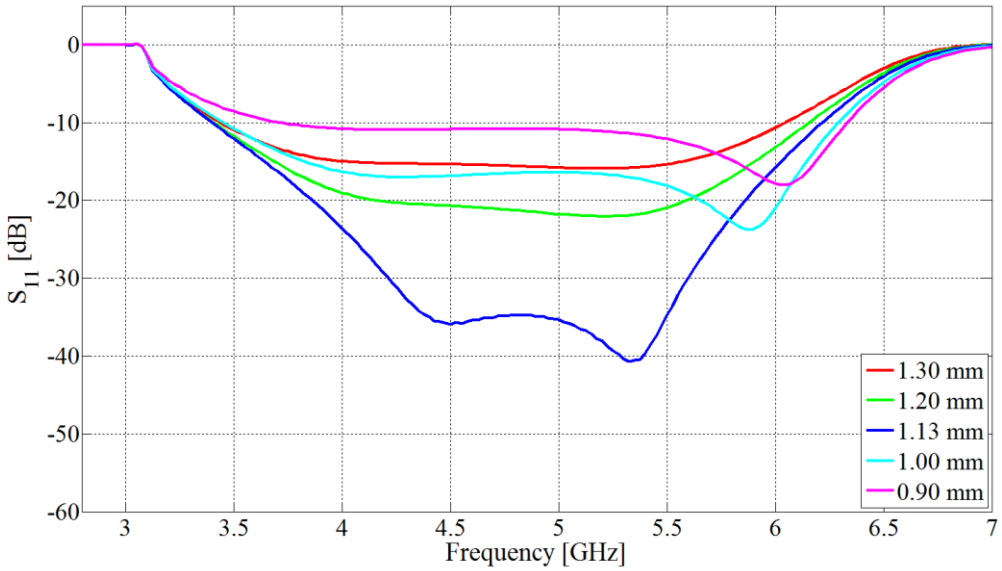

Figure 3.25. Simulated reflection coefficient for different probe feeder offsets.

The simulated insertion losses for the various probe feeder offsets are given below in figure 3.26. Note that even in the worst case of 0.90 mm, the insertion loss is still acceptable.

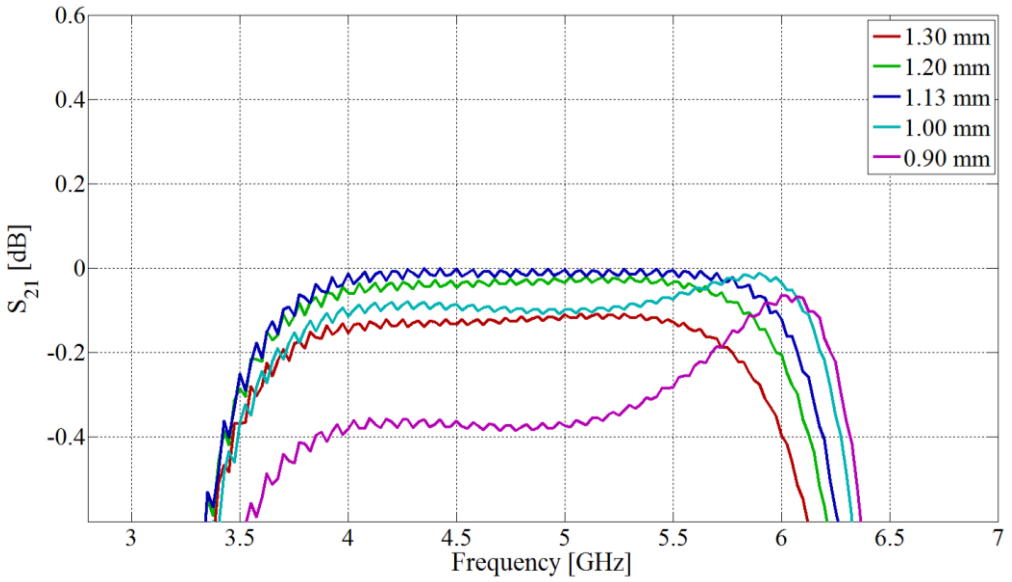

Figure 3.26. Simulated transmission coefficient for different probe feeder offsets.

3.3.6 Probe position

The probe position is defined as the distance between the centre of the probe and the shorting wall of the waveguide as shown in figure 3.27.

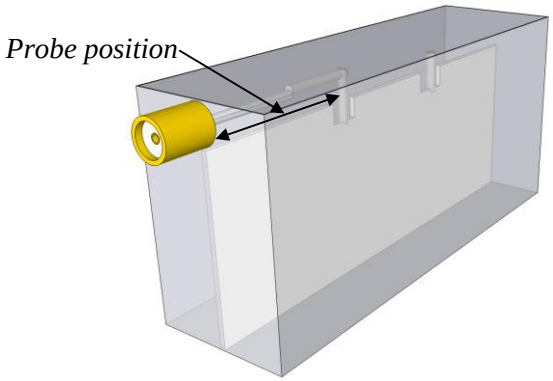

Figure 3.27. Probe position dimension definition.

Note that the probe position length does not include the thickness of the shorting wall (6 mm, see section 3.4 for more details). The input impedance for the various probe positions is given below in figure 3.28.

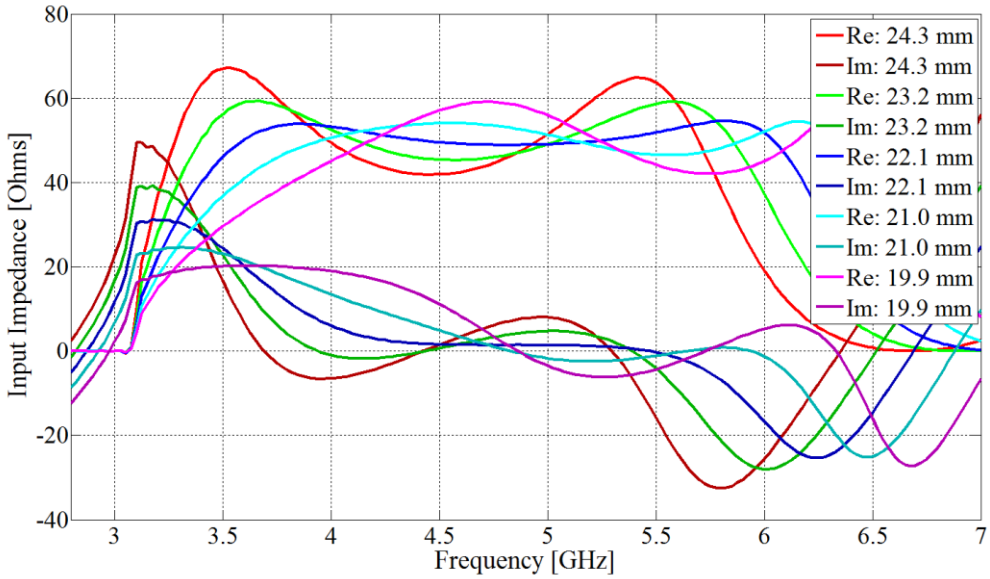

Figure 3.28. Complex input impedance for different probe positions.

Note that the figure above shows that the input impedance is very sensitive to variations in the probe position parameter. This result was expected as the probe position sets the resonant frequency of the probe inside the waveguide.

The simulated reflection coefficient achieved with the various probe positions is given in figure 3.29.

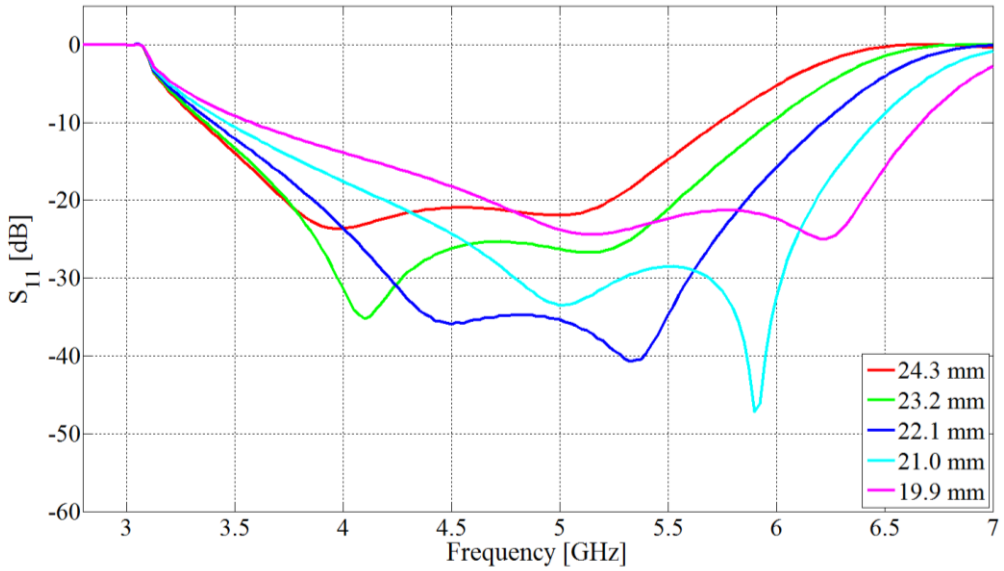

Figure 3.29. Simulated reflection coefficient for different probe positions.

The simulated insertion losses for the various probe positions are given below in figure 3.30.

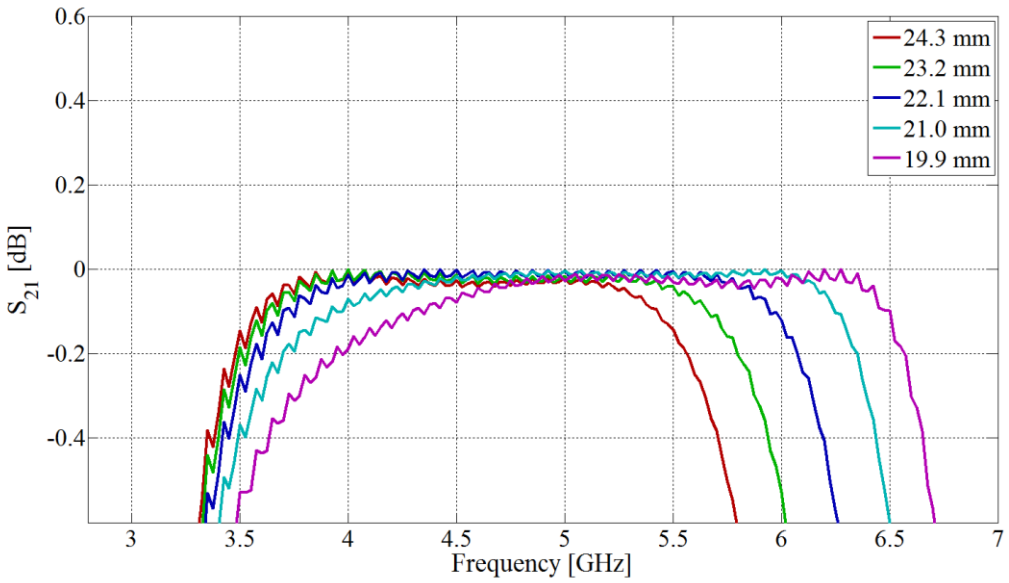

Figure 3.30. Simulated transmission coefficient for different probe positions.

As with the input impendence and reflection coefficient, the insertion loss also exhibits the sensitive nature of the probe position parameter; however the insertion loss is still acceptable.

3.3.7 Probe cut-out depth

Figure 3.31 defines the probe cut-out depth as the depth that the probe extends into the vane inside of the cut-out, thereby setting the length of the probe.

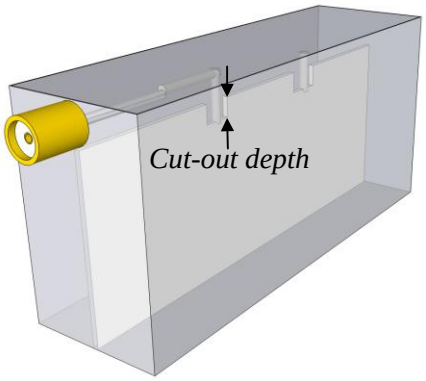

Figure 3.31. Probe cut-out depth dimension definition.

The input impedance of the prototype transition for various probe cut-out depths is given in figure 3.32. Note that the probe cut-out only occupies a small percentage of the total vane depth of 20.2 mm.

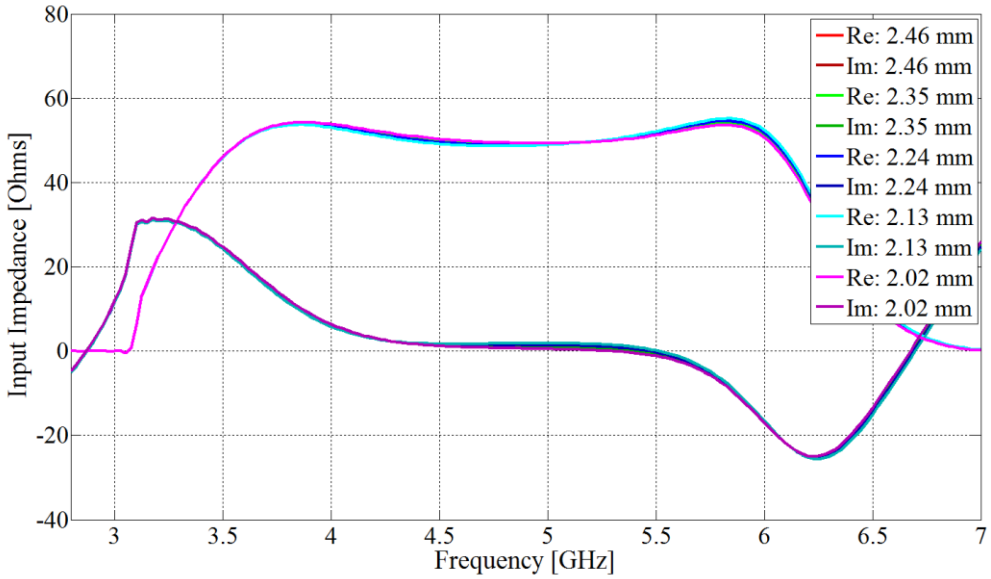

Figure 3.32. Complex input impedance for different probe cut-out depths.

From the figure is appears that the design parameter is relatively insensitive to probe cut-out depth variations. The reflection coefficient for the various depths is given in figure 3.33.

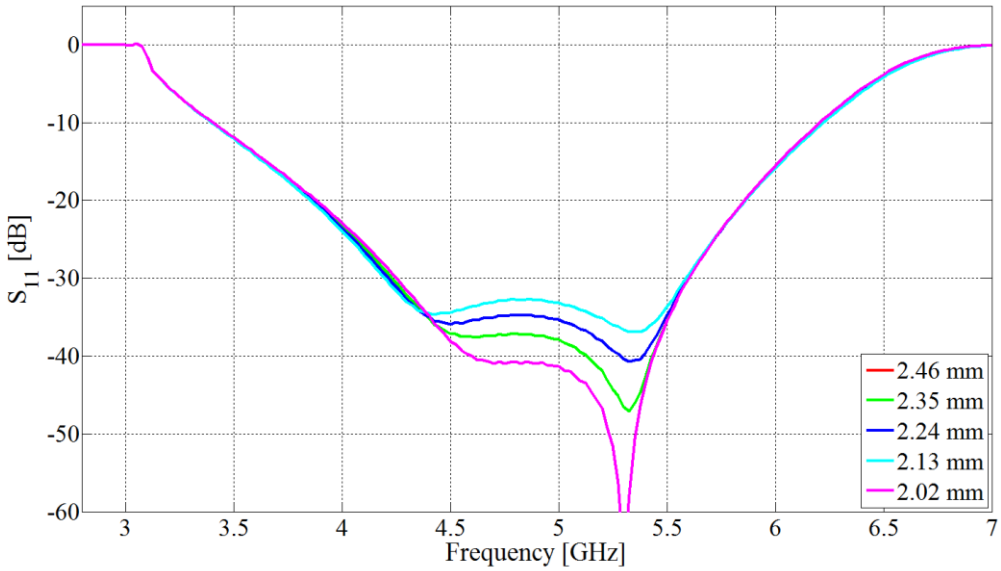

Figure 3.33. Simulated reflection coefficient for different probe cut-out depths.

Figure 3.34 shows the effect of different probe cut-out depths on the simulated insertion loss.

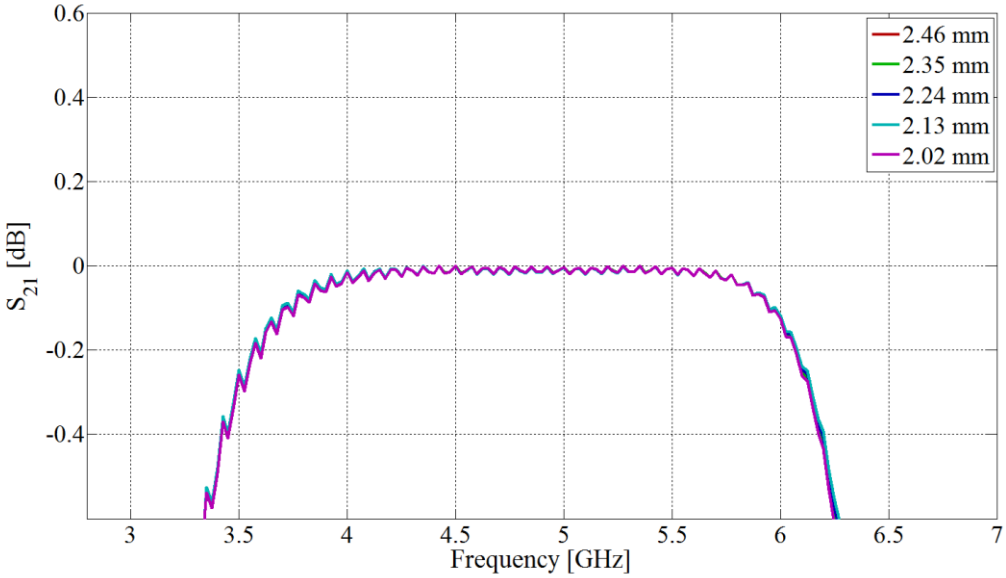

Figure 3.34. Simulated transmission coefficient for different probe cut-out depths.

The insensitivity to the probe cut-out depth is also confirmed from the simulated insertion losses above, where hardly any deviation is visible.

3.3.8 Probe cut-out width

The probe cut-out width is defined as the width of the notch around the probe as shown in figure 3.35.

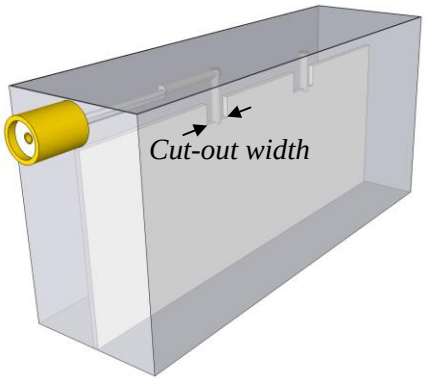

Figure 3.35. Probe cut-out width dimension definition.

The constraint for the cut-width from a manufacturing view would be less than the probe diameter (1.2 mm, see next subsection for details). However from an alignment of the probe to the centre of the cut-out tolerances view, the constraint was selected as 0.2 mm on either side of the probe. Therefore the minimum acceptable probe cut-out width is 1.6 mm. Figure 3.36 below gives the input impedance for different cut-out widths around the probe. The input impedance appears to be insensitive to variations in the cut-out width.

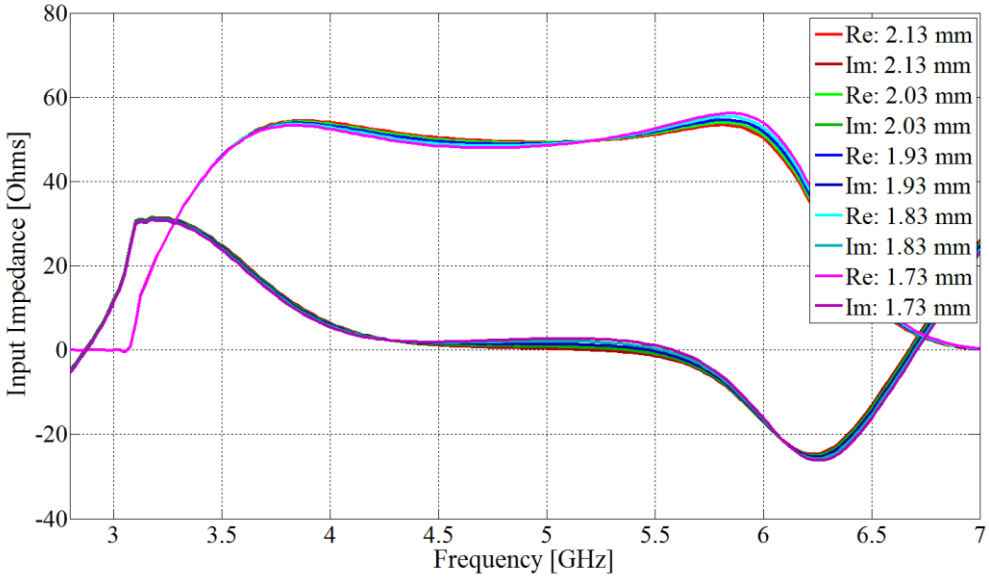

Figure 3.36. Complex input impedance for different probe cut-out widths.

The reflection coefficient for the various probe cut-out widths are given in figure 3.37 and also shows that the design is moderately sensitive to variations in the probe cut-out width.

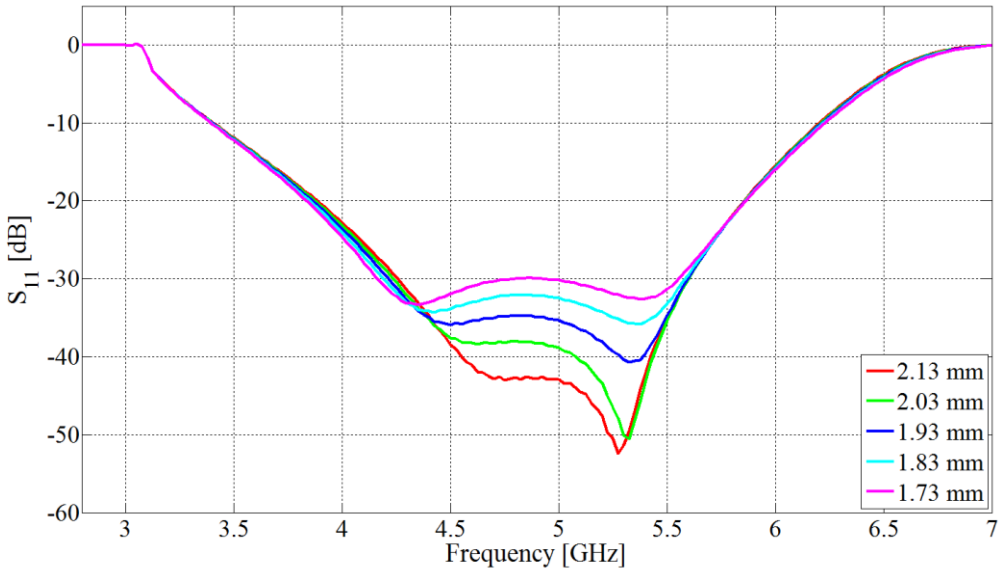

Figure 3.37. Simulated reflection coefficient for different probe cut-out widths.

The simulated insertion losses for the various cut-out widths are given below in figure 3.38.

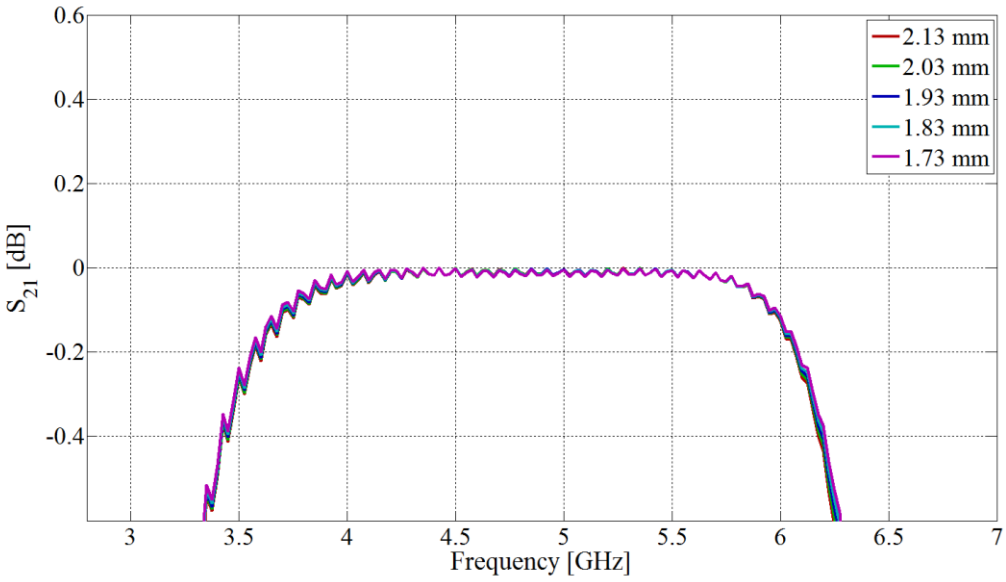

Figure 3.38. Simulated transmission coefficient for different probe cut-out widths.

Note that the insertion loss appears to be insensitive to variations.

3.3.9 Probe diameter

The probe diameter dimension is simply the diameter of the rod that forms the probe as shown in figure 3.39.

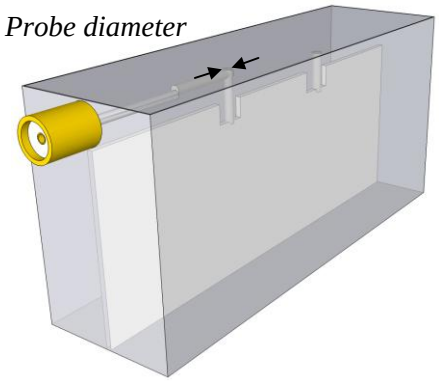

Figure 3.39. Probe diameter definition.

For convenience the nominal probe diameter was set as 1.20 mm, the same diameter as the matching section, which was selected to be close to the 1.25 mm diameter of the centre conductor of the SMA connector. Figure 3.40 gives the input impedance for various probe diameters. Note that over most of the band a smaller diameter results in a larger real component and a larger diameter yields a lower real component.

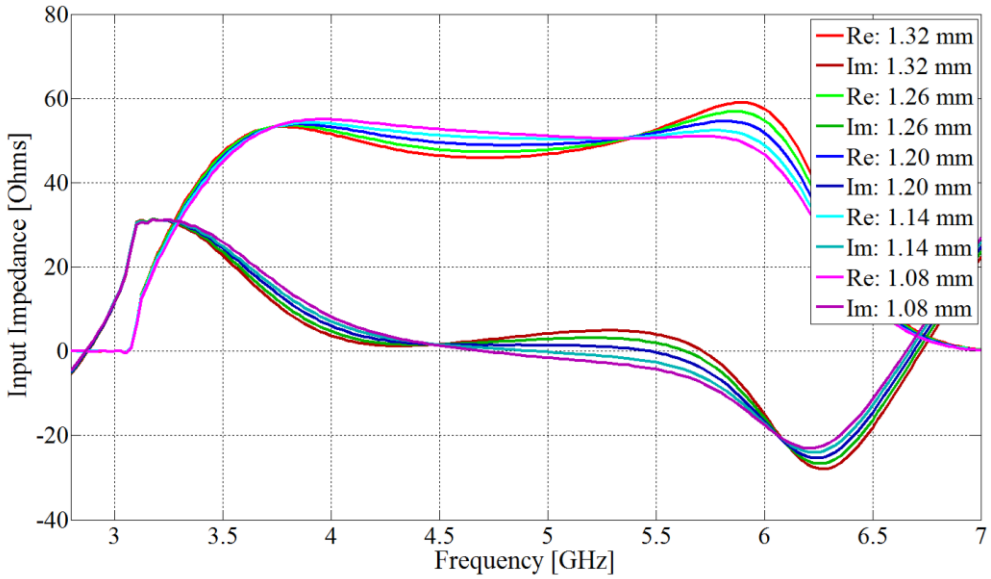

Figure 3.40. Complex input impedance for different probe diameters.

The figure above shows that the prototype is moderately sensitive to variations in the probe diameter.

The reflection coefficient for the various probe diameters is given in figure 3.41.

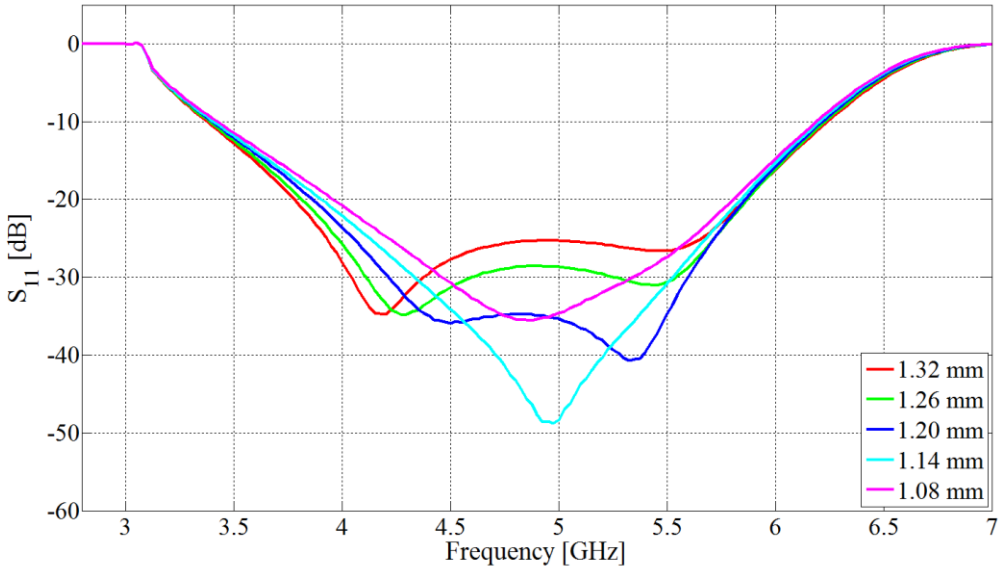

Figure 3.41. Simulated reflection coefficient for different probe diameters.

Despite the cyan coloured line (1.14 mm) reaching a deeper global minimum, it is not the optimum as the blue line (1.20 mm) has slightly better values over the rest of the band. Figure 3.42 shows the effect of different probe diameters on the simulated insertion loss.

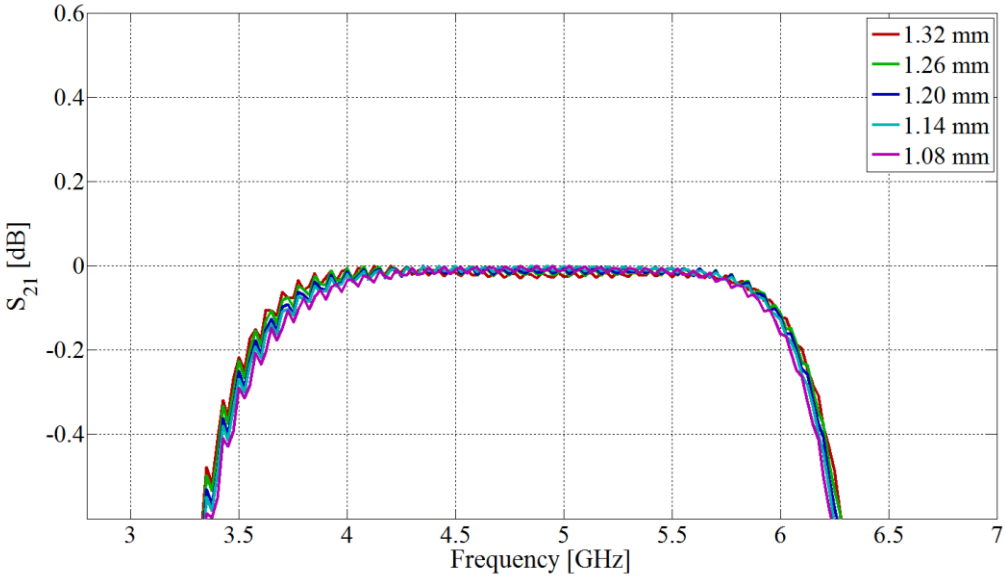

Figure 3.42. Simulated transmission coefficient for different probe diameters.

Note that the insertion loss appears to be slightly more sensitive at the lower end of the band.

3.3.10 Probe end gap

The distance between the end of the probe and the waveguide's side wall is defined as probe end gap dimension as shown in figure 3.43.

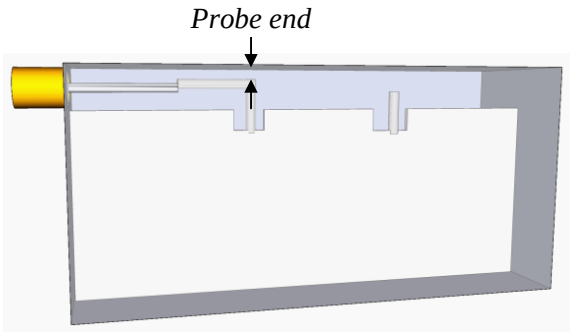

Figure 3.43. Probe end gap dimension definition.

As in the case of the SMA connector offset and probe feeder offset, the physical constraint is set at 0.5 mm for this parameter, due to manufacturing tolerances and power handling concerns. Figure 3.44 below gives the input impedance for the various probe end gap sizes.

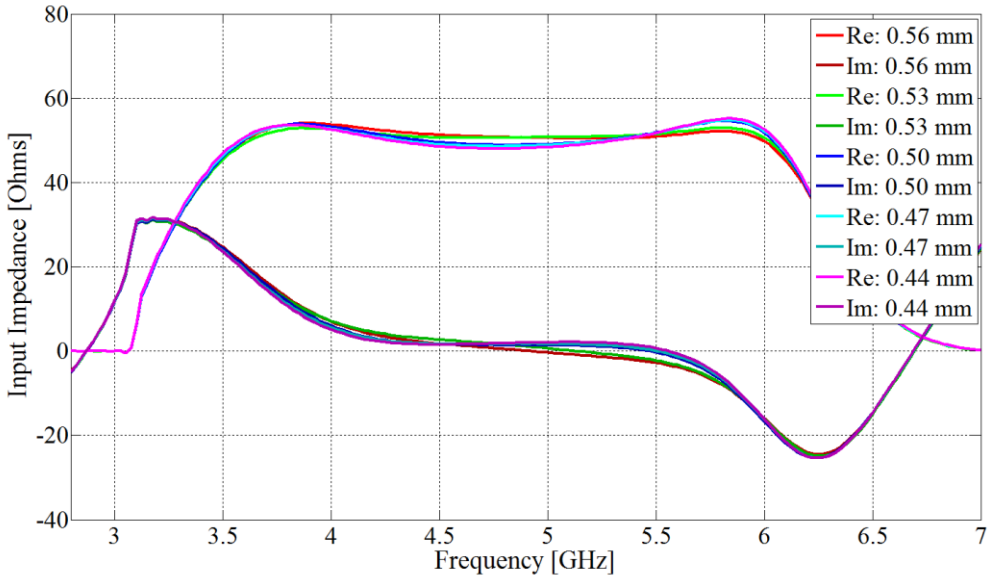

Figure 3.44. Complex input impedance for different probe end gap values.

Note that a larger gap size increases the real component of the input impedance and the smaller sizes yield decreased real component values. Lastly the complex component of the input impedance varies the most with larger gap sizes.

Figure 3.45 gives the reflection coefficient for the different post end gap dimensions.

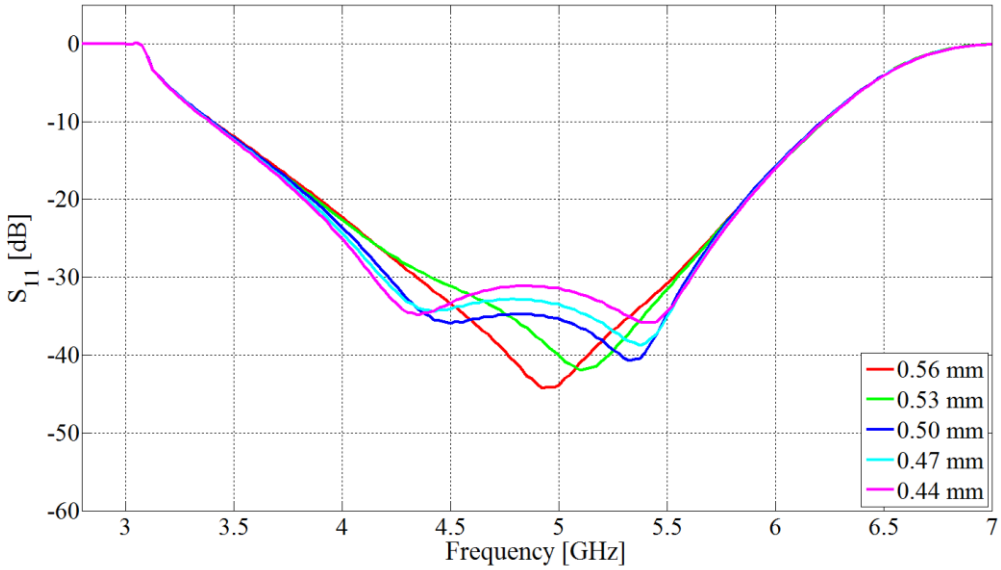

Figure 3.45. Simulated reflection coefficient for different probe end gap values.

Figure 3.46 shows simulated insertion loss for the various probe end gap sizes.

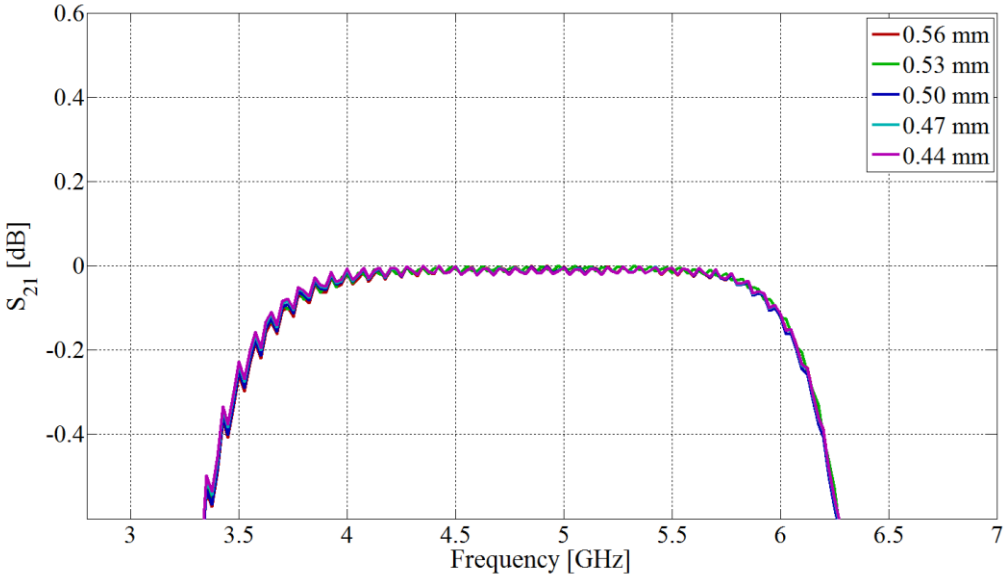

Figure 3.46. Simulated transmission coefficient for different probe end gap values.

From the simulated input impedance, reflection coefficient and insertion loss the design appears to be insensitive to variations in the probe end gap.

3.3.11 Post position

The post position is defined as the distance between the centre of the post and the waveguide's shorting wall, as shown in figure 3.47.

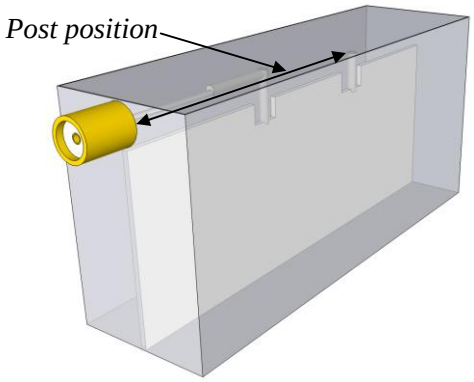

Figure 3.47. Post position dimension definition.

Figure 3.48 gives the input impedance for various post positions. Note that input impedance appears to be highly sensitive to this parameter with large fluctuations in both the real and imaginary components.

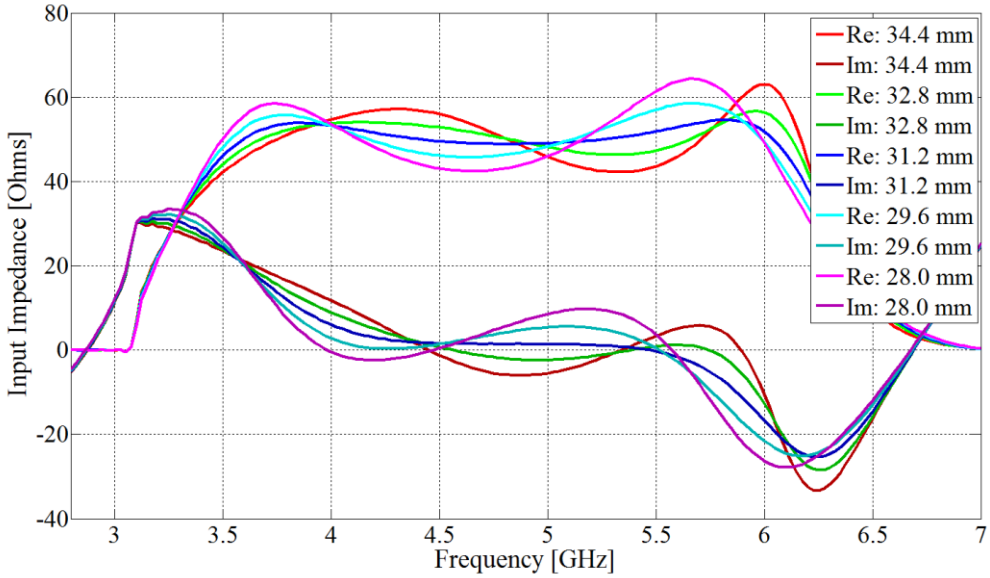

Figure 3.48. Complex input impedance for different post positions.

Since the post position sets the resonance frequency of the post is expected to be a sensitive parameter.

The reflection coefficient for the various post positions are given below in figure 3.49.

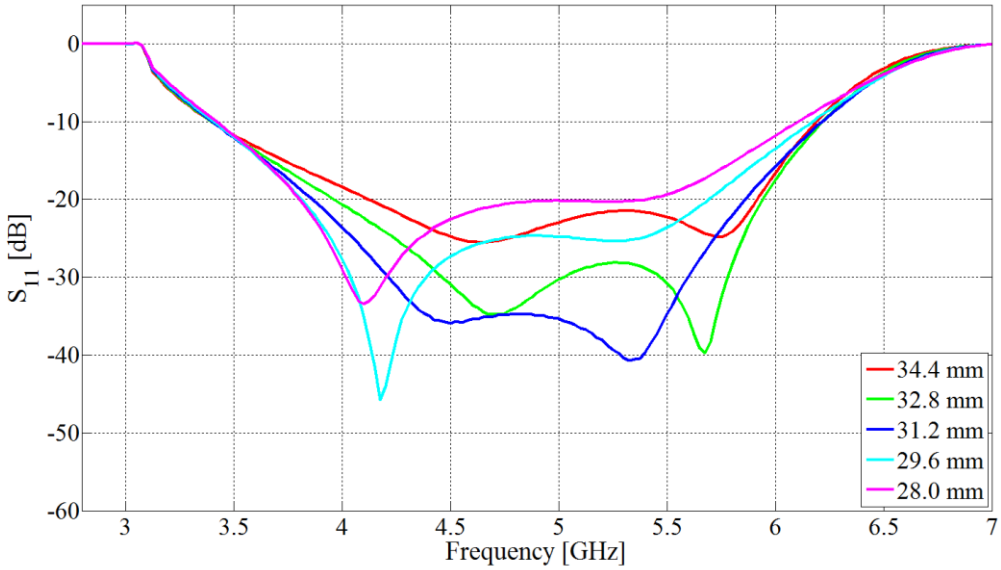

Figure 3.49. Simulated reflection coefficient for different post positions.

From the simulated input impedance and return losses, it can be seen that the higher of the two frequency resonances is controlled by the parameters related to post. Figure 3.50 shows the effect of different post positions on the simulated insertion loss.

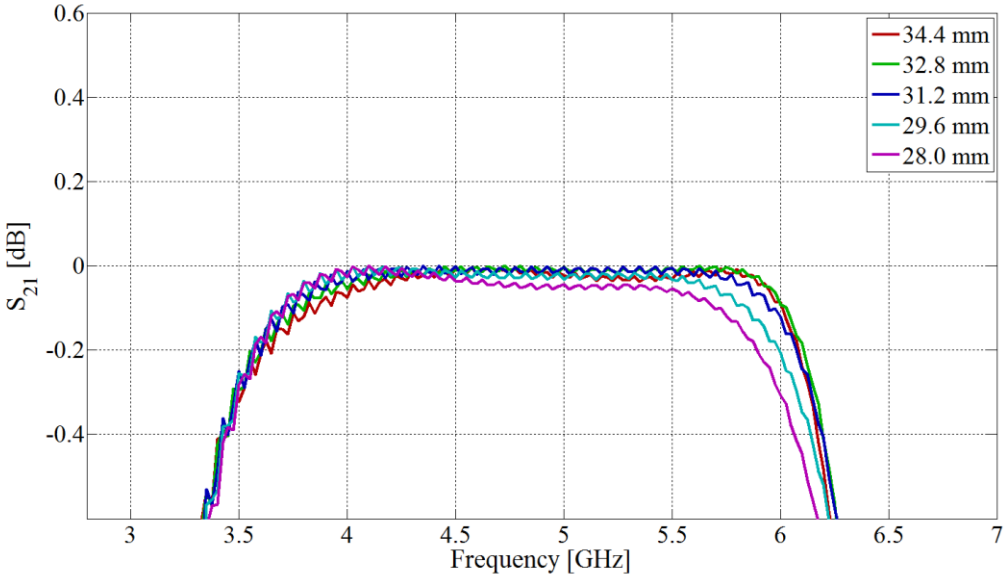

Figure 3.50. Simulated transmission coefficient for different post positions.

Note that the shorter post, positions yield higher insertion losses.

3.3.12 Post cut-out depth

The definition of the cut-out depth for the tuning post is given below in figure 3.51.

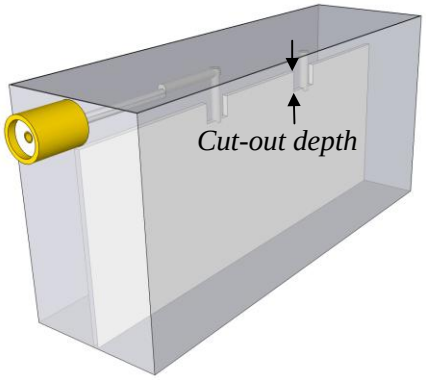

Figure 3.51. Post cut-out depth dimension definition.

The post cut-out depth is the depth that the post can extend into the H-plane vane. Figure 3.52 below gives the input impedance for increased and decreased depths.

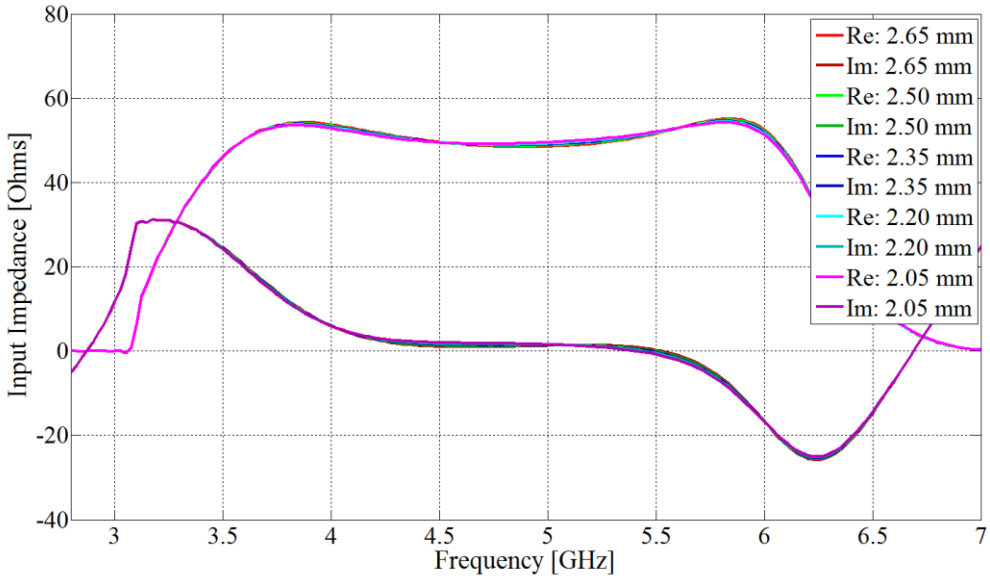

Figure 3.52. Complex input impedance for different post cut-out depths.

From the minimal input impedance variation for varied post cut-out depths it appears that the prototype is highly insensitive to post cut-out depth parameter variations.

The reflection coefficient for the various post cut-out depths is given in figure 3.53.

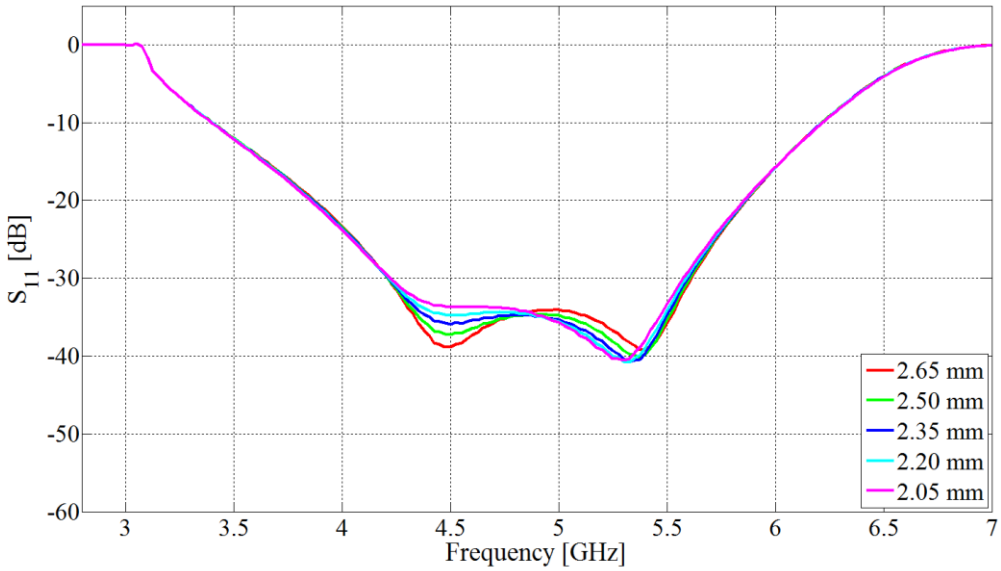

Figure 3.53. Simulated reflection coefficient for different post cut-out depths.

Figure 3.54 shows the effect of different post cut-out depths on the simulated insertion loss.

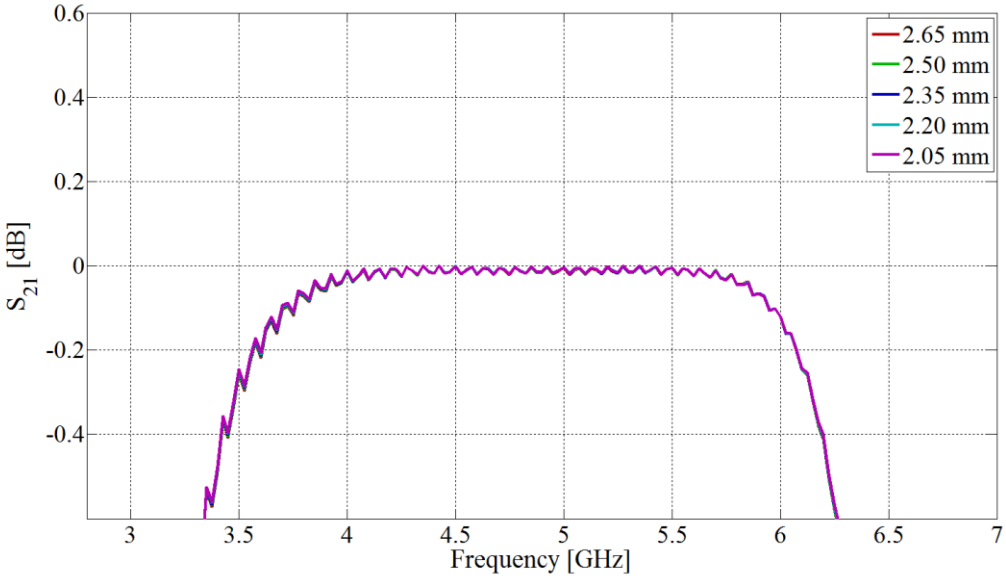

Figure 3.54. Simulated transmission coefficient for different post cut-out depths.

From the simulated input impedance, reflection coefficient and insertion loss, it can be seen that the post cut-out depth is one of the least sensitive parameter explored in this parameter study.

3.3.13 Post cut-out width

The post cut-out width is defined as the width of the notch around the post as shown in figure 3.55. As with the probe cut-out width, the parameter constraint is set as a minimum width of 1.6 mm, since the post diameter is the same as the probe diameter.

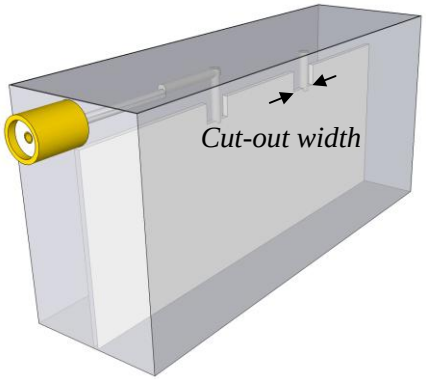

Figure 3.55. Post cut-out width definition.

Figure 3.56 below gives the input impedance for different cut-out widths around the post. The input impedance appears to be highly insensitive to variations in the post cut-out width.

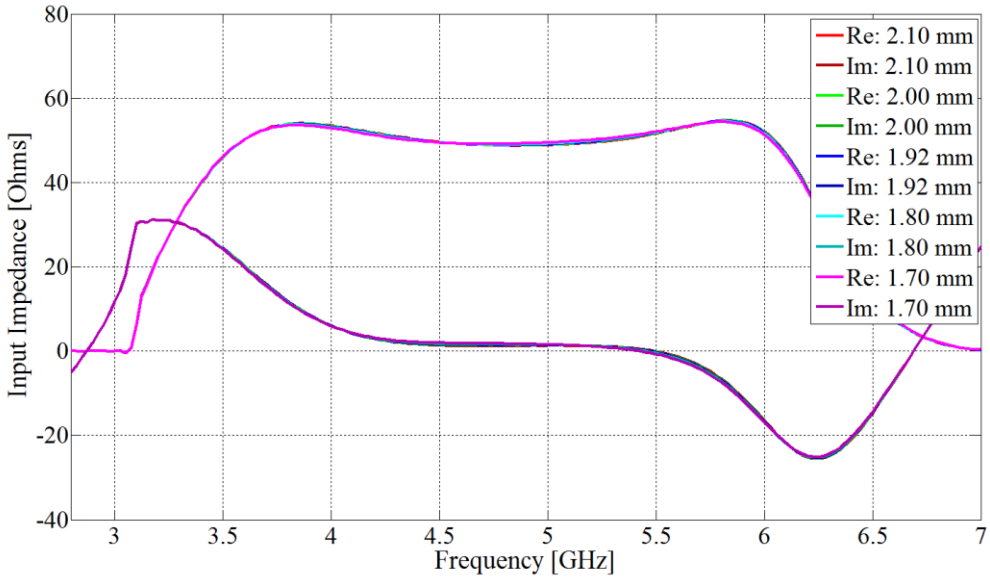

Figure 3.56. Complex input coefficient for different post cut-out widths.

The reflection coefficient for the various post cut-out widths are given in figure 3.57 and also shown that this parameter is relatively insensitive to variations.

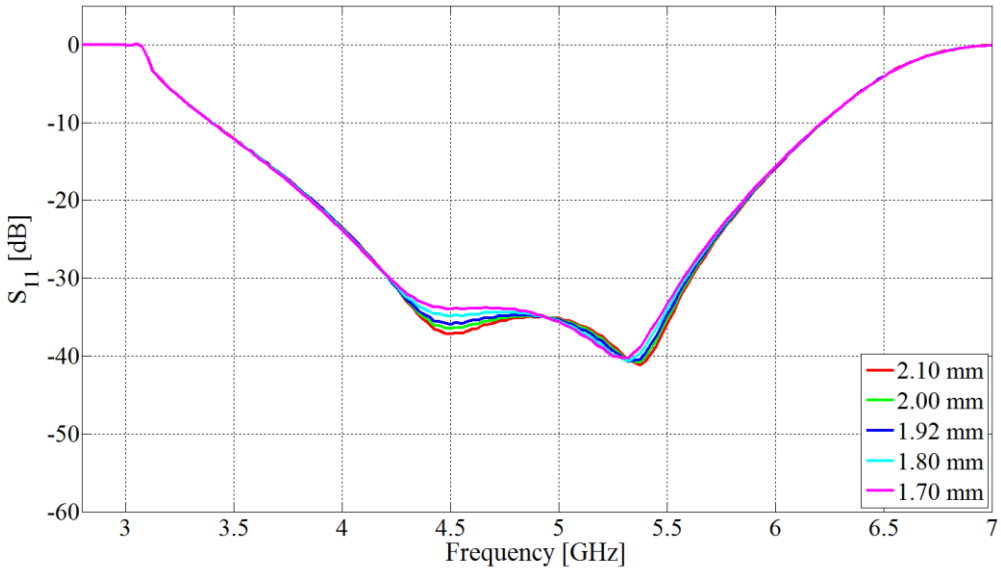

Figure 3.57. Simulated reflection coefficient for different post cut-out widths.

Figure 3.58 shows the effect of different post cut-out widths on the simulated insertion loss.

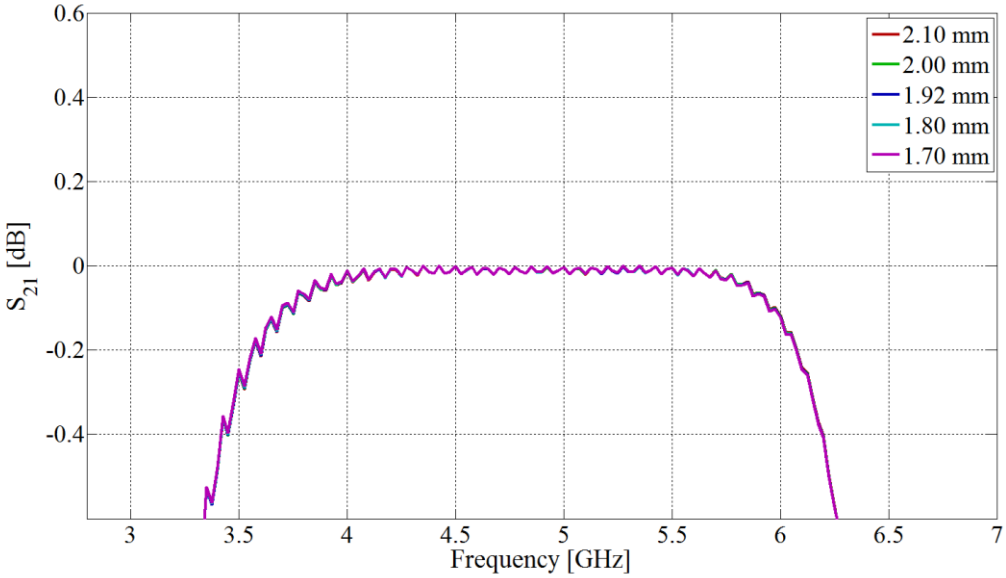

Figure 3.58. Simulated transmission coefficient for different post cut-out widths.

From the simulated results above, it can be seen that the post cut-out width is the least sensitive parameter in the prototype.

3.3.14 Post diameter

The post diameter dimension is simply the diameter of the rod that forms the tuning post as shown in figure 3.59. For convenience the post diameter was selected to be the same as the probe diameter (1.20 mm).

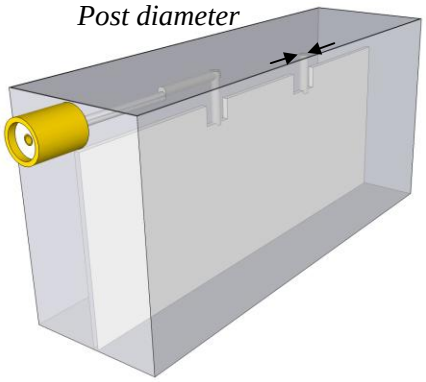

Figure 3.59. Post diameter dimension definition.

Figure 3.60 gives the input impedance for various post diameters. Note that the larger diameters lead to a larger real component (red line in the figure) in the middle of the band, whilst a smaller diameter (magenta line) decreases the real component.

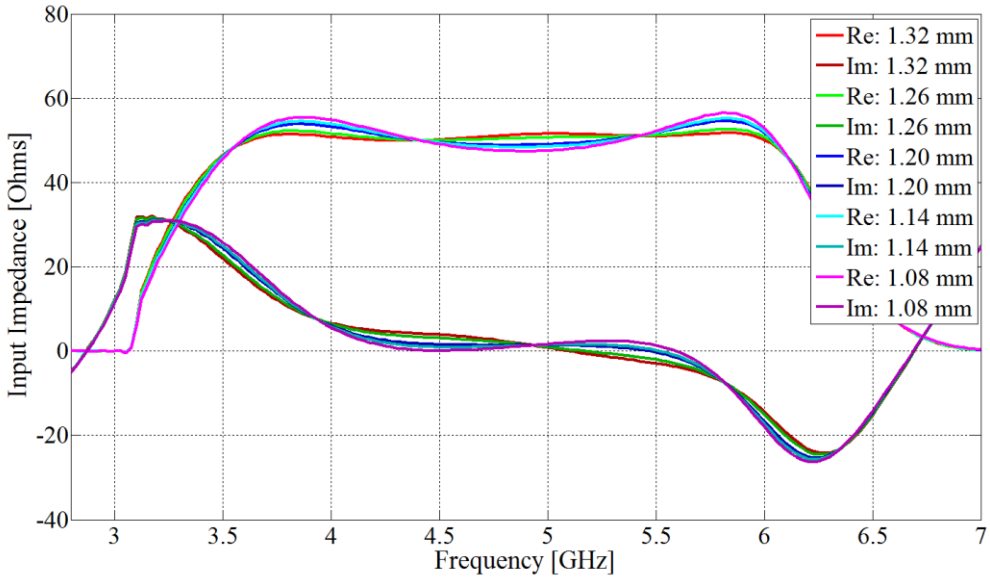

Figure 3.60. Complex input impedance for different post diameters.

The smaller diameters appears to have significantly less imaginary component variation over the band of interest compared to the larger diameter posts.

The reflection coefficient for the various post diameters are given in figure 3.61 below.

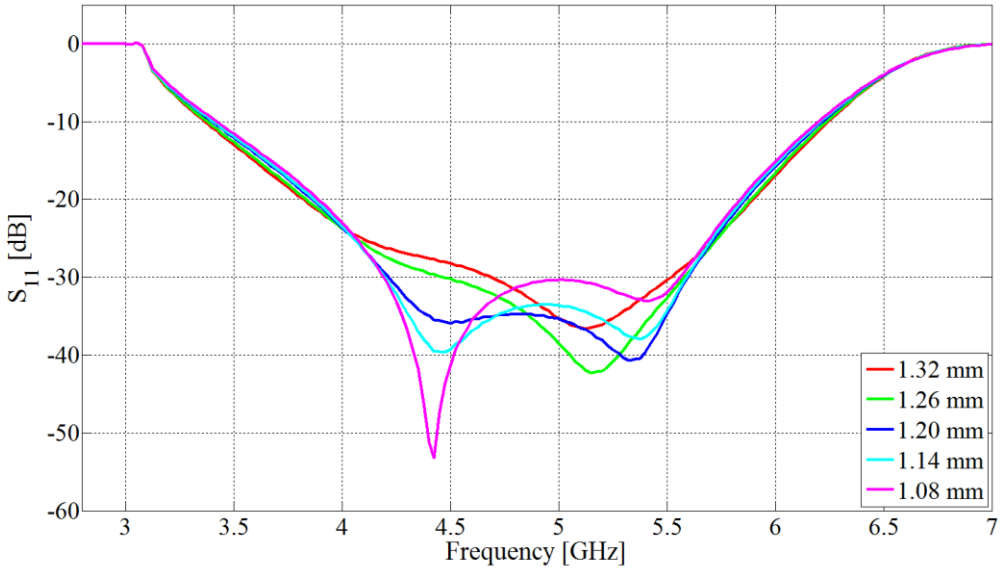

Figure 3.61. Simulated reflection coefficient for different post diameters.

Figure 3.62 shows the effect of different post diameters on the simulated insertion loss.

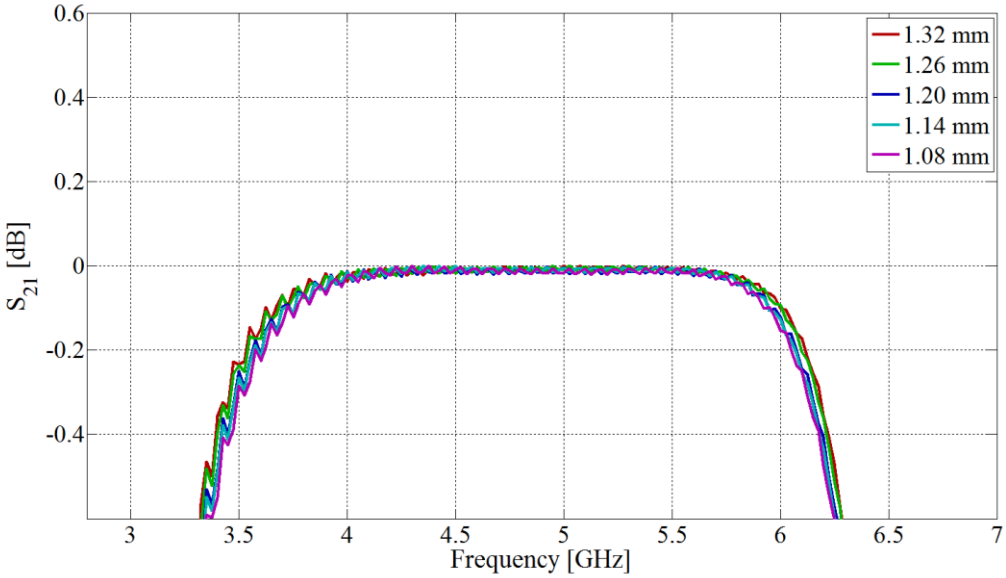

Figure 3.62. Simulated transmission coefficient for different post diameters.

From the input impedance and reflection coefficient graphs above it can be seen that the post diameter parameter is moderately sensitive.

3.3.15 Post end gap

The distance between the end of the post and the waveguide's side wall is defined as the post end gap dimension as shown in figure 3.63.

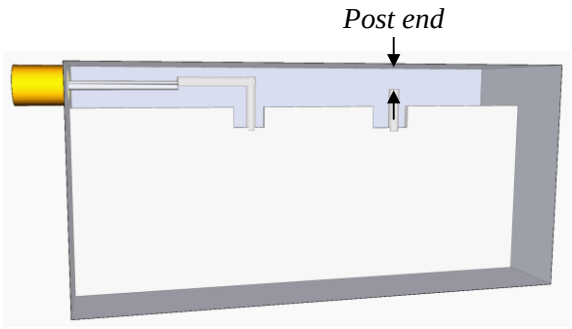

Figure 3.63. Post end gap definition.

As in the case of the SMA connector offset, probe feeder offset, and probe end gap the physical constraint is set at 0.5 mm for this parameter, due to manufacturing tolerances and power handling concerns. Figure 3.64 below gives the input impedance for the various post end gap sizes.

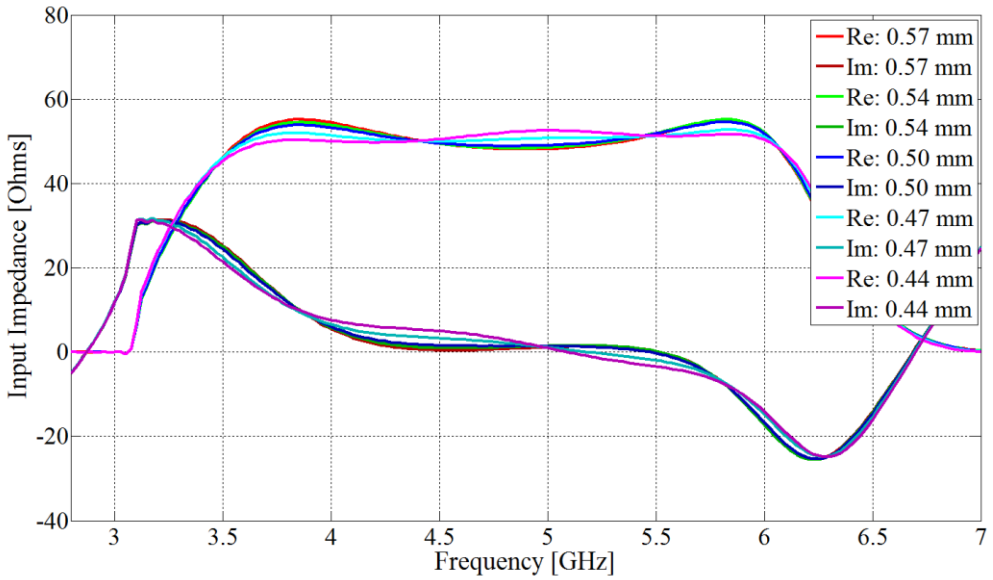

Figure 3.64. Complex input impedance for different post end gap sizes.

The figure shows that smaller gaps lead to a higher real component at mid-band and a larger gap leads to a lower real component (below 50 Ω). Lastly note that the larger gaps

tend to have less variation in the complex component of the input impedance. From the input impedance it can be seen that the design is moderately sensitive to parameter variations. Figure 3.65 gives the simulated reflection coefficient for the different post end gap sizes.

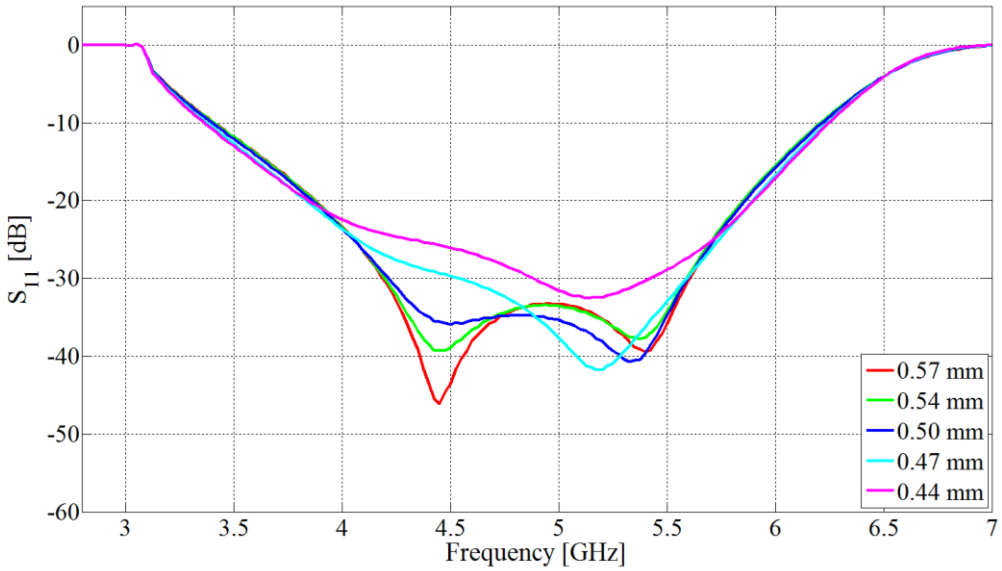

Figure 3.65. Simulated reflection coefficient for different post end gap sizes.

Figure 3.66 shows the effect of different post end gaps sizes on the simulated insertion loss.

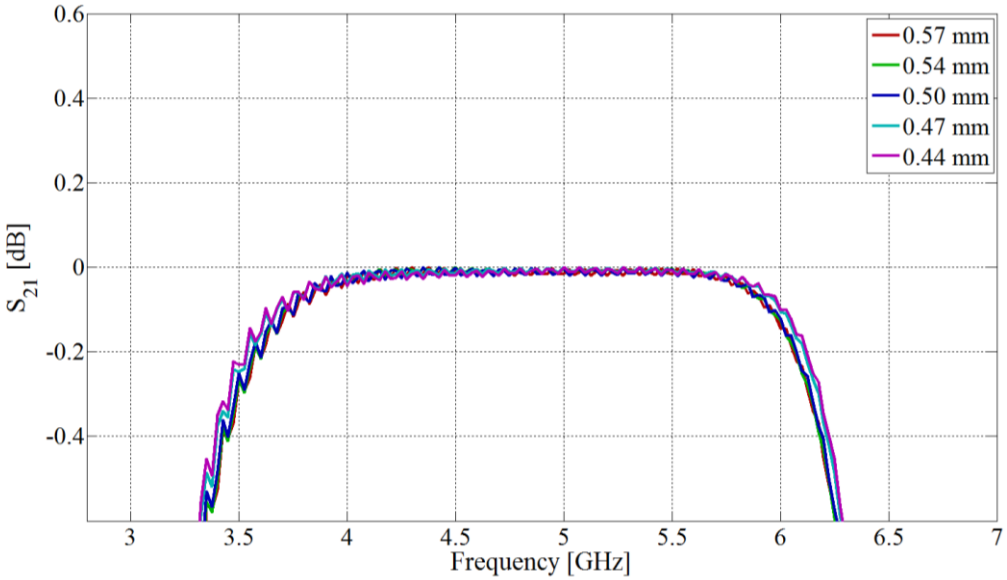

Figure 3.66. Simulated transmission coefficient for different post end gap sizes.

3.3.16 Parametric study summary

Table 3.1 summarises the effect of the various parameters investigated. The sensitivities are classified as either insensitive, moderately sensitive, highly sensitive, or extremely sensitive. The sensitivities in the table are mainly referring to the reflection coefficient as the insertion loss is insensitive to most parameters.

Table 3.1. Parameter study summary.

Parameter	Optimum value [mm]	Sensitivity	Notes
SMA offset	1.34	High	Larger values decrease real impedance component and vice versa.
Feed-line length	8.90	Moderate	Formed from extended SMA connector dielectric and centre conductor.
Probe feeder offset	1.13	Extreme	This is sets the impedance of the matching section and is the most sensitive parameter.
Probe position	22.13	Extreme	This sets the resonant frequency of the probe.
Probe cut-out depth	2.24	Insensitive	This sets the length of the probe which could influence the major resonant frequency.
Probe cut-out width	1.93	Moderate	Insertion loss is insensitive.
Probe diameter	1.20	Moderate	Design goal is 1.20 mm for convenience.
Probe end gap	0.50	Insensitive	Larger gap sizes increase the real component of the input impedance, and vice versa.
Post position	31.24	High	This sets the higher resonant frequency (post).
Post cut-out depth	2.35	Insensitive	This sets the length of the post and could influence the post resonant frequency.
Post cut-out width	1.92	Insensitive	Least sensitive parameter.
Post diameter	1.20	Moderate	Input impedance imaginary component is effected less by smaller diameters.
Post end gap	0.52	Moderate	Less than 0.50 mm constraint.

3.4 PROTOTYPE REALISATION

This section describes the process followed to realise the prototype end-launched partial H-plane waveguide adapter. The purpose of realising the prototypes in hardware is to facilitate measurements to confirm the simulation results. Since partial H-plane waveguide components are not currently commercially available and no previous full band adapters have been developed, the prototype realised will consist of two transitions in the back-to-back configuration.

For simplicity and ease of manufacturing the material used to fabricate the prototypes was brass. The waveguide wall thickness was selected as 6 mm as this would allow the use of 2.5 mm cap screws to bolt the prototype together. The 6 mm wall thickness facilitates the cap of the screw not overhang the sides and have ample materiel thickness on either side of the holes for mechanical rigidity. Figure 3.67 below shows a three-dimensional model of the coaxial end-launched prototype.

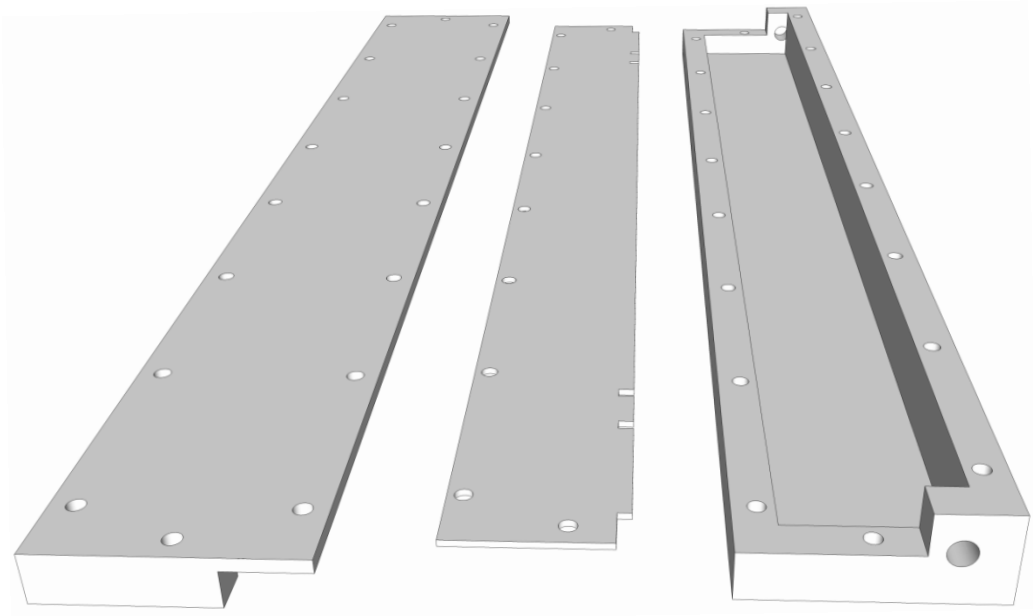

Figure 3.67. CAD model of end-launched prototype.

Figure 3.67 shows from left to right, the top cover, H-plane vane and bottom cover. The figure was drawn using the commercially available SketchUp CAD software. The thickness of the vane was selected as 1 mm as it was mechanically stiff and facilitated fine machining. From an electromagnetic point of view a very thin vane is desired as mentioned

in [3], where a 0.1 mm was used. However an initial prototype fabricated using the same 0.1 mm vane thickness did not yield satisfactory results as the vane was too flexible and did not maintain its shape. The 0.1 mm vane used in [3] was used to fabricate a filter where the vane was electrically and mechanically connected (or shorted) to the side walls of the waveguide at several points which gave additional mechanical support to the vane, which was not present in this study as we are concerned with realising a general purpose waveguide section between two prototype adapters.

The length of the partial H-plane waveguide that separates the two prototype adapters was selected as 237 mm, which is approximately two guided wavelengths at the middle of H-band. The separation distance of two guided wavelengths was selected to ensure that the two adapters did not negatively influence each other. Two photographs of the completed coaxial prototype are shown in figure 3.68 and figure 3.69.

Figure 3.68. Photograph of the inside of the coaxial prototype.

Note the use of solder to attach the feed-line to the matching section. Solder was additionally used to attach the probe and post to the H-plane vane. Although utilising these solder joints did increase inaccuracy in the prototype, they facilitated the final tuning and simple assembly and disassembly during measurements.

Figure 3.69. Photograph of the exterior of the completed end-launched prototype.

The figure above shows the exterior of the final end-launched coaxial prototype.

3.5 RESULTS

The results obtained through measurements of the realised end-launched coaxial prototype are documented in this section. Figure 3.70 below shows the calibration setup used to calibrate the Rohde & Schwarz ZVA40 vector network analyser.

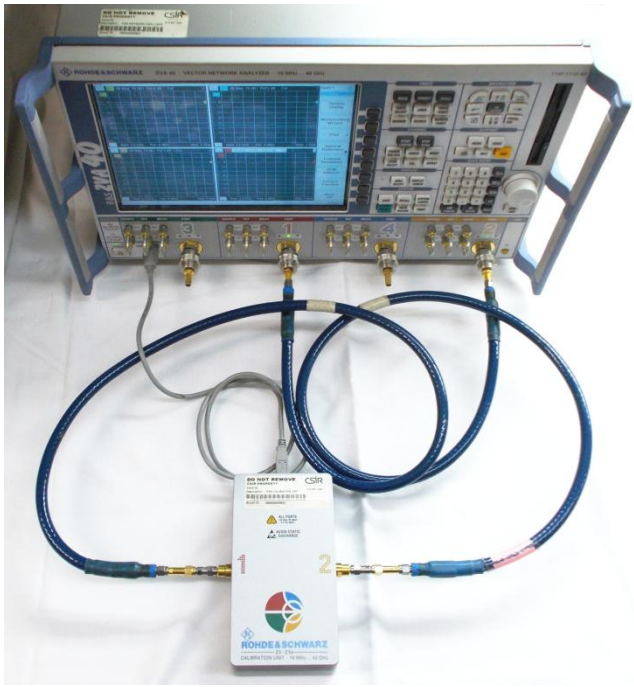

Figure 3.70. Vector network analyser calibration setup photo.

The instrument was calibrated using the automatic calibration method with the supplied two port calibration kit. The calibration was performed to ensure that accurate measurements were made with the reference point set at the SMA connectors at the end of the coaxial cable. Figure 3.71 shows the prototype connected to the measurement instrument.

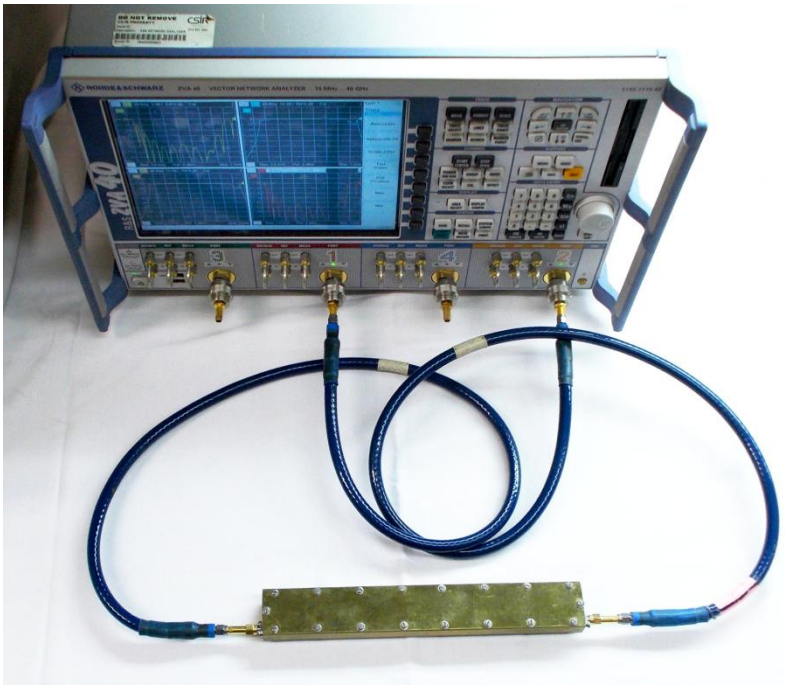

Figure 3.71. Coaxial prototype connected to the vector network analyser.

Port one on the prototype is defined as the left hand SMA connector and the second port is the right hand port as shown in figure 3.71**.**

3.5.1 Back-to-back results

The two port measured results for the back to back configuration are given together with simulated results in figure 3.72.

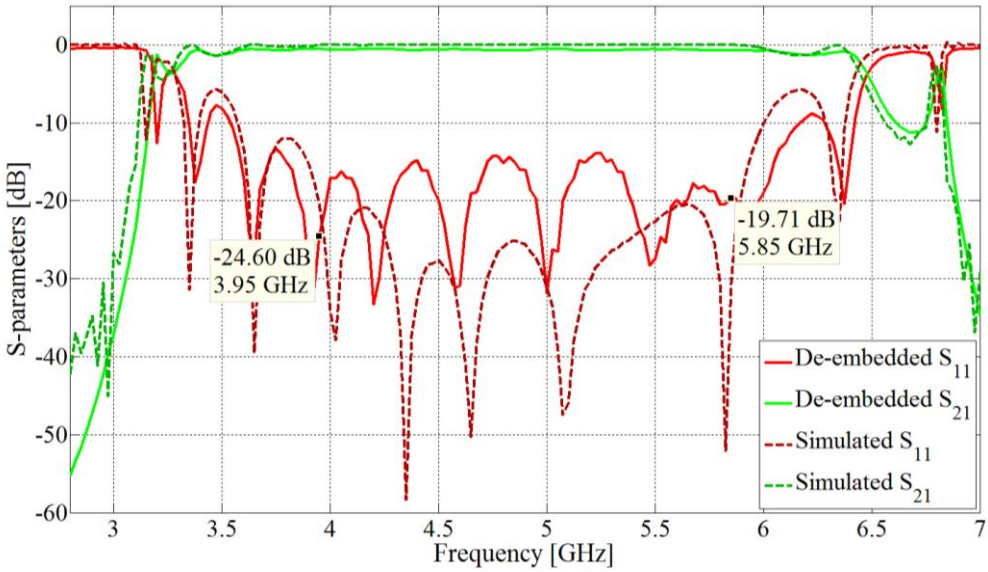

Figure 3.72. Two port back-to-back measured and simulated results.

The brightly coloured red and green solid lines in figure 3.72 are the measured return and insertion losses respectively. Similarly the dull red and green dashed lines are the simulated return and insertion losses respectively. The maximum (worst case) measured reflection coefficient within the band of interest (3.95 to 5.85 GHz) is -14 dB and the highest insertion loss achieved is 0.75 dB within the same band.

The reason for the back-to-back results having a different shape when compared to the simulated single ended results given in section 3.2.4 is that the combined reflection coefficient response is the result of constructive and destructive interference between the two transitions on either side of the realised prototype partial H-plane waveguide.

3.5.2 Propagation constant used for de-embedding

In order to estimate the single ended response through the de-embedding technique the propagation constant within the waveguide is required. In conventional rectangular waveguides the propagation constant can solved through using different lengths of waveguide between the two adapters [44]. This is possible since convention waveguide adapters can be bolted onto different lengths of transmission line through the standard flange mounts; therefore the only variable is the length of waveguide. In the partial H-plane waveguide scenario there is no standard interface or connector mechanism available to separate the prototype adapters from the waveguide section between them and insert different lengths.

In order to overcome this limitation the simulated propagation constant was used as an initial baseline and adjusted until the cut-off frequencies of the first (dominant) and second propagating modes matched the measured cut-off frequencies. If incorrect cut-off frequencies are used during de-embedding the extracted single ended response will have large discontinuities between the actual and simulated cut-off frequencies. This behaviour facilitated checking that the correct propagation constant was used during de-embedding. The initial baseline and final de-embedding propagation constants used to extract the single ended results are given in figure 3.73. Note that the de-embedding cut-off frequencies are below the simulated baseline cut-off frequencies.

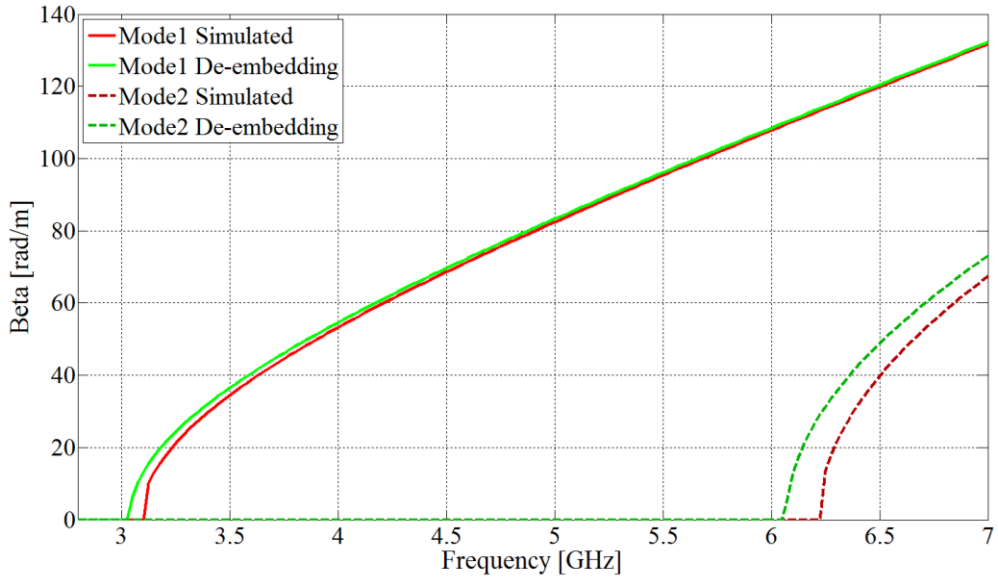

Figure 3.73. Initial simulated baseline and de-embedding propagation constants.

3.5.3 De-embedded single adapter results

The de-embedded approximate single adapter results are given below in figure 3.74. The de-embedded results are based on the propagation constant discussed in the previous section and the assumption that the two adapters in the prototype are identical.

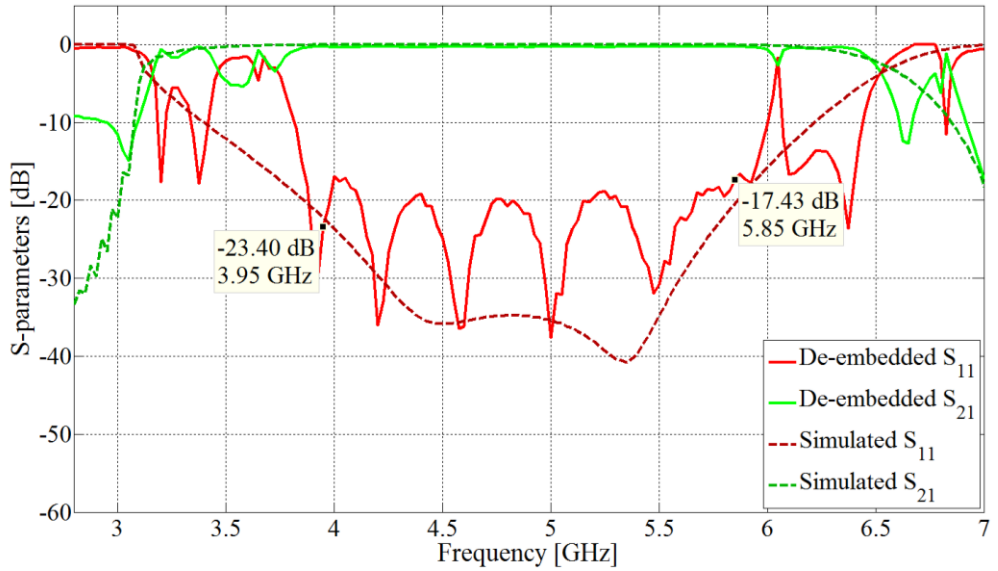

Figure 3.74. Measured and simulated single adapter S-parameters.

The maximum reflection coefficient within H-band is -17 dB and the maximum insertion loss is 0.75 dB.

The de-embedded approximate single adapter input impedance results are given below in figure 3.75. The red lines in the figure represent the real component of the input impedance and the green lines represent the imaginary component.

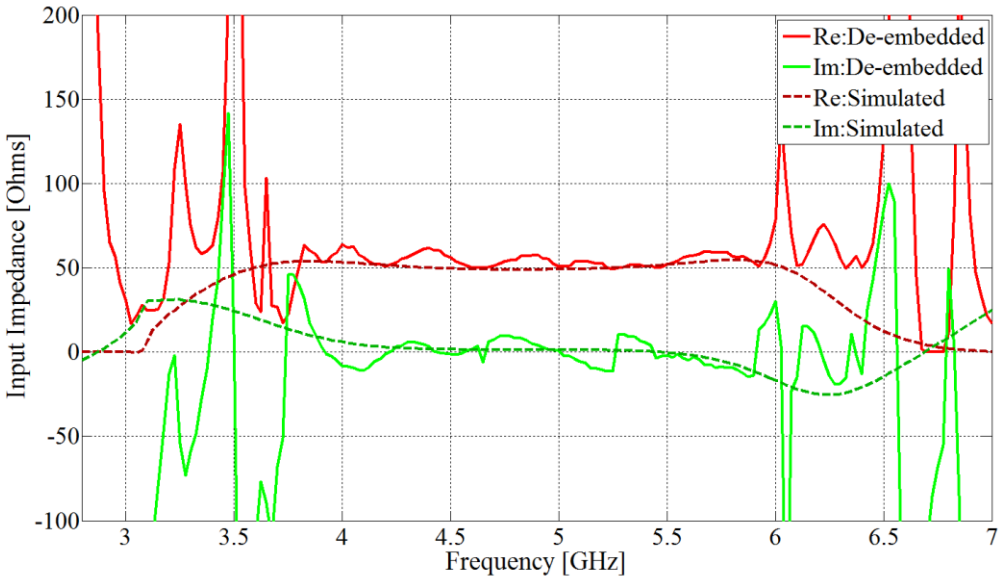

Figure 3.75. Measured and simulated **s**ingle adapter input impedance.

Note that the de-embedded imaginary component of the input impedance appears to be centred around zero over the band of interest (3.95 to 5.85 GHz) as desired. The de-embedded real component is reasonably flat over the band of interest but is slightly too high and is centred around 55 Ohms instead of the desired 50 Ohms.

From the parameter summary table 3.1 it is plausible that the real component is slightly too high due to the realised SMA offset parameter being under the optimal value of 1.34 mm.

3.6 DISCUSSION

This chapter has documented the development of the end-launched coaxial to partial H-plane waveguide adapter from concept development through to measurements of the realised prototype. The concept development started off with the simple L-shaped loop and evolved with the addition of a cut-out to increase the length of the probe, an impedance matching section, and finally a tuning post to increase the simulated bandwidth to cover the entire band. A parameter study was conducted to determine which parameters were the most sensitive and which parameters are insensitive. The parameter study concludes with a table which summarises the sensitivity of all of the parameters, with the probe position and feed offset (sets the characteristic impedance of matching section) being declared the most sensitive parameters in the design. CAD design models and photographs of the realised prototype were given in section 3.4.

Lastly, the measured results obtained from laboratory measurements of the realised prototype are presented in section 3.5. As previously discussed the prototype was realised in the back-to-back configuration to facilitate insertion and return loss measurements. The measured two port return loss and insertion losses are 14 dB and 0.75 dB; note that these are the worst case results over the entire band. Despite the simulated results being 20.4 dB and 0.06 dB respectively, the shape and values (to a lesser degree) of the measured results still compare favourably with the simulation results. The approximate single ended adapter response was obtained through de-embedding using the approximate propagation constant in section 3.5.2 and the assumption that the two realised transitions in the prototype are identical. The approximate singled adapter result has an insertion loss of 0.75 dB and a reflection coefficient of -17 dB, compared to the simulated values of 0.05 dB and -20.38 dB respectively. Despite the single adapter results not achieving the design goal of an insertion loss of less than 0.5 dB and a reflection coefficient less than -20 dB, the results obtained still confirm the validity of the design. The difference between the measured and simulated results can be attributed to manufacturing tolerances and imperfections in the materials. Note that the poor manufacturing tolerances are a result of the use of several solder joints in the design.

CHAPTER 4 MICROSTRIP TO WAVEGUIDE ADAPTER

4.1 INTRODUCTION

In chapter 3 the development of the end-launched coaxial to partial H-plane waveguide adapter was discussed and measured results were given for the fabricated prototype. Similarly in this chapter the development of a microstrip adapter to partial H-plane waveguide will be discussed. As with the coaxial adapter the microstrip adapter will be designed for and measured in H-band (3.95 to 5.85 GHz) to facilitate comparisons between previously existing partial H-plane waveguide adapters.

4.2 CONCEPT DEVELOPMENT

The integrated broadside microstrip adapter from chapter 2 was selected as the feed structure to adapt to the partial H-plane scenario due to large potential bandwidths and simplicity as the entire feed structure may be integrated on a single microstrip substrate. Additionally this conventional waveguide to microstrip adapter is essentially a modified probe feed which is similar to the broadside coaxial probe used in [10] (figure 2.2). Similar to the coaxial partial H-plane waveguide adapter, the probe part of the feed structure should be inserted above the vane, where the E-field is at a maximum.

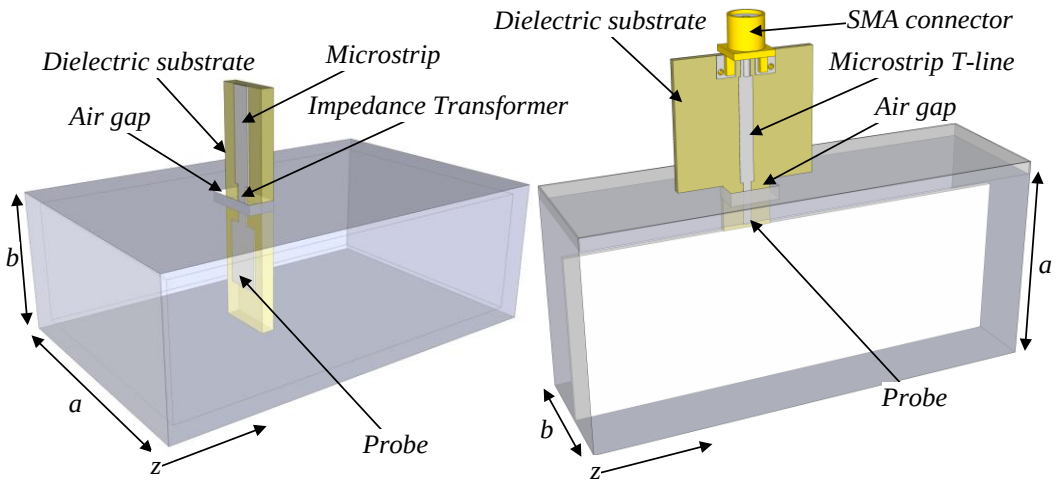

(a) (b)

Figure 4.1. Integrated microstrip probe in rectangular (a) and partial H-plane (b) waveguides.

Figure 4.1 shows that the integrated broadside microstrip probe (a), used in conventional rectangular waveguides can be adapted for the partial H-plane geometry (b), by bending the conventional waveguide like a horseshoe. Note that the *a* and *b* dimensions are not equivalent in the two different waveguides in the figure and therefore the figures are not to scale. The partial H-plane is smaller with a quarter of the cross-sectional area since it's *a* and *b* dimensions are approximately half of the *a* and *b* of the conventional waveguide. The SMA connector in figure 4.1 (b) is specifically labelled as it is important to consider the microstrip to SMA transition required to perform measurements using the vector network analyser in the experimental setup given in chapter 2.

As previously mentioned the integrated microstrip probe is very similar to the coaxial probe used in [10]; it is interesting to note that the probe in [10] was optimised for narrowband performance as it was used in a band pass filter application [10]. If the adapter in [10] is optimised to cover the entire H-band the results in figure 4.2 can be obtained.

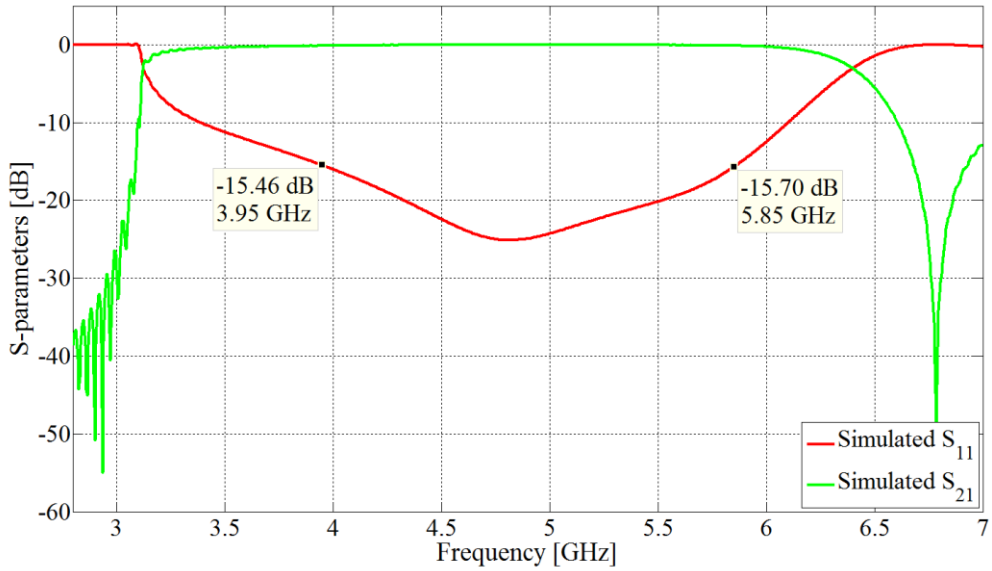

Figure 4.2. Simulated S-parameters for coaxial probe optimised over the entire H-band.

The results above were generated by optimising the dimensions of the feed in figure 2.2 [10] using CST Microwave Studio for minimal S_{11} over 3.95 to 5.85 GHz. The results in figure 4.2 show that a simple probe feed can be optimised to achieve a return loss of over 15 dB. This result is encouraging as a simple microstrip probe feed should achieve similar

results and is the basis from where a microstrip transition to the partial H-plane waveguide will be developed.

4.2.1 Coaxial to Microstrip transition

Since vector network analysers typically have coaxial connectors the prototype transition should terminate on the non-waveguide port with a coaxial connector to facilitate measurements. For convenience the SMA connector was selected as it is an industry standard. Rogers RO4003C with a thickness of 0.813 mm was selected as the microstrip substrate as it is readily available, relatively low cost, has low loss characteristics and a dielectric constant of 3.55 which yields microstrip lines of reasonable widths.

Initially the microstrip transition was designed and simulated without any vias using the dimensions of a commercially available SMA connector as shown in figure 4.3 (a). Note that the square face of the SMA edge connector is continued until the end of the connector as it simplified the simulation geometry and did not negatively affect the simulation results as the outside shape of the coaxial structure does not play a role in the internal electromagnetic fields.

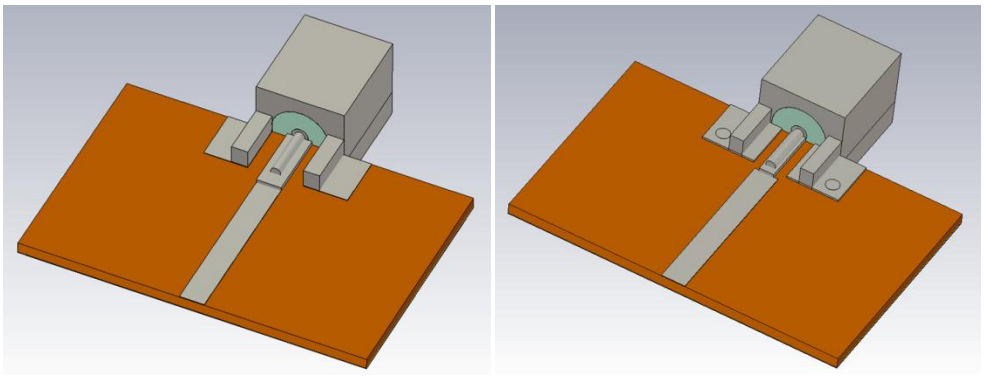

(a) (b)

Figure 4.3. CST model of SMA to microstrip transition, without (a) and with grounding vias (b).

The track width in figure 4.3 (a) is a constant width of 1.78 mm which yields a 50 Ω characteristic impedance; in addition to the two vias in figure 4.3 (b) the strip width between the two legs of the connector is narrowed to 1.10 mm. These two modifications

overcome the negative capacitive effects of the floating connector legs. The simulated S-parameters of the two transitions are given in figure 4.4.

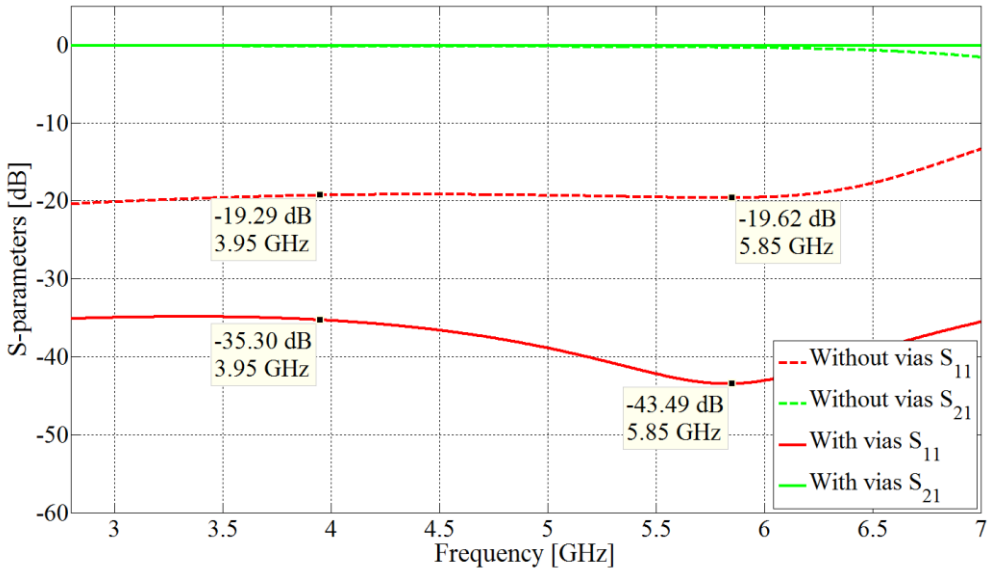

Figure 4.4. Simulated S-parameters of SMA to microstrip transition, with and without vias.

Note that the reflection coefficient without and with vias are -19 dB and -35 dB respectively; the transmission coefficient (S_{21}) with the vias is also flatter. Given these significant improvements the prototype waveguide transition was fabricated with these improvements to minimise the effects of the microstrip to coaxial transition on the measured results.

4.2.2 Microstrip probe

The probe feed geometry given in figure 4.1 (b) consists of a 50 Ω microstrip line up to the waveguide's external wall and a probe integrated onto the same substrate going through a hole in the waveguide's side wall. The air gap above the substrate in figure 4.1 (b) and the substrate width going through the waveguide wall were optimised to be as small as possible without negatively affecting the return loss. The probe width and position from the shorting wall were also optimised using CST MWS for the maximum return loss over the entire band. The simulated S-parameters in figure 4.5 were obtained for the optimised adapter. The minimum return loss occurs at the lower band edge and is 8 dB which is not sufficient for a general purpose adapter.

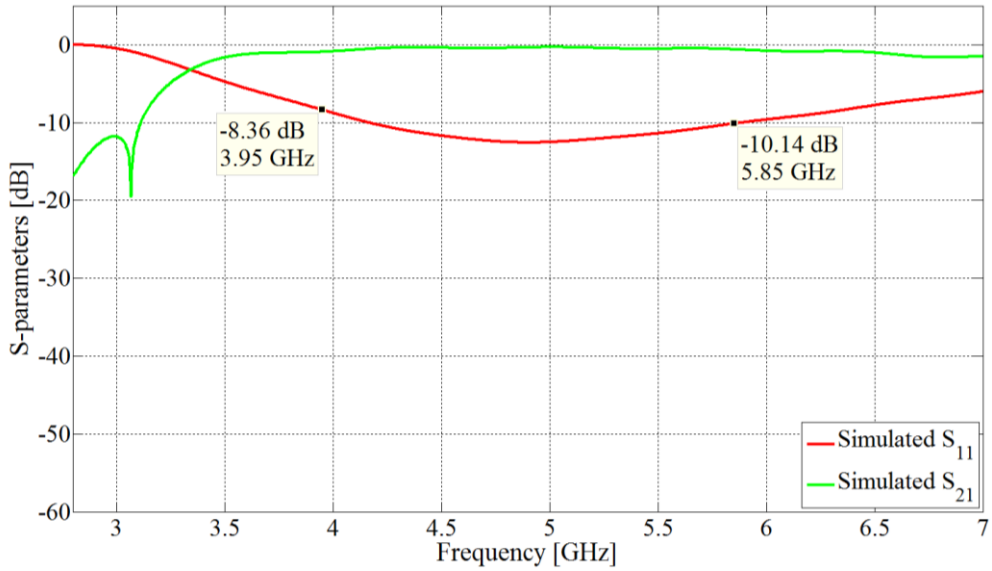

Figure 4.5. Simulated S-parameters after some optimisation in CST, for the microstrip probe transition.

The poor reflection coefficient performance of only -8.3 dB achieved above is a result of the length of the probe being too short as it can only utilise the gap between the side wall of the waveguide and the H-plane vane as shown in figure 4.1 (b), which is too short to achieve resonance.

4.2.3 Microstrip probe with cut-out

The length of the probe can be increased if a cut-out is introduced as shown in figure 4.6.

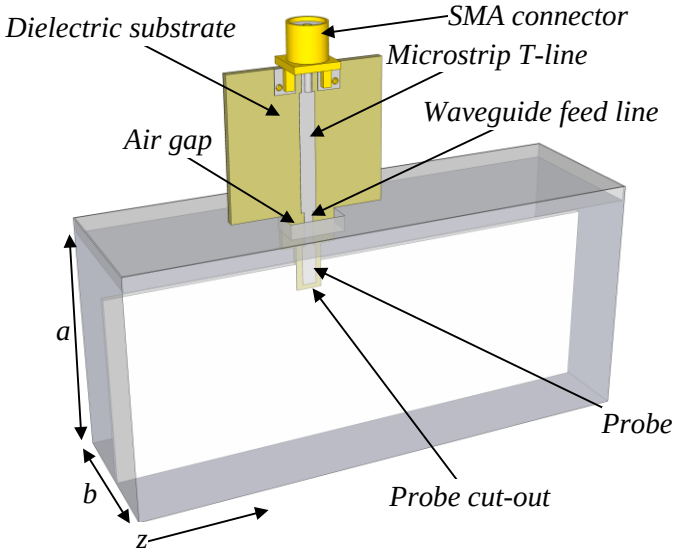

Figure 4.6. Microstrip adapter with probe cut-out.

The extended probe protrudes into the vane but does not make electrical contact with the vane. The substrate does however make mechanical contact with the vane to add mechanical stability. Note that it is possible to etch the feed structure and vane from a single double sided substrate with vias along the vane's leading edge. However for more general purpose use where the waveguide can be quite long this is not always feasible, but it can be useful when realising compact waveguide filters. The effect of lengthening the probe is given in figure 4.7, which is the simulated S-parameters of the geometry shown in figure 4.6.

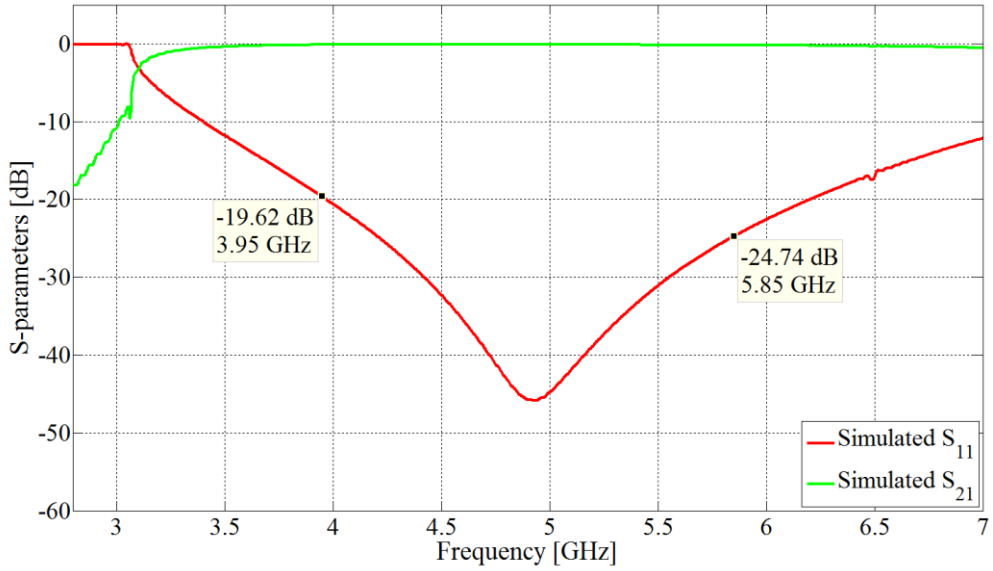

Figure 4.7. Simulated S-parameters for microstrip adapter with cut-out optimised for wide band operation.

The effect of increasing the length of the probe is dramatic with the maximum reflection coefficient simulated within the band of interest reduced from -8.3 dB to only -19.62 dB. In order to lower the reflection coefficient a matching section will be introduced into the feed structure in the following subsection.

4.2.4 With matching section

A matching section can be easily implemented in the microstrip section outside of the waveguide by changing the characteristic impedance of the microstrip line by varying the microstrip width. A narrower section has an increased characteristic impedance and a

wider section has a decreased characteristic impedance (see figure 4.12) when compared to the 50 Ω section. Figure 4.8 below shows the prototype geometry with the addition of the matching section.

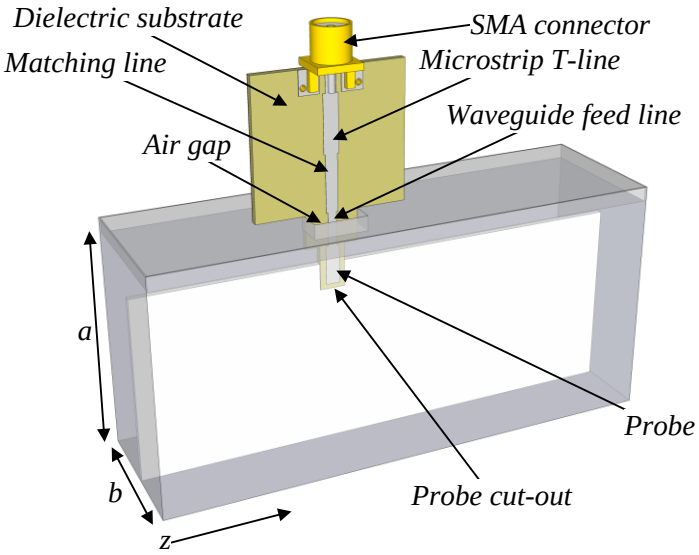

Figure 4.8. Microstrip transition with additional matching section.

The S-parameters of the modified geometry are given in figure 4.9 below.

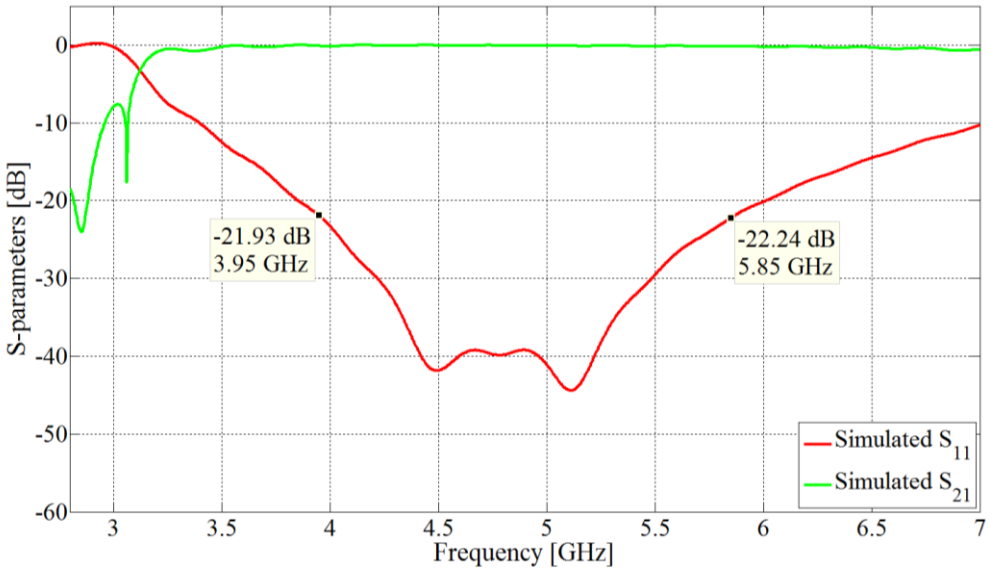

Figure 4.9. Simulated S-parameters for microstrip adapter with cut-out and matching section optimised for wide band operation.

The maximum in-band reflection coefficient has been improved to -21.9 dB which is not as significant as other additions to the prototype but will enable the next addition of a tuning post to yield vastly superior wideband performance.

4.2.5 Microstrip adapter with Post

The geometry of the prototype microstrip adapter with the introduction of a tuning post is given below in figure 4.10.

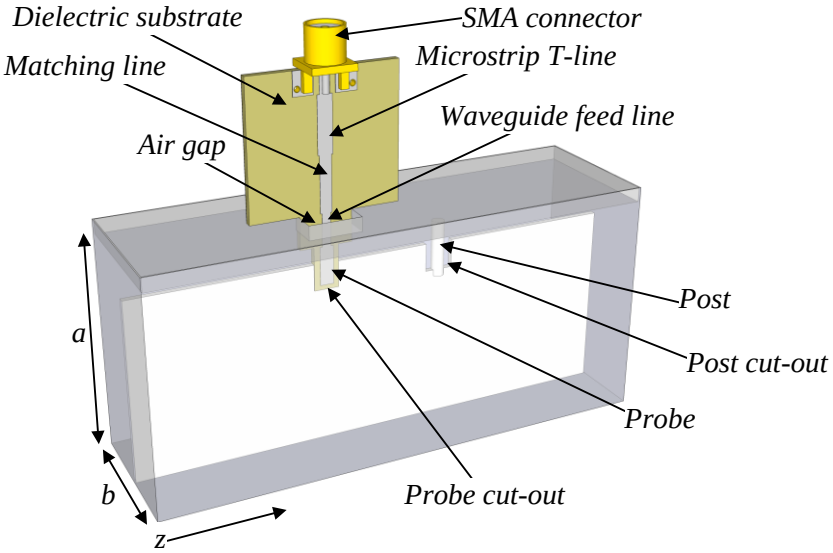

Figure 4.10. Microstrip transition with the addition of a post.

The simulated S-parameters of the prototype with the addition of a tuning post is shown below.

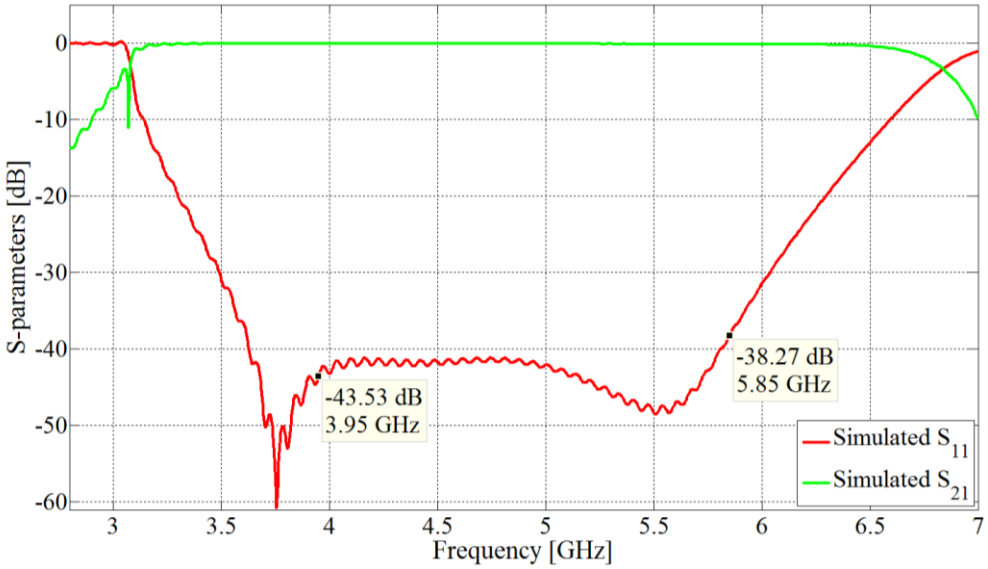

Figure 4.11. Simulated S-parameters for microstrip adapter with cut-out, matching section and tuning post optimised for wide band operation.

The addition of a post into the feed geometry is strictly not necessary as the microstrip adapter already has satisfactory results and is superior to the coaxial adapter. However the

huge advantage shown in figure 4.11 of adding a tuning post outweighs the additional complexity having the addition of a post. The maximum reflection coefficient is -38.3 dB and the insertion loss is a maximum of 0.2 dB over the band of interest. Note that the transition is useful well below the H-band edge at 3.95 GHz. A parametric study will be performed in the following subsection on this final microstrip geometry.

4.3 PARAMETRIC STUDY

The purpose of the parametric study is to determine which parameters (physical dimensions and material properties) affect the real or imaginary parts of the impedance and the insertion and return losses and therefore influencing the achievable bandwidth.

4.3.1 Microstrip substrate

The figure below gives the characteristic impedance of various microstrip strip widths on the different standard Rogers RO4003C substrate thickness.

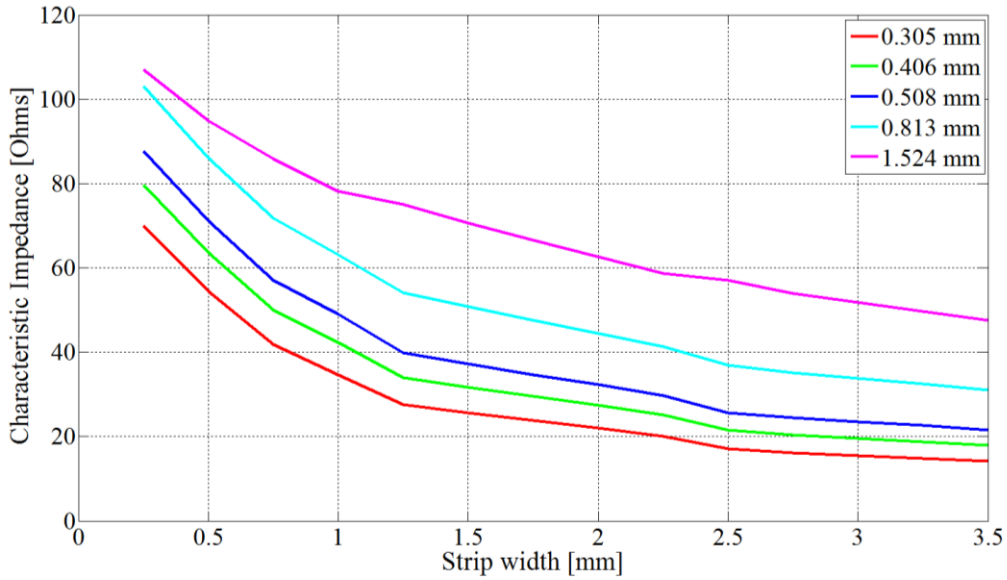

Figure 4.12. Microstrip characteristic impedance vs. the strip width for various standard substrate thicknesses.

Note that a thicker microstrip strip width has a lower characteristic impedance, and a thinner substrate thickness also leads to a lower characteristic impedance. A substrate thickness of 0.813 mm was selected for the prototype as it offered reasonable microstrip widths and was easily available.

4.3.2 Transmission line width

The width of the 50 Ω section of the microstrip transmission line is defined below in figure 4.13. The nominal width is 1.78 mm, which yields 50 Ω on the given 0.813 mm substrate thickness in figure 4.12.

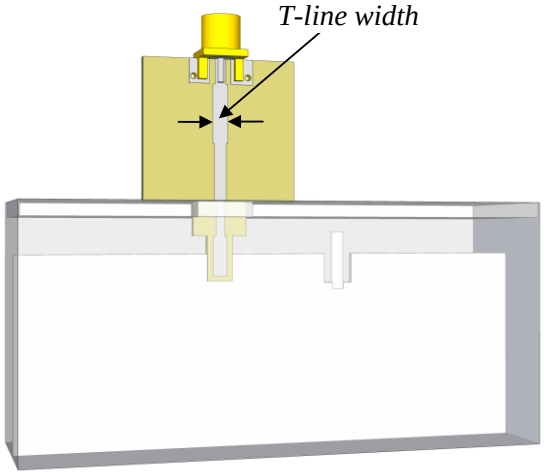

Figure 4.13. Microstrip transmission line width.

The input impedance of the prototype transition for various transmission line widths is given in figure 4.14.

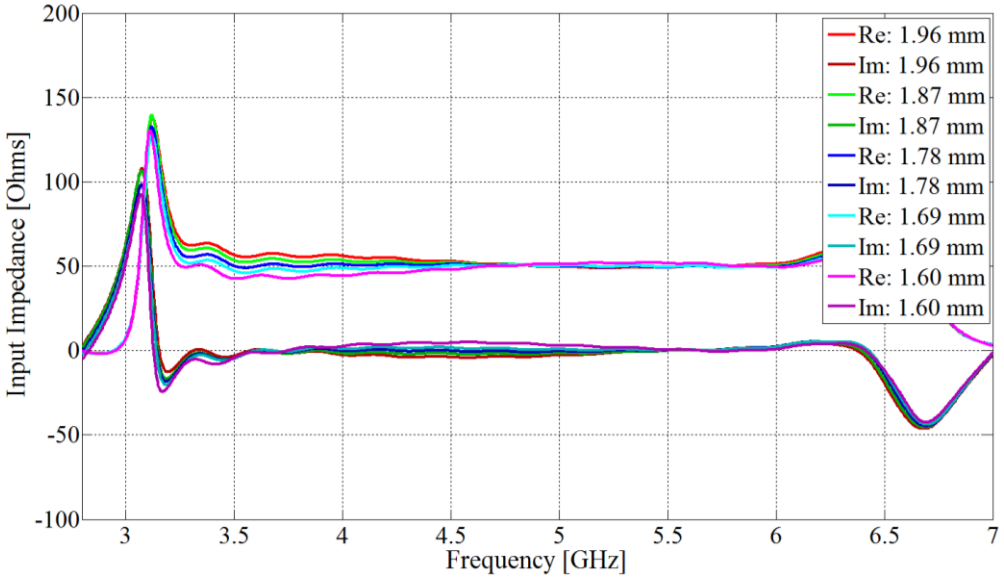

Figure 4.14. Complex input impedance for different transmission line widths.

Note that the scale of the input impedance in the figure above is larger than in the figures related to the prototype end-launched adapter, to show the effect of the probe's resonance.

Note that the input impedance appears to vary more at the lower end of the band for variations in transmission line widths. The reflection coefficient for the different microstrip transmission line widths is given in figure 4.15.

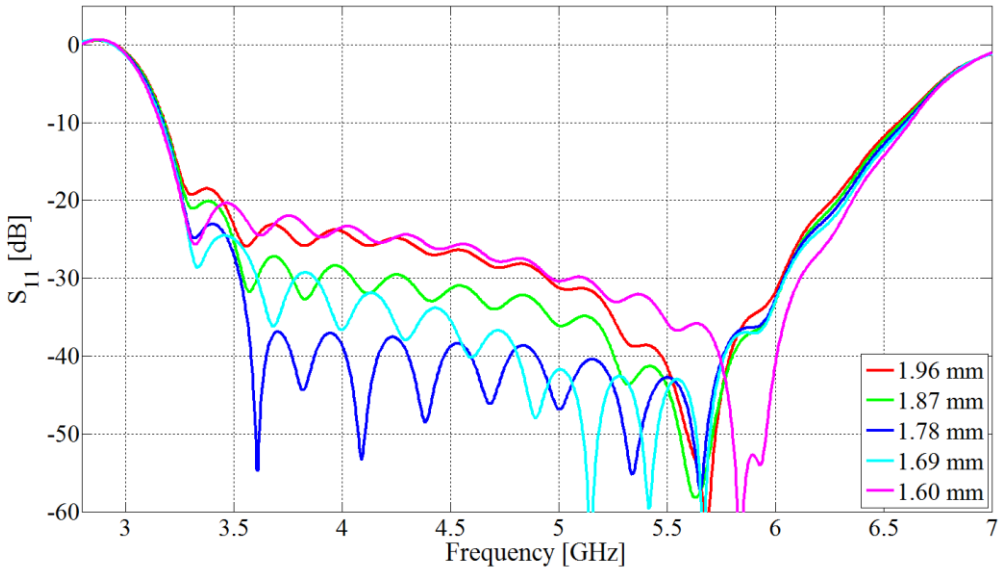

Figure 4.15. Simulated reflection coefficient for different transmission line widths.

The simulated insertion losses for the various microstrip widths are given below in figure 4.16. From the simulated insertion loss and reflection coefficient it can be seen that the parameter is moderately sensitive.

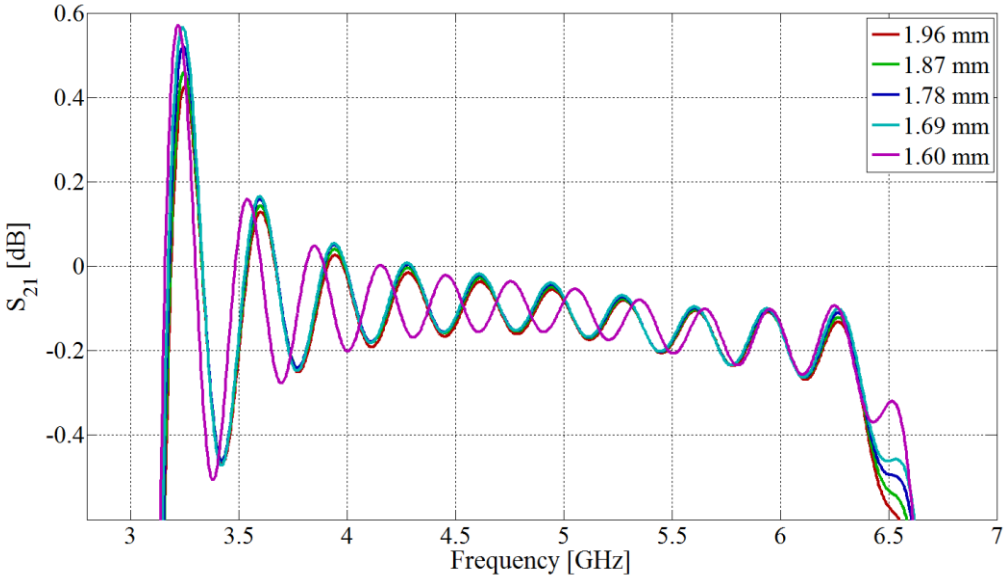

Figure 4.16. Simulated transmission coefficient for different transmission line widths.

4.3.3 Matching length

As discussed in section 4.2.4, a matching section of microstrip is incorporated between the outside of the waveguide's side wall and the 50 Ω section of microstrip transmission line as shown in figure 4.17.

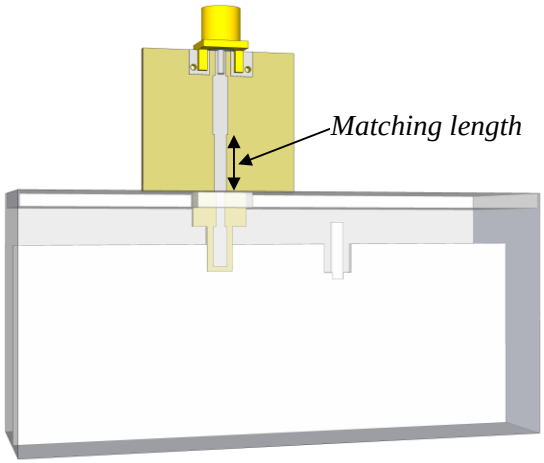

Figure 4.17. Matching length dimension definition.

The simulated input impedance of the prototype transition is given below in figure 4.18.

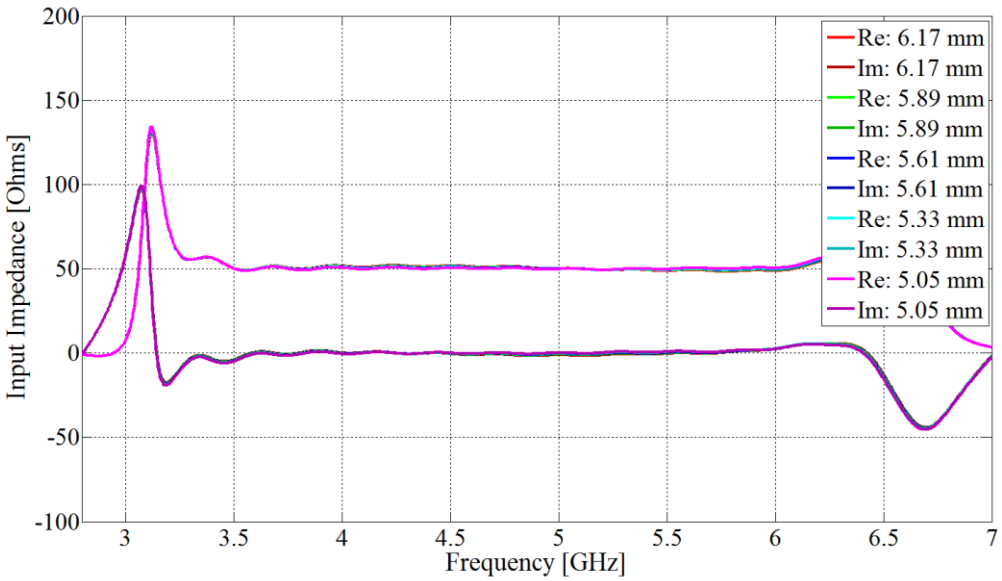

Figure 4.18. Complex input impedance for different matching section lengths.

Note that the input impedance appears to be reasonable insensitive to the matching length parameter. The reflection coefficient for various matching lengths is given in figure 4.19.

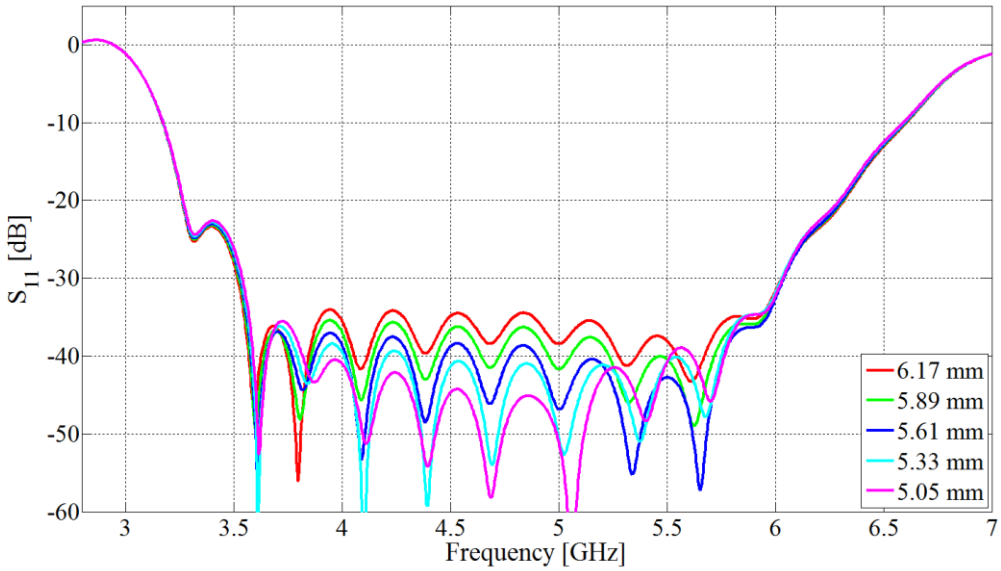

Figure 4.19. Simulated reflection coefficient for different matching section lengths.

Note that the effect of the different matching lengths simply shifts the reflection coefficient slightly up or down in the middle of the band depending on if the parameter is increased or decreased respectively. Figure 4.20 shows simulated insertion loss for the various matching section lengths.

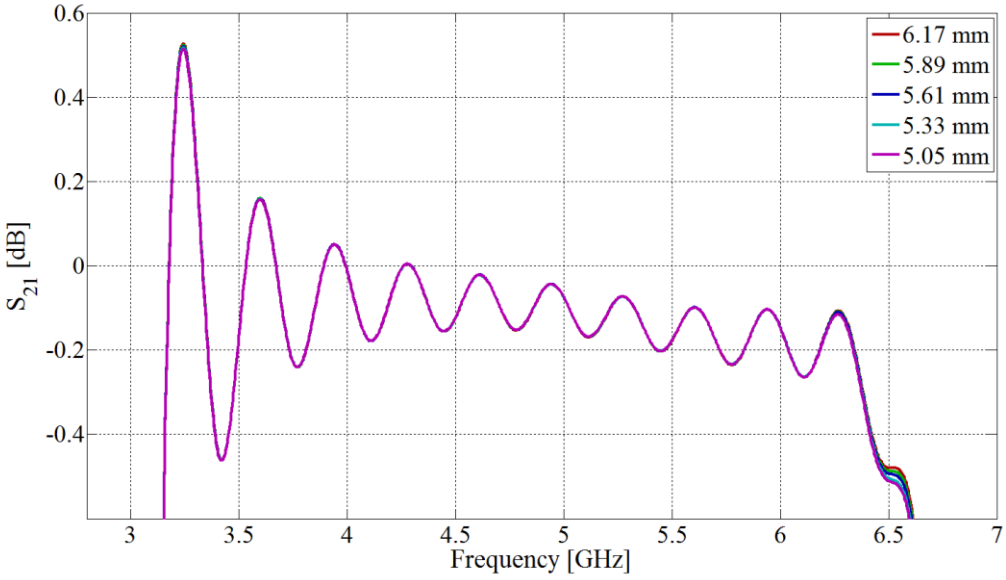

Figure 4.20. Simulated transmission coefficient for different matching section lengths.

It is interesting to note that the coaxial end-launched adapter was also fairly insensitive to the matching length parameter.

4.3.4 Matching strip width

The width of the matching microstrip section is defined figure 4.21 in below. The width of the matching section sets the characteristic impedance of the matching section.

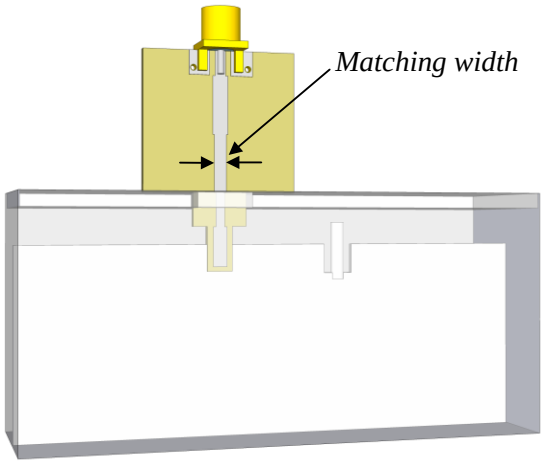

Figure 4.21. Matching strip width definition.

For all microstrip lines the constraint for the minimum strip widths was set as 0.5 mm to minimise the risk of strips lifting off of the substrate during final tuning of the prototype. The input impedance for various matching section widths is given in figure 4.22.

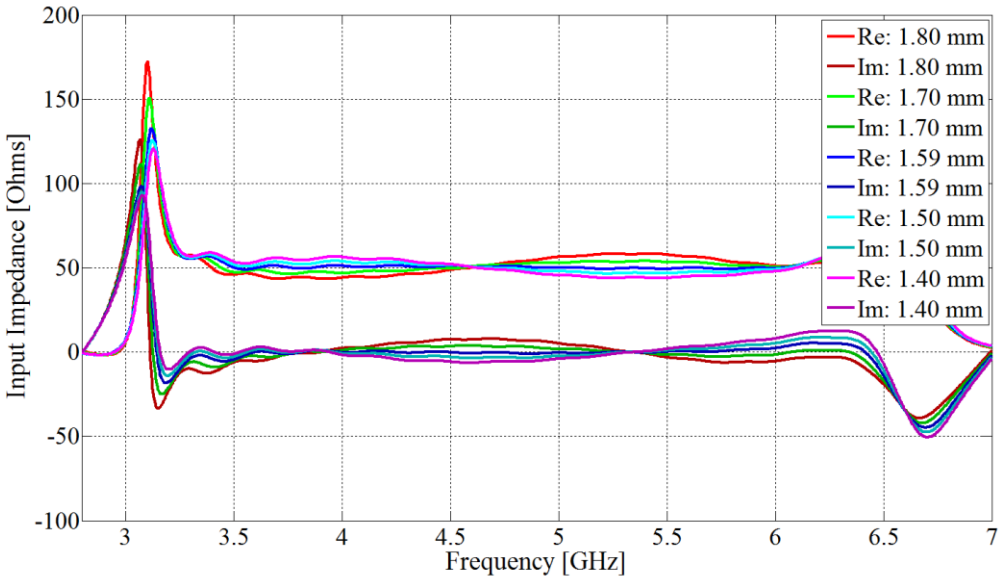

Figure 4.22. Complex input impedance for different matching section widths.

From the input impedance figure above it can be seen that the design is highly sensitive to the parameter variations.

The simulated reflection coefficient achieved with the various matching strip widths is given in figure 4.23.

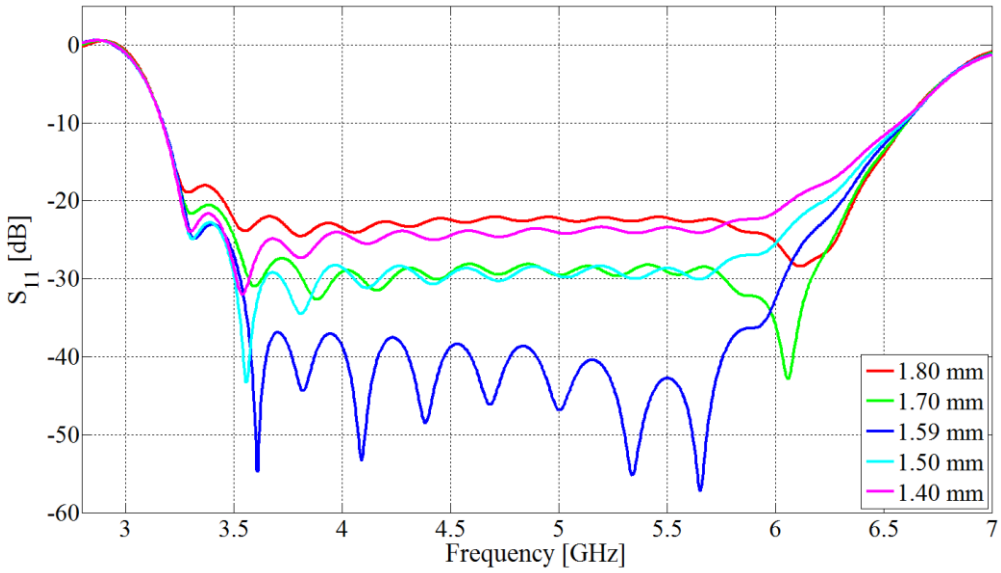

Figure 4.23. Simulated reflection coefficient for different matching section widths.

The simulated insertion losses for the various matching microstrip widths are given below in figure 4.24.

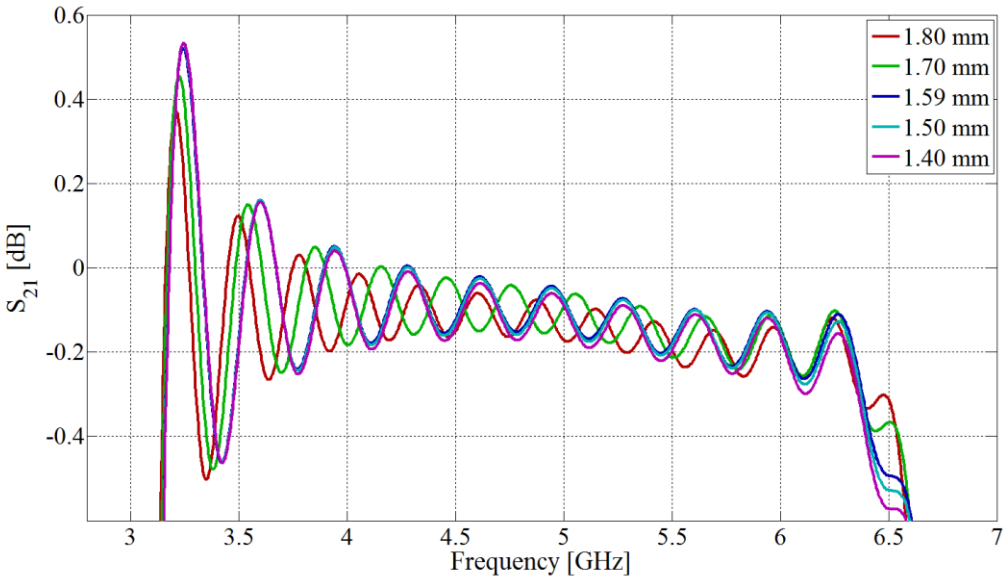

Figure 4.24. Simulated transmission coefficient for different matching section widths.

4.3.5 Feed-line microstrip width

The width of the microstrip feed-line that transfers energy through the waveguide's side wall into the inside of the waveguide is defined below in figure 4.25.

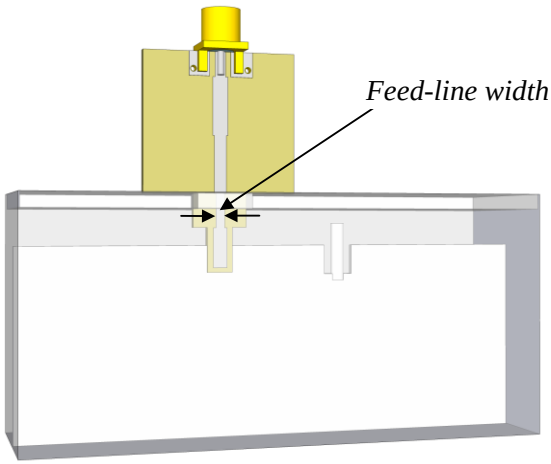

Figure 4.25. Feed-line width dimension definition.

Figure 4.26 gives the input impedance for various feed-line microstrip strip widths.

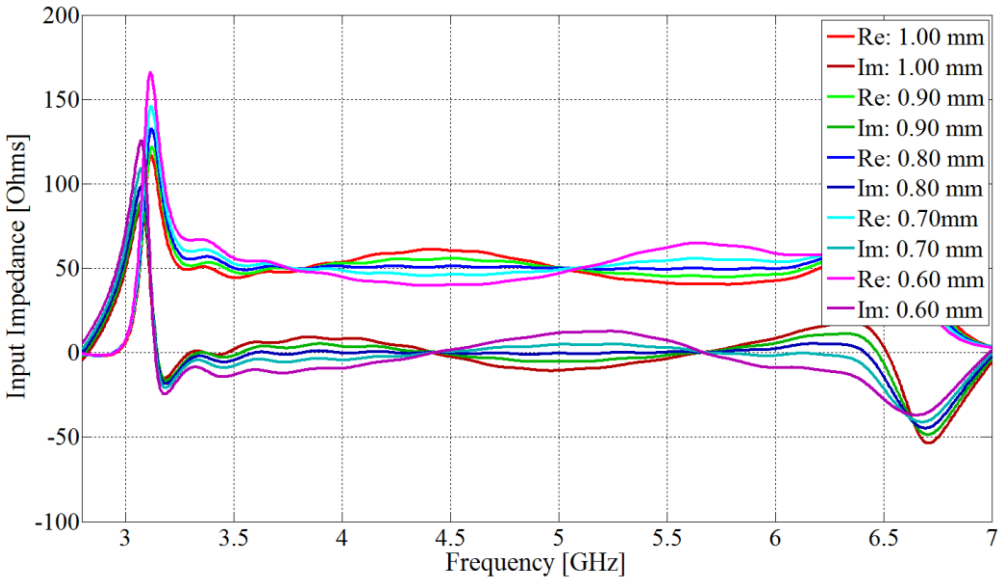

Figure 4.26. Complex input impedance for different feed-line widths.

The figure above shows that the prototype is quite sensitive to parameter variations. The reflection coefficient for the various feed-line widths are given in figure 4.27.

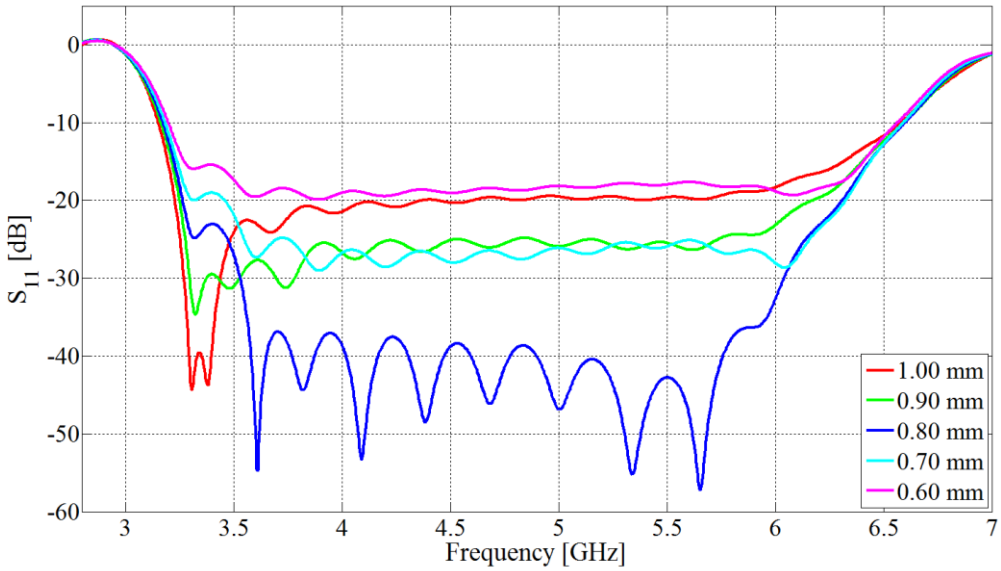

Figure 4.27. Simulated reflection coefficient for different feed-line widths.

The simulated insertion loss for the different microstrip feed-line widths are given below in figure 4.28.

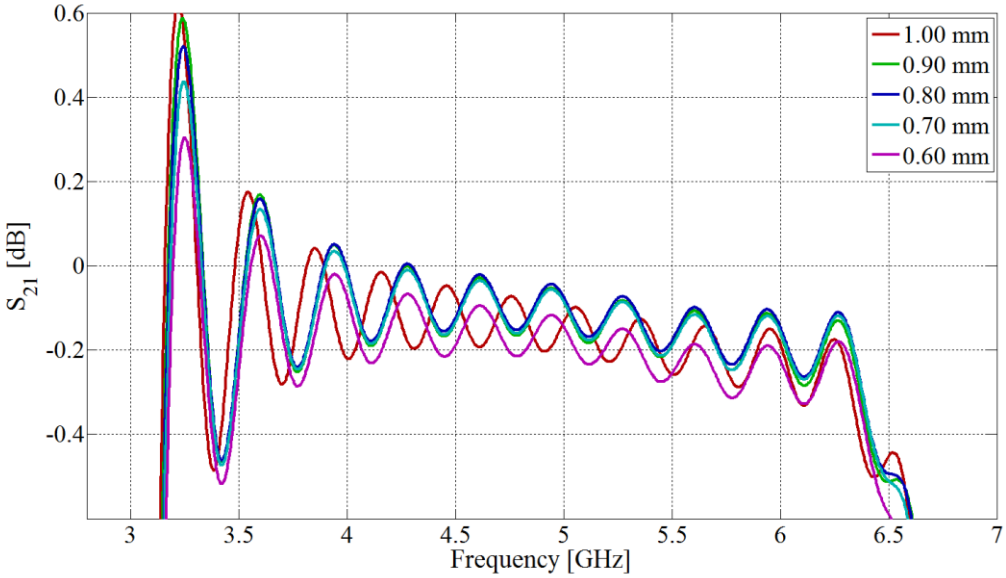

Figure 4.28. Simulated transmission coefficient for different feed-line widths.

From the simulated graphs above it can be seen that the microstrip adapter's S-parameters are most sensitive to changes in the feed-line width parameter.

4.3.6 Feed-line gap width

The feed-line gap width is the width of the microstrip substrate and air gap above the substrate that forms the hole in the waveguide's side wall that the feed structure passes through, as shown in figure 4.29.

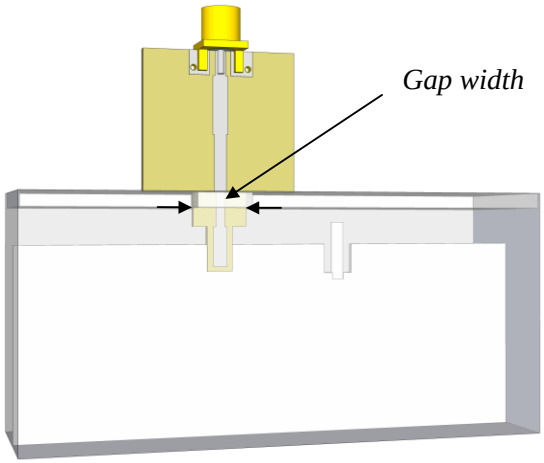

Figure 4.29. Feed-line gap width dimension.

Figure 4.30 gives the simulated input impedance for various gap widths, note that the impedance appears to be quite insensitive to parameter variations.

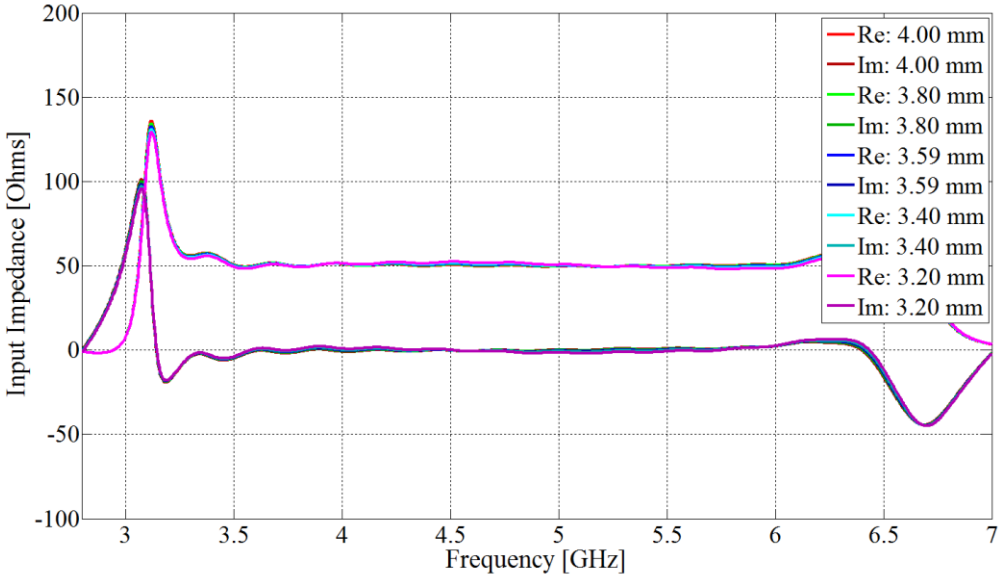

Figure 4.30. Complex input impedance for different feed-line gap widths.

The reflection coefficient for the various gap widths is given in figure 4.31.

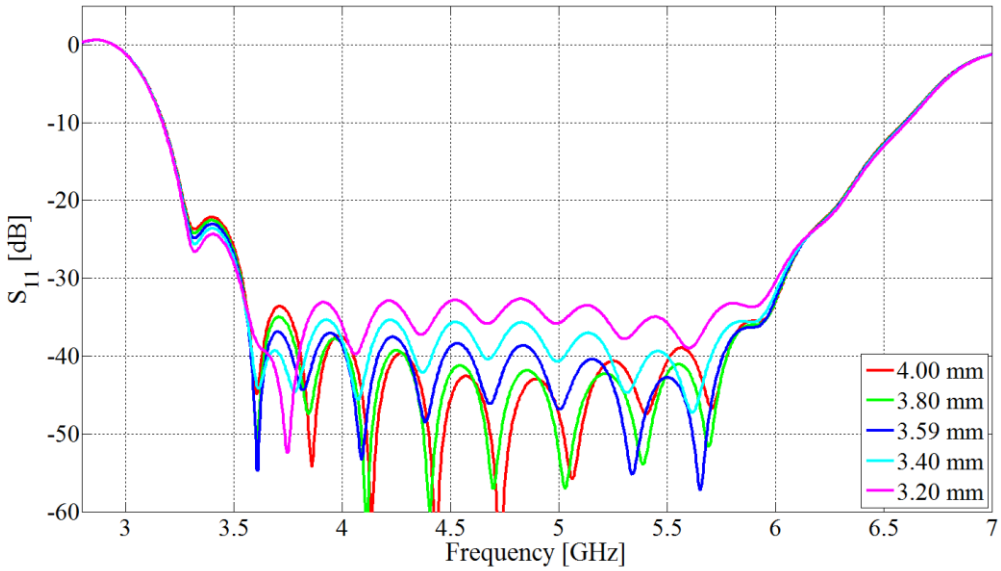

Figure 4.31. Simulated reflection coefficient for different feed-line gap widths.

Figure 4.32 shows the effect of the different feed-line gap widths on the simulated insertion loss.

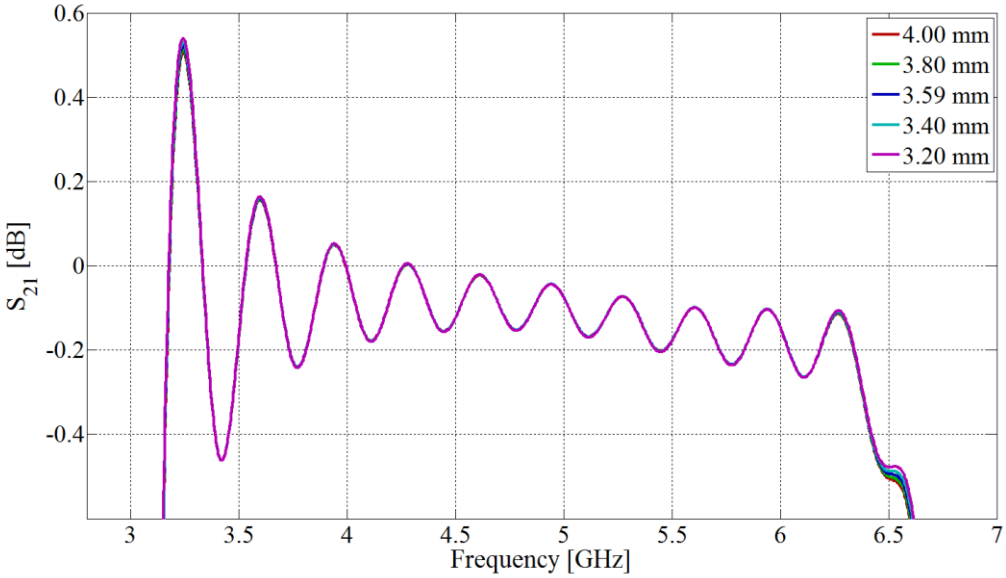

Figure 4.32. Simulated transmission coefficient for different feed-line gap widths.

Note that hardly any variation is visible in the insertion loss for the given parameter values.

4.3.7 Microstrip air gap (waveguide hole)

The feed-line gap width previously defined described the width of the hole in the waveguide's side wall through which the microstrip feed-line passes. The height above the microstrip substrate that forms the height of the air gap in the side wall hole is defined as the microstrip air gap in figure 4.33 below.

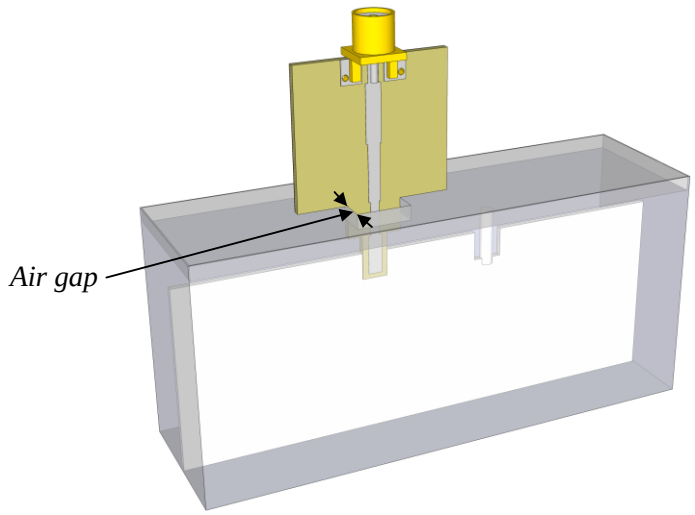

Figure 4.33. Waveguide to microstrip air gap dimension.

The simulated input impedance for various air gap heights is given below in figure 4.34.

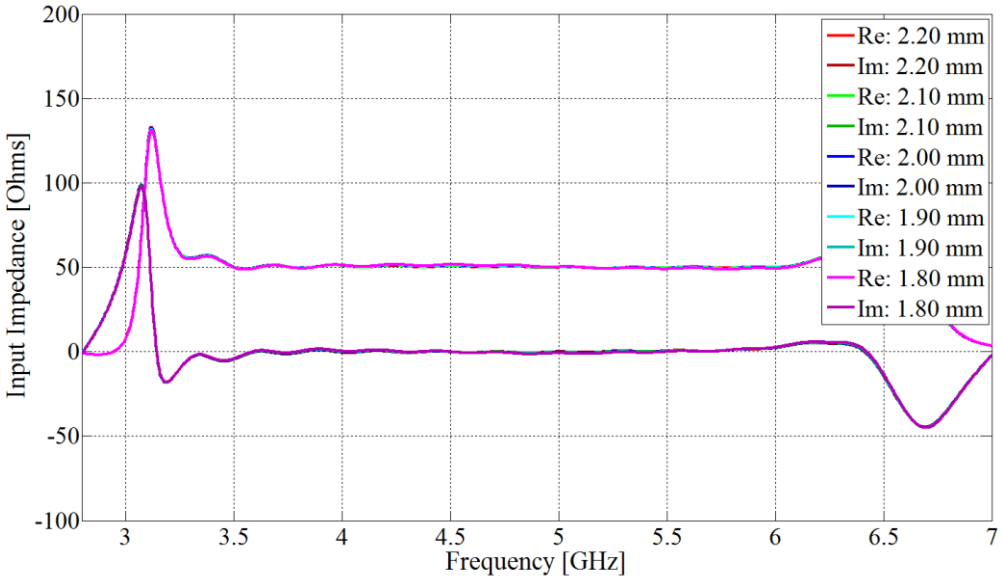

Figure 4.34. Complex input impedance for different microstrip air gap heights.

The reflection coefficient for the various air gap heights is given in figure 4.35.

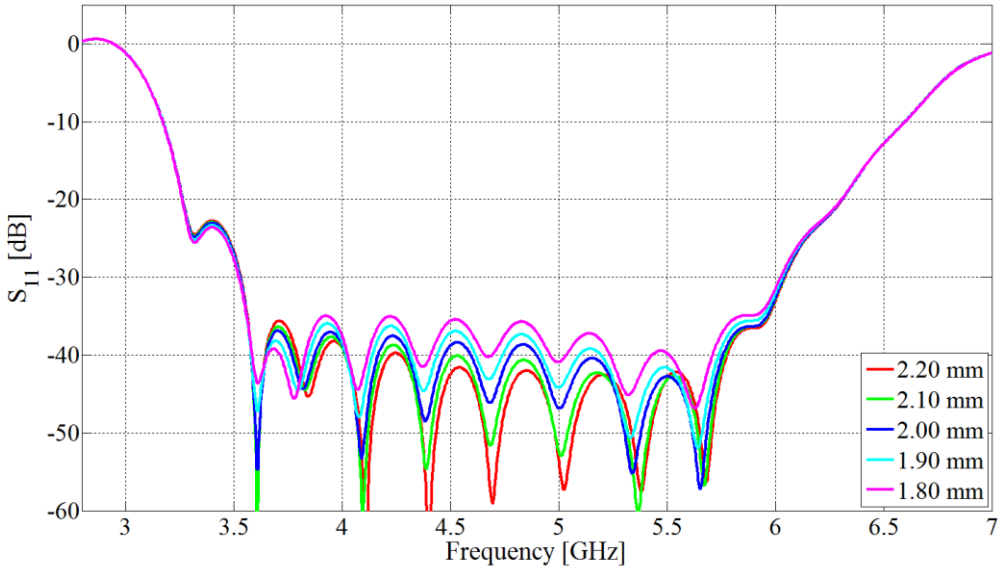

Figure 4.35. Simulated reflection coefficient for different microstrip air gap heights.

Figure 4.36 shows the effect of the different air gap heights on the simulated insertion loss.

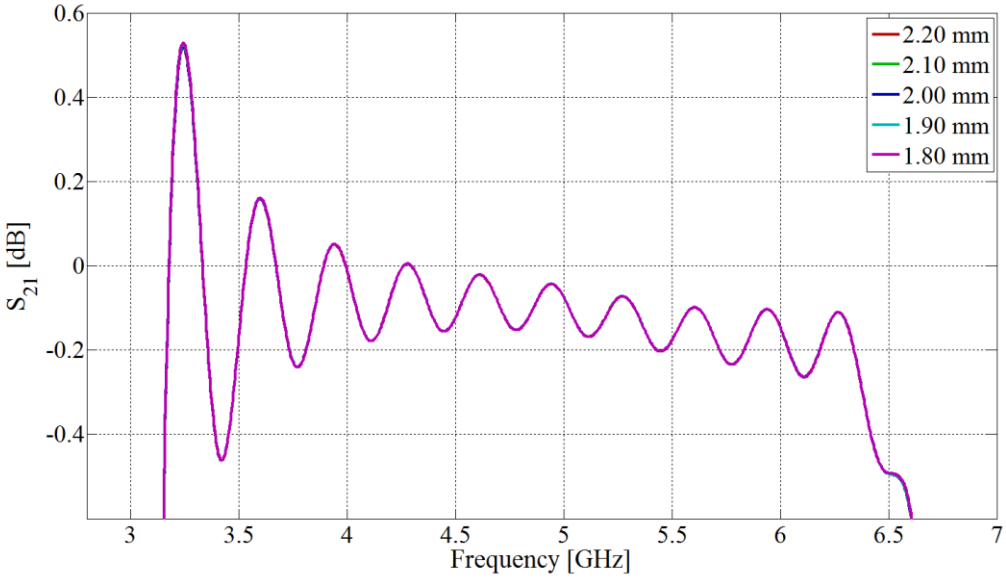

Figure 4.36. Simulated transmission coefficient for different microstrip air gap heights.

Note that the design appears to be highly insensitive to variations in the air gap height parameter.

4.3.8 Feed-line end

The feed-line end position is defined as the length that the feed-line protrudes inside the partial H-plane waveguide, as shown in figure 4.37. Note that the length is measured from the inside side wall of the waveguide and does not include the width of the side wall.

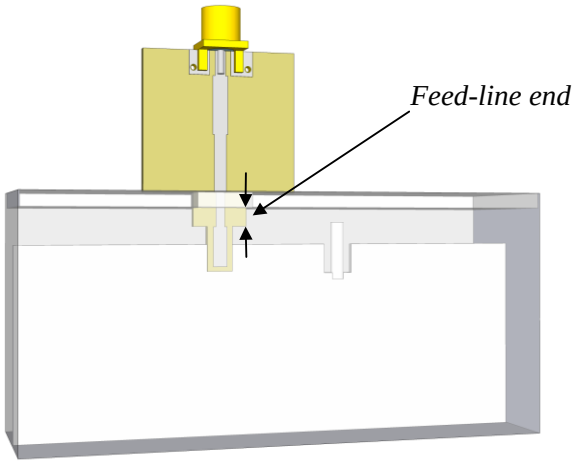

Figure 4.37. Feed-line end position definition.

Figure 4.38 below gives the input impedance for different feed-line end positions, note that the impedance appears to be quite insensitive to the parameter in that the amplitude fluctuation is minimal. However there appears to be a phase shift between the different parameter values.

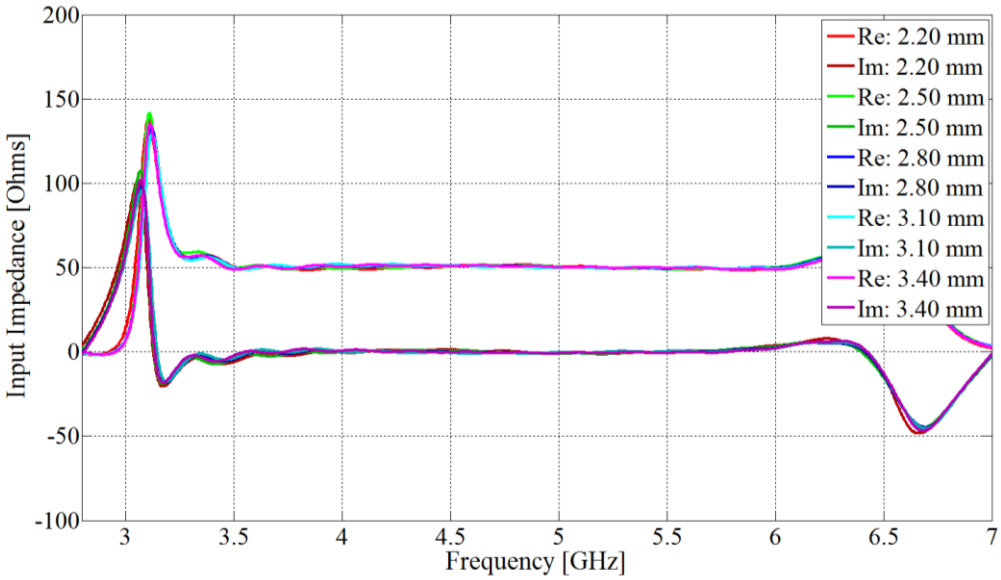

Figure 4.38. Complex input impedance for different feed-line end positions.

The reflection coefficient for the various feed-line end positions is given in figure 4.39.

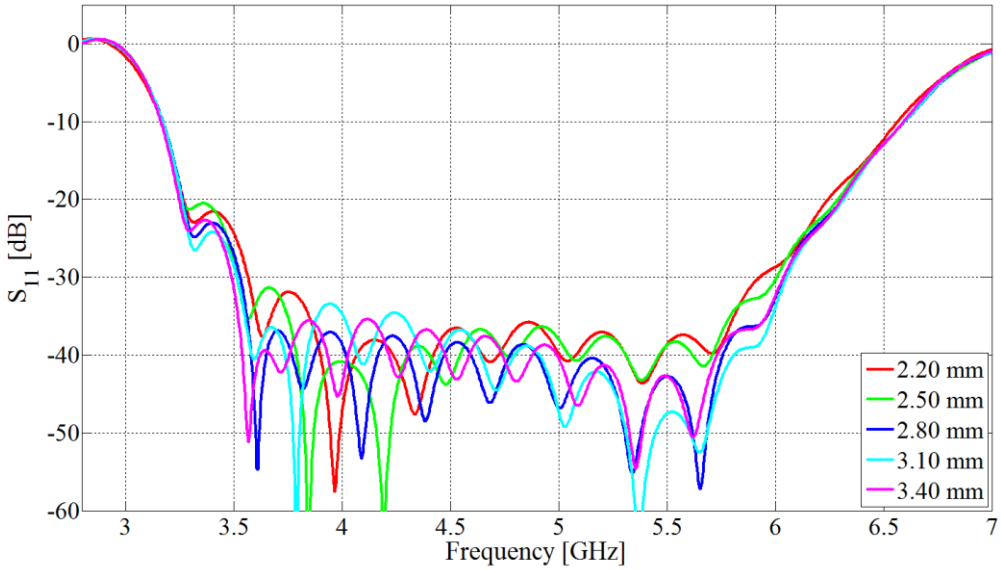

Figure 4.39. Simulated reflection coefficient for different feed-line end positions.

The simulated insertion loss for the various feed-line end positions is given in figure 4.40.

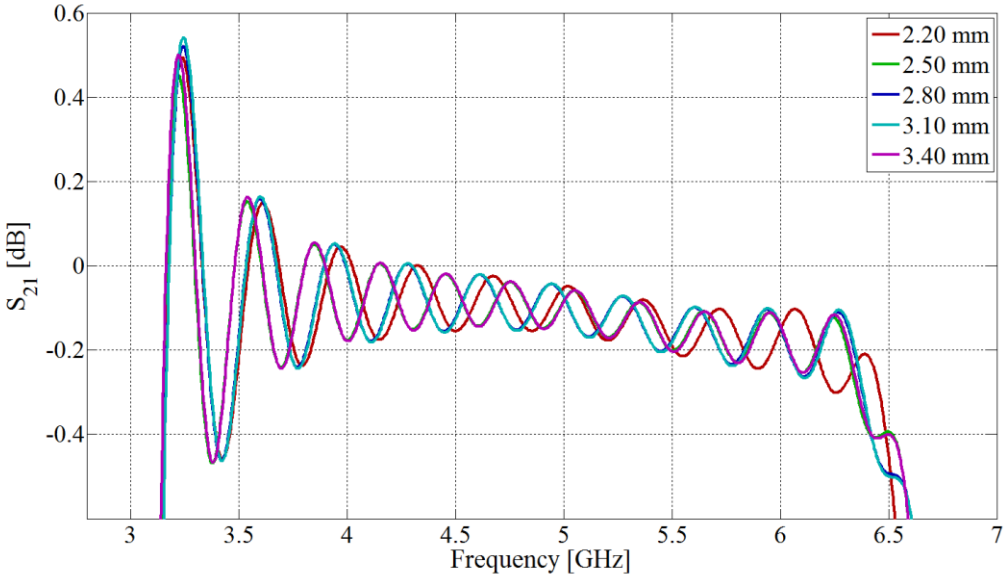

Figure 4.40. Simulated transmission coefficient for different feed-line end positions.

4.3.9 Probe position

The probe position is defined as the distance between the centre of the probe to the shorting wall as shown in figure 4.41.

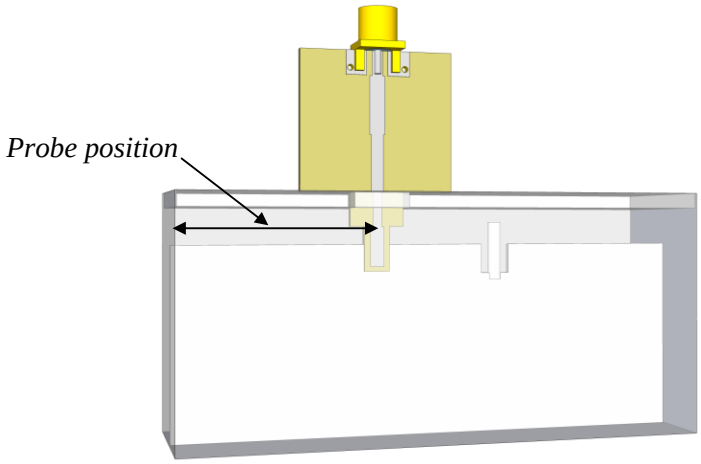

Figure 4.41. Probe position dimension definition.

The input impedance for the various probe positions is given below in figure 4.42.

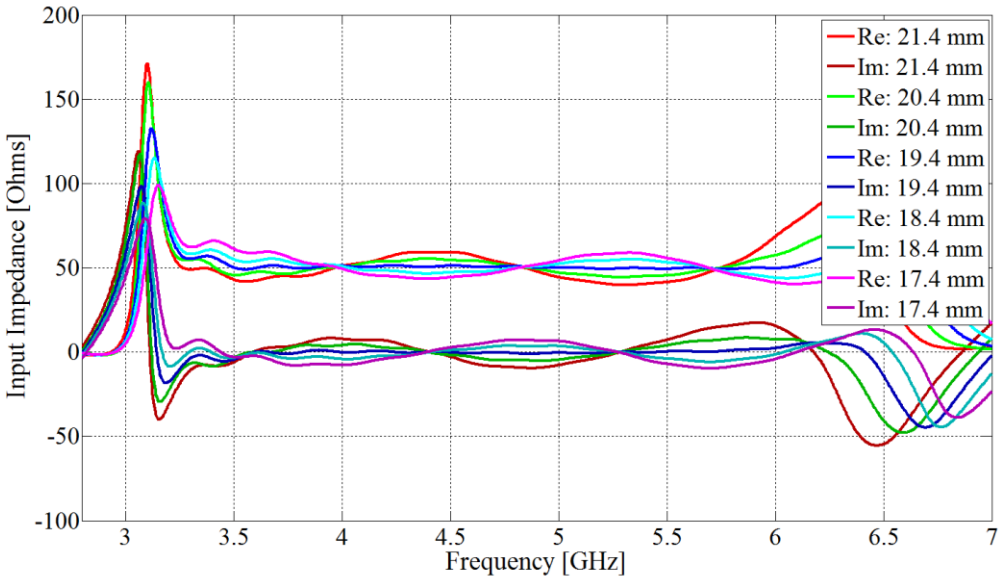

Figure 4.42. Complex input impedance for different probe positions.

Note that the figure above shows that the impedance is highly sensitive to variations in the probe position parameter. This result was expected as the probe position sets the resonant frequency of the probe inside the waveguide. Note that the lower frequency resonance in the figure is severely affected by the parameter variations.

The simulated reflection coefficient achieved with the various probe positions is given in figure 4.43 below.

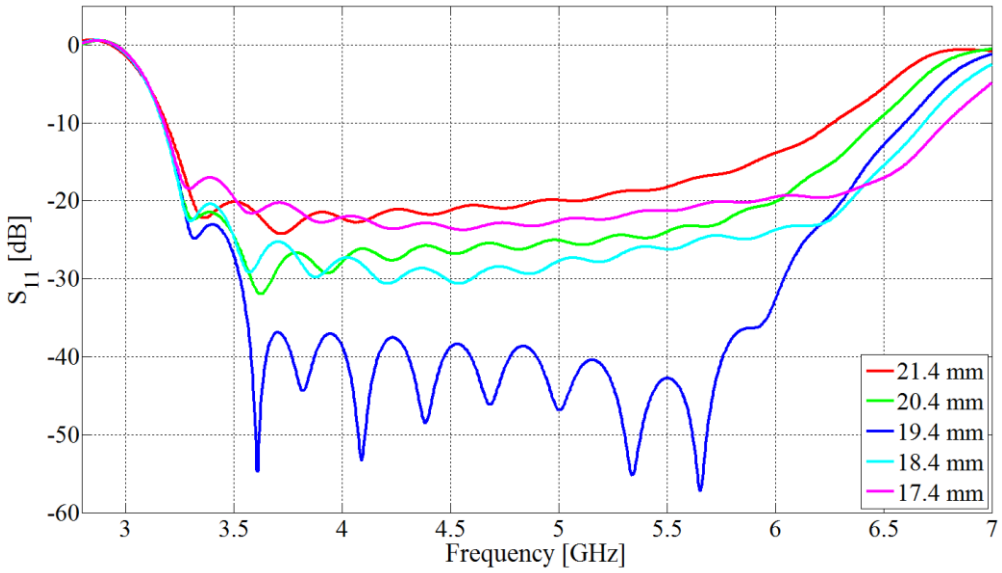

Figure 4.43. Simulated reflection coefficient for different probe positions.

The simulated insertion loss for the various probe positions are given below in figure 4.44.

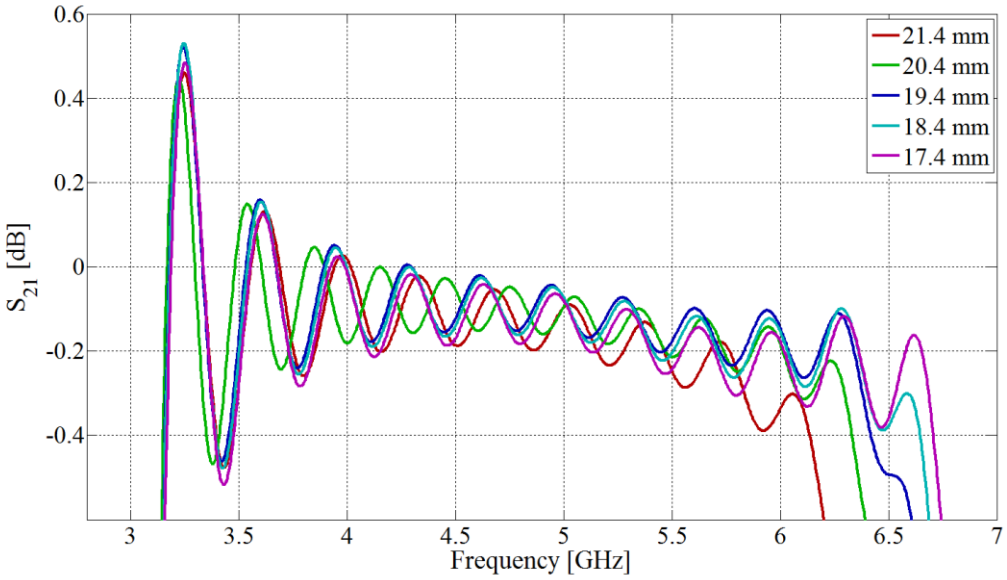

Figure 4.44. Simulated transmission coefficient for different probe positions.

Note that the insertion loss at the higher frequencies appears to be more sensitive to parameter changes then the lower frequencies.

4.3.10 Probe cut-out depth

The probe cut-out depth is defined the as the depth that the probe extends into the vane inside of the cut-out, as shown in figure 4.45.

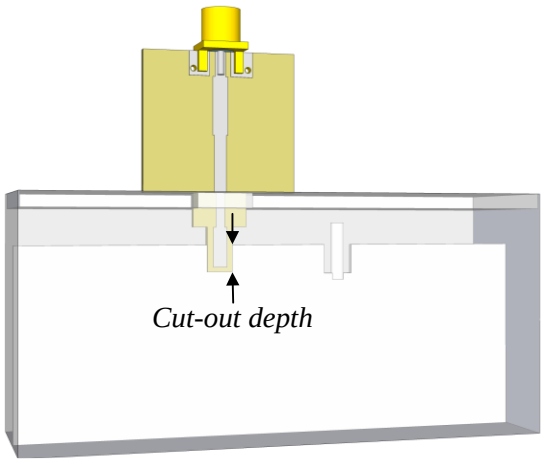

Figure 4.45. Probe cut-out depth dimension definition.

The input impedance of the prototype transition for various probe cut-out depths is given in figure 4.46.

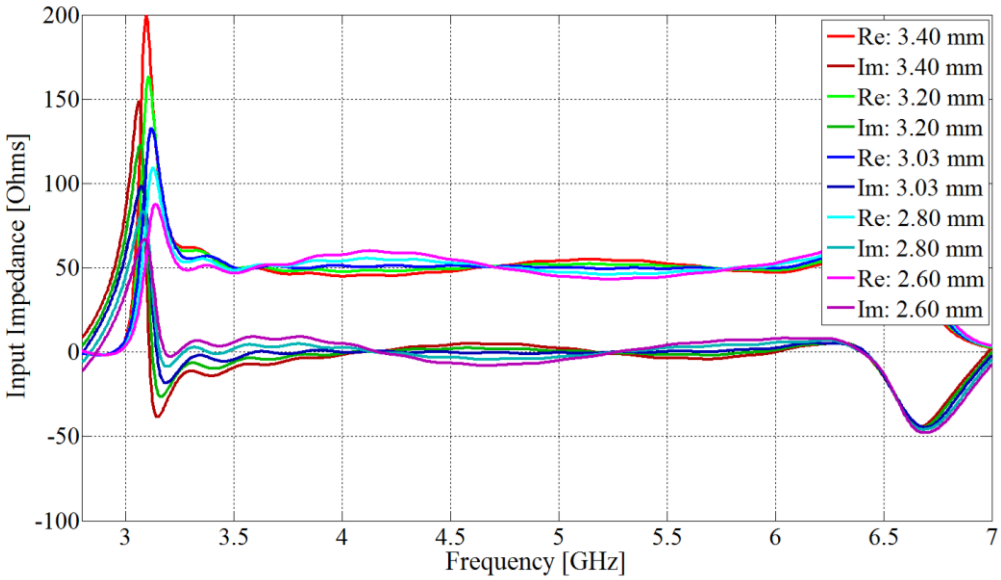

Figure 4.46. Complex input impedance for different probe cut-out depths.

From the figure above it appears that the input impedance is highly sensitive to variations in the probe cut-out depth parameter. The reflection coefficient for the various depths is given in figure 4.47.

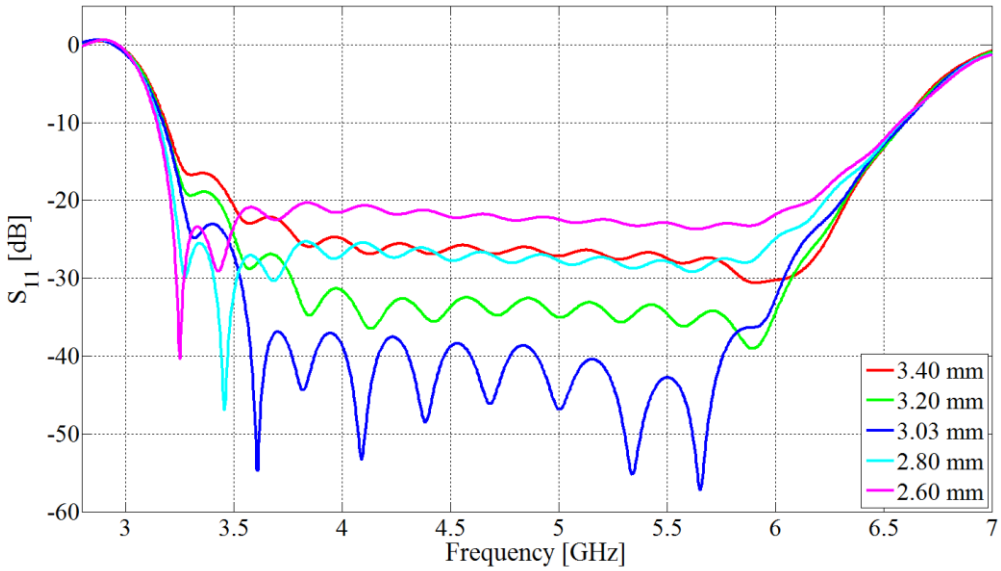

Figure 4.47. Simulated reflection coefficient for different probe cut-out depths.

Figure 4.48 shows the effect of different probe cut-out depths on the simulated insertion loss.

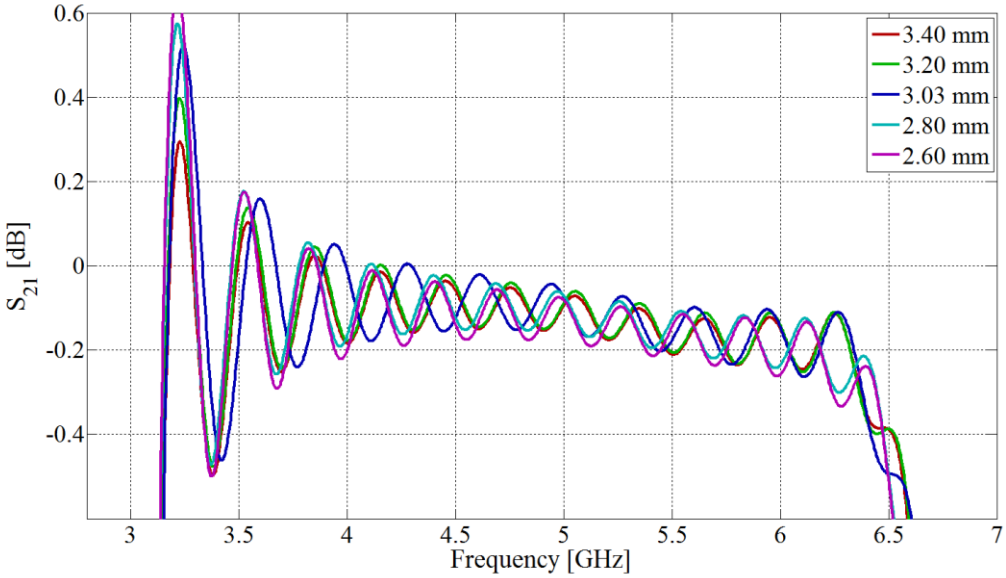

Figure 4.48. Simulated transmission coefficient for different probe cut-out depths.

It is interesting to note that the probe cut-out depth in the coaxial prototype was insensitive in contrast to the microstrip case above.

4.3.11 Probe cut-out width

The probe cut-out width is defined as the width of the cut-out around the probe as shown in figure 4.49.

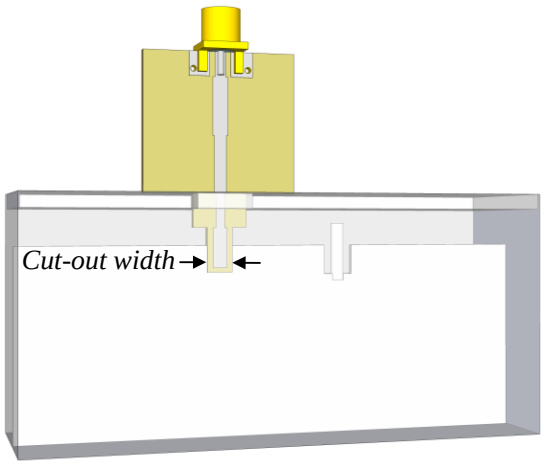

Figure 4.49. Probe cut-out width dimension definition.

The same physical constraint of 1.6 mm for the minimum acceptable cut-out width was selected as in the coaxial prototype. Figure 4.50 below gives the input impedance for different cut-out widths around the probe.

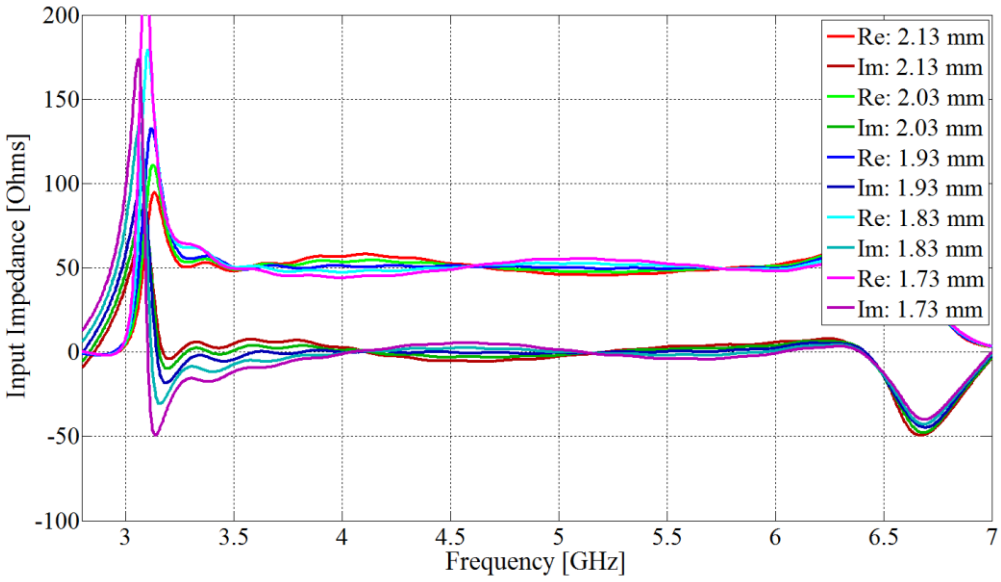

Figure 4.50. Complex input impedance for different probe cut-out widths.

The reflection coefficient for the various probe cut-out widths are given in figure 4.51.

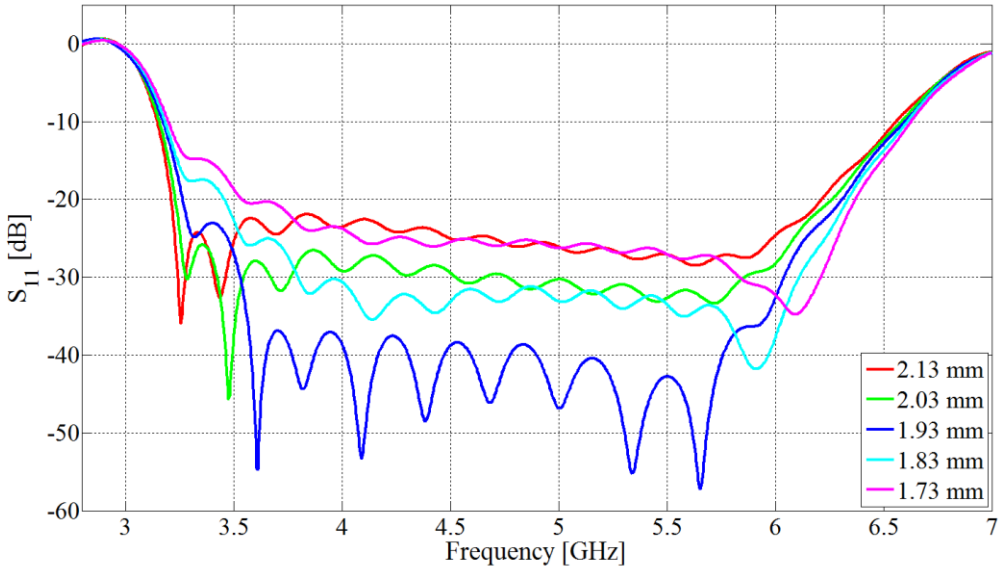

Figure 4.51. Simulated reflection coefficient for different probe cut-out widths.

From the simulated input impedance and reflection coefficient it can be seen that the design is moderately sensitive to the different values simulated. Note that the effects of parameter variations are more severe at lower frequencies. The simulated insertion losses for the various cut-out widths are given below in figure 4.52.

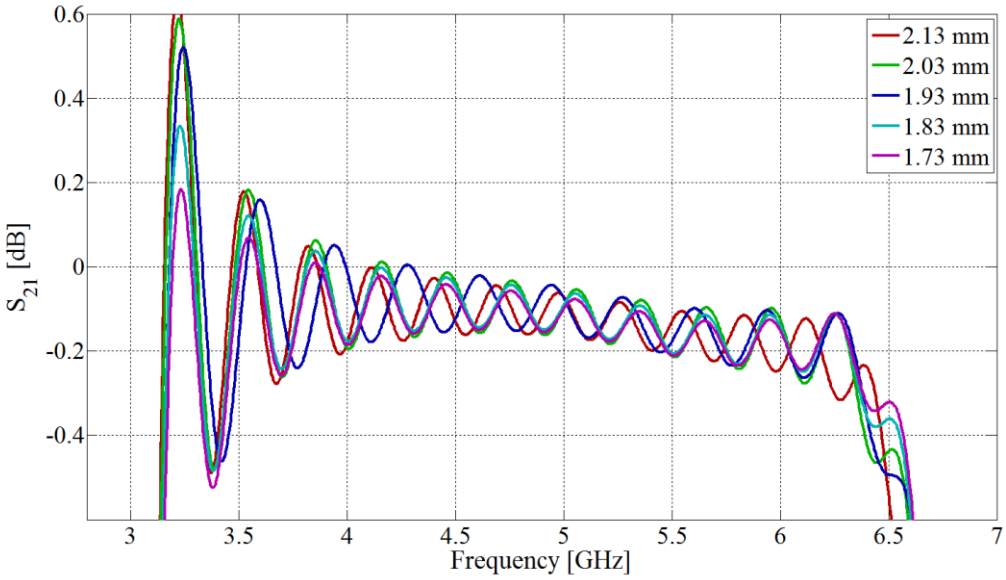

Figure 4.52. Simulated transmission coefficient for different probe cut-out widths.

4.3.12 Microstrip probe width

The probe width is defined as the width of the microstrip used to implement the probe part of the prototype transition, as shown in figure 4.53. The minimum acceptable probe width is constrained to 0.5 mm, as previously mentioned this is the constraint for all strip widths.

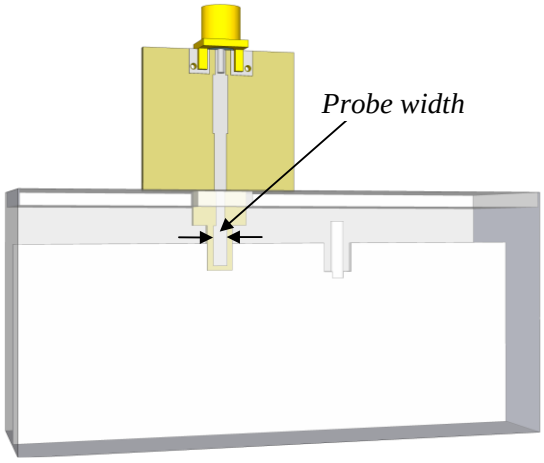

Figure 4.53. Microstrip probe width dimension.

Note that there is no ground plane on the bottom side of the substrate inside the waveguide (including the probe part). Figure 4.54 gives the simulated input impedance for various probe widths. Note that the prototype appears to be moderately sensitive to parameter variations.

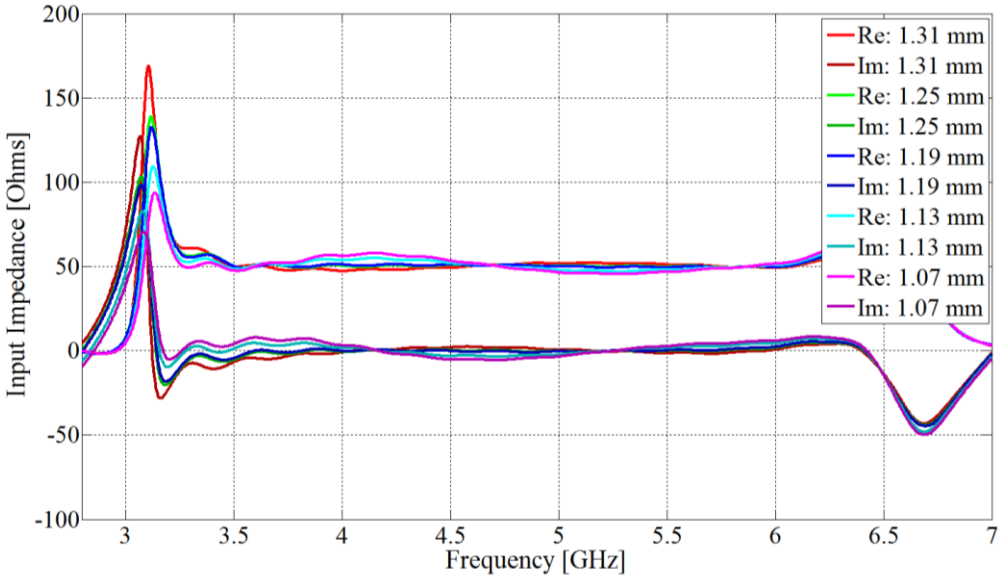

Figure 4.54. Complex input impedance for different probe widths.

Note that the variation in impedance appears to be more severe at the lower edge of the band. The reflection coefficient for the various microstrip probe widths is given in figure 4.55.

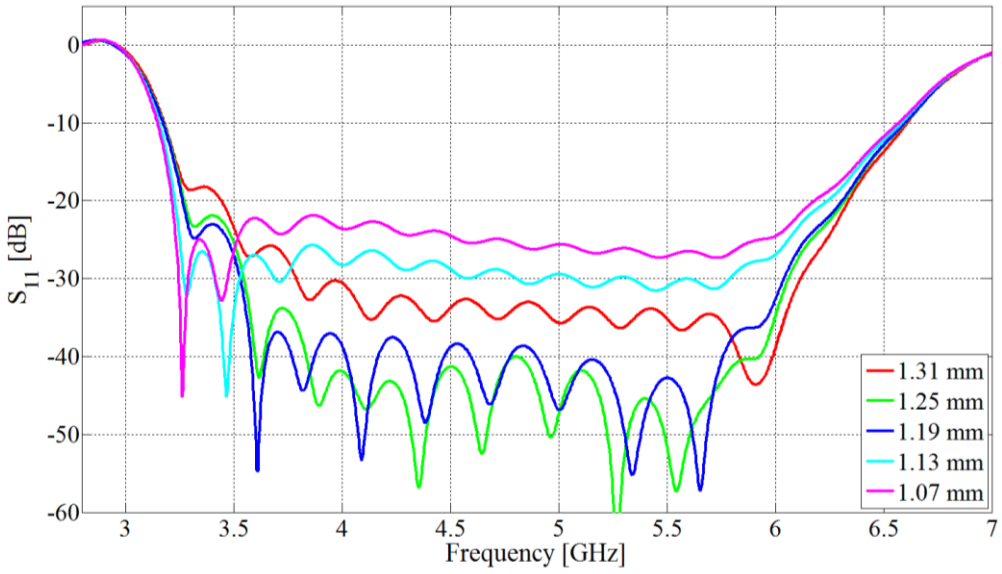

Figure 4.55. Simulated reflection coefficient for different probe widths.

The simulated insertion loss for the various probe widths are given below in figure 4.56.

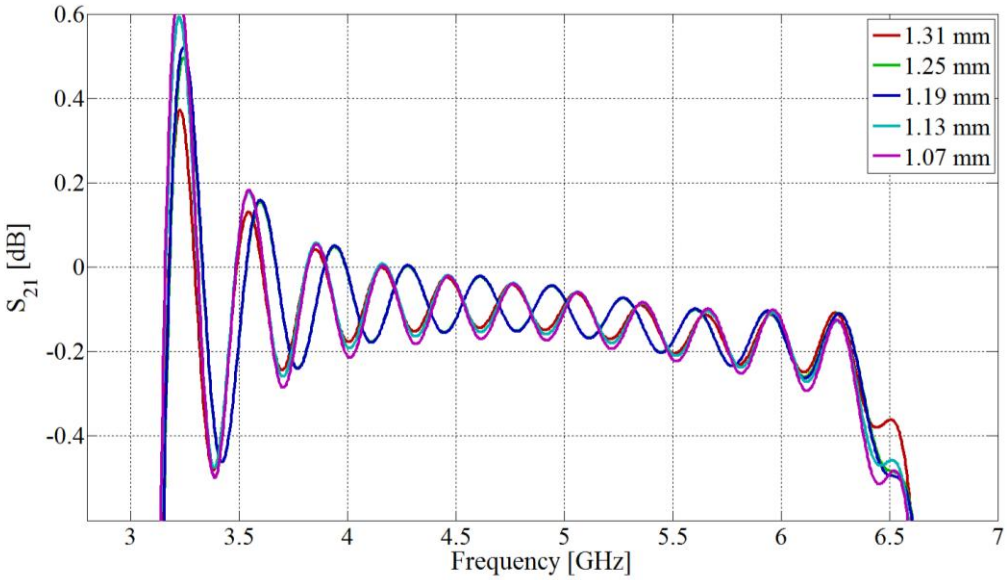

Figure 4.56. Simulated transmission coefficient for different probe widths.

Note that the probe width parameter can differ from the diameter of the post; therefore in this regard the microstrip adapter has at least one more degrees of freedom, when compared to the end-launched coaxial prototype.

4.3.13 Post position

As in the coaxial end-launcher the post position is the distance between the centre of the post to the waveguide's shorting wall as depicted in figure 4.57.

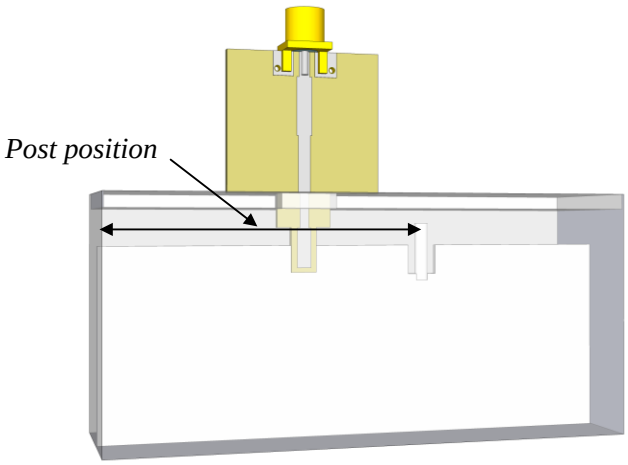

Figure 4.57. Post position dimension definition.

Figure 4.58 gives the input impedance for various post positions. Note that this parameter appears to be moderately sensitive with fluctuations in both the real and imaginary components clearly visible.

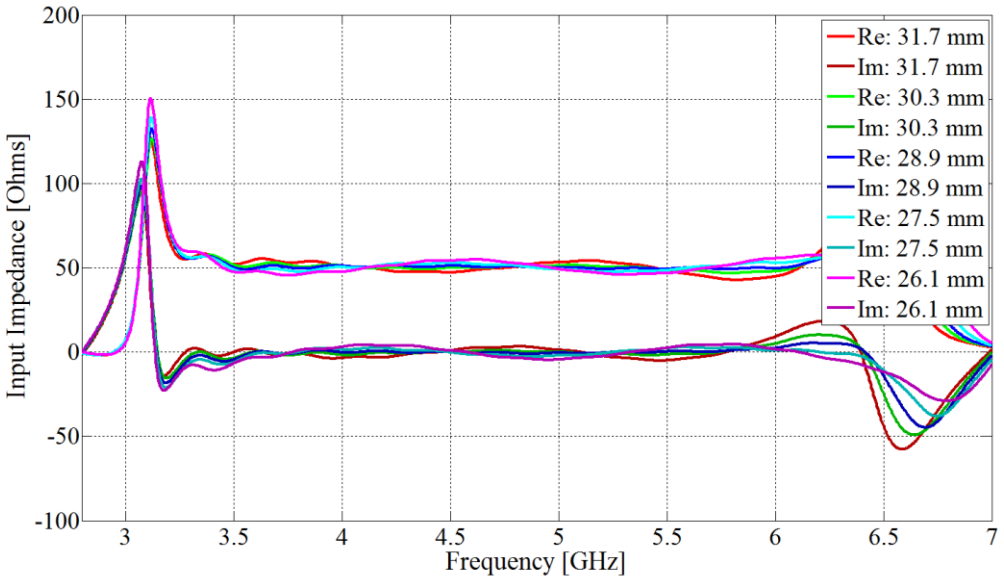

Figure 4.58. Complex input impedance for different post positions.

Since the post position sets the resonance frequency of the post it is expected to be a sensitive parameter. The reflection coefficient for the various post positions are given below in figure 4.59.

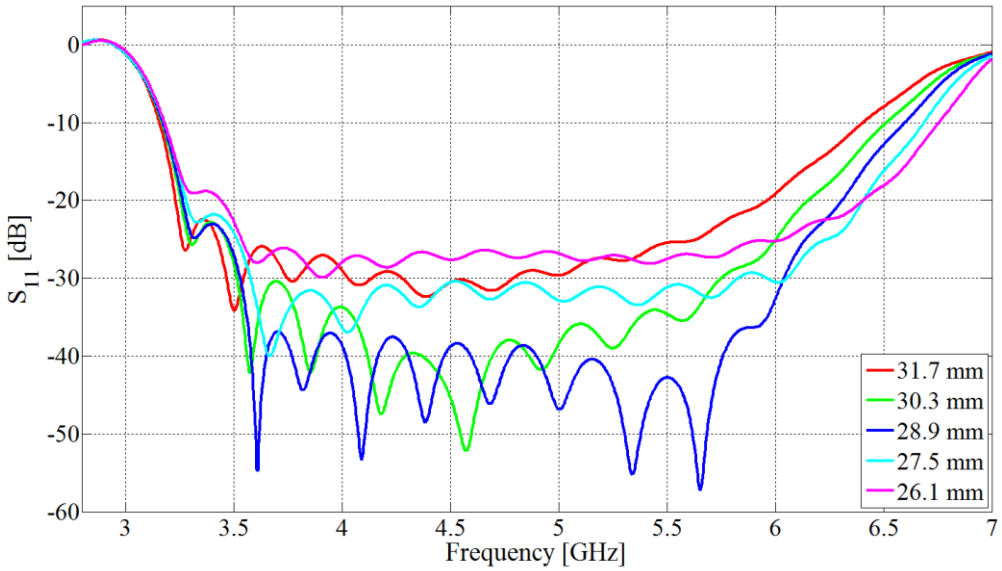

Figure 4.59. Simulated reflection efficient for different post positions.

Note that the higher frequencies in the figure above are more severely affected by the parameter variations in the post position compared to the lower frequencies. Figure 4.60 shows the effect of different post positions on the simulated insertion loss.

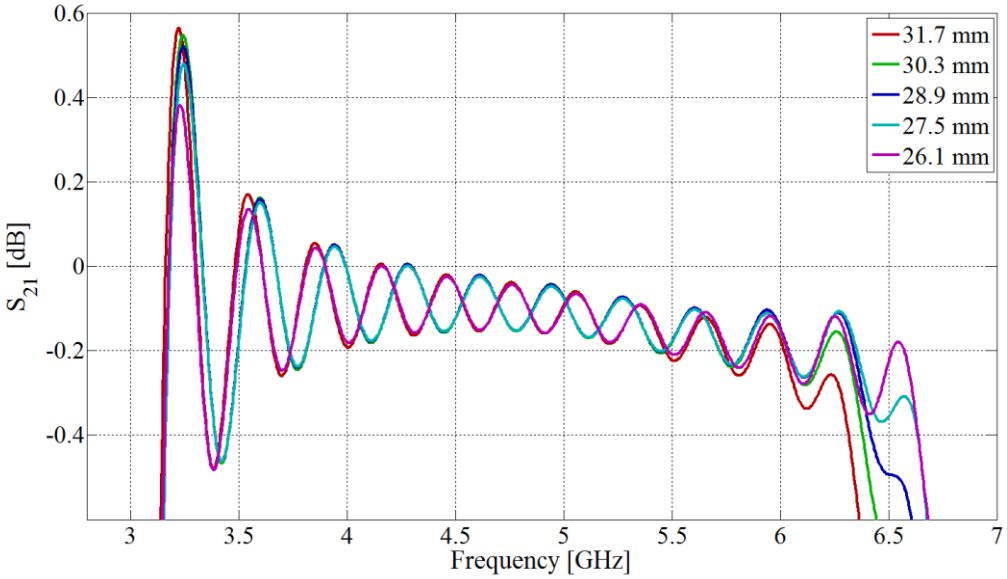

Figure 4.60. Simulated transmission efficient for different post positions.

4.3.14 Post cut-out depth

The definition of the cut-out depth for the tuning post is given below in figure 4.61. Note that the post cut-out depth sets the length of the post, as in the coaxial case.

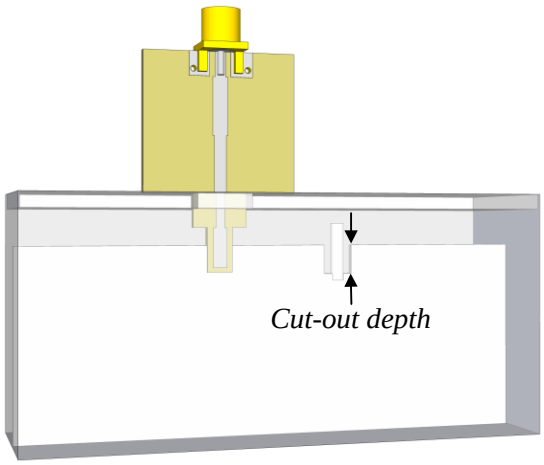

Figure 4.61. Post cut-out depth dimension definition.

Figure 4.62 below gives the input impedance for increased and decreased post cut-out depths.

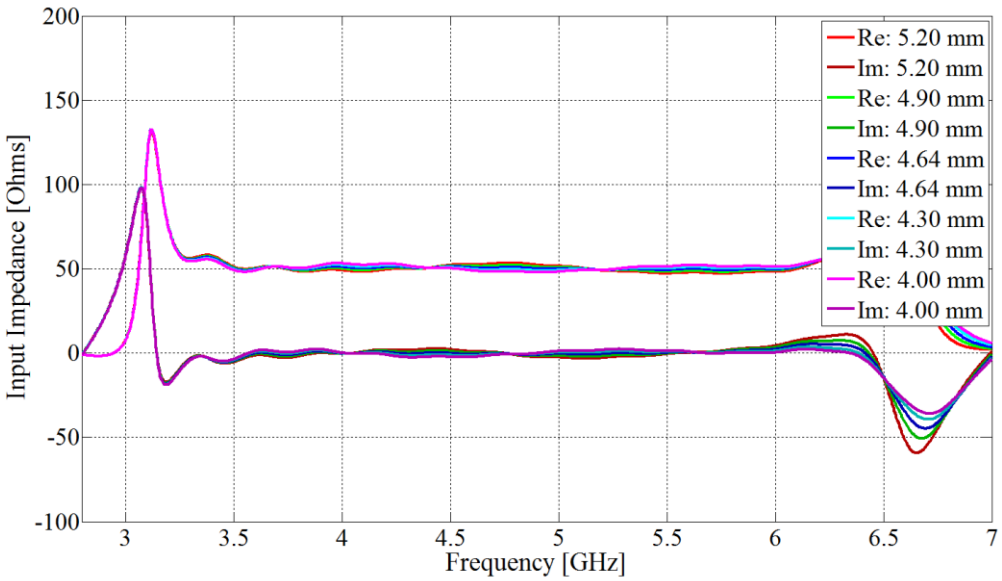

Figure 4.62. Complex input impedance for different post cut-out depths.

From the figure above it appears that the post cut-out depth is somewhat insensitive as in the coaxial end-launched adapter scenario.

The reflection coefficient for various post cut-out depths is given in figure 4.63.

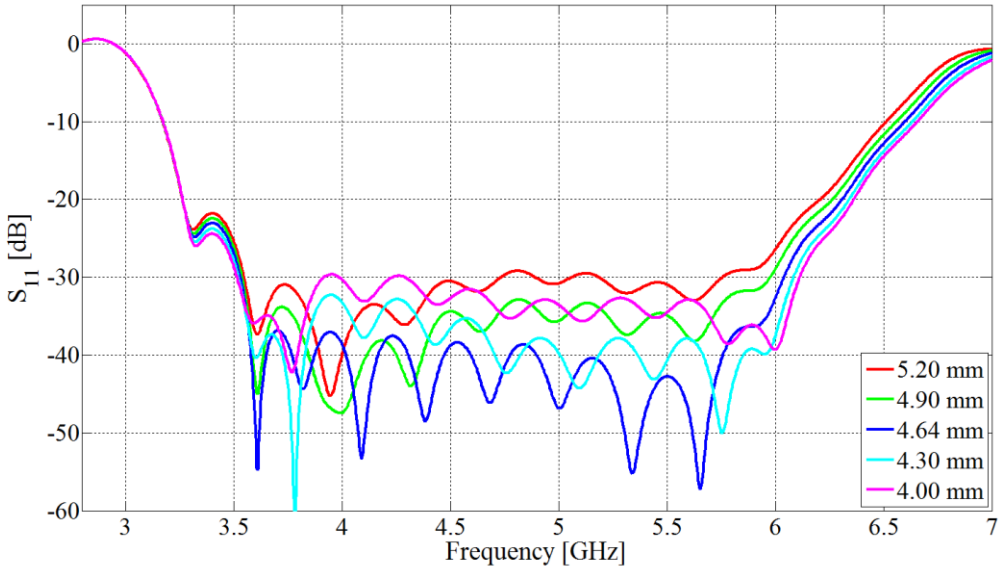

Figure 4.63. Simulated reflection coefficient for different post cut-out depths.

Figure 4.64 shows the effect of different post cut-out depths on the simulated insertion loss.

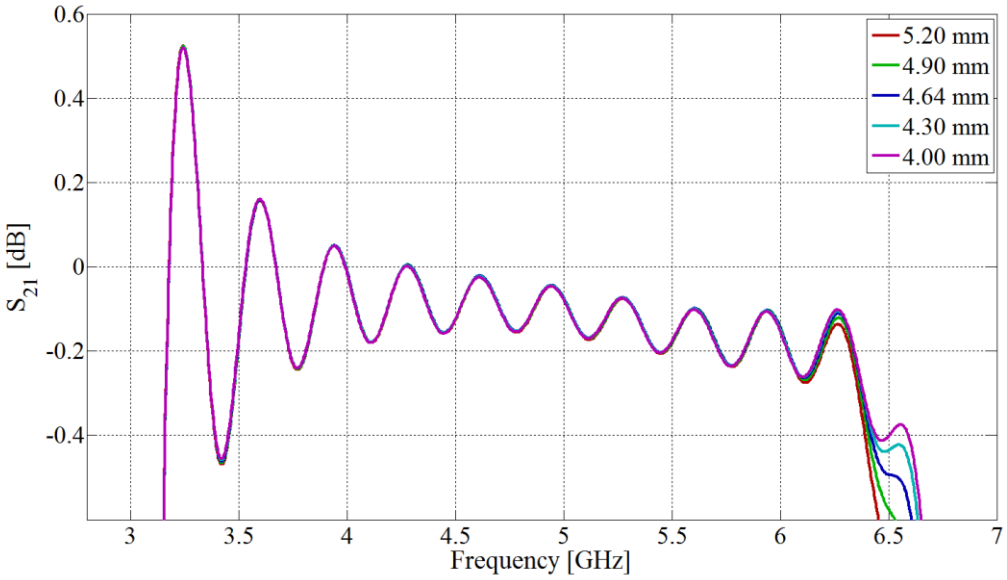

Figure 4.64. Simulated transmission coefficient for different post cut-out depths.

4.3.15 Post cut-out width

The post cut-out width is defined as the width of the notch around the post as shown in figure 4.65. The same physical constraint of 1.60 mm for the minimum acceptable cut-out width was selected as in the coaxial case to ensure that manufacturing tolerance concerns were minimal.

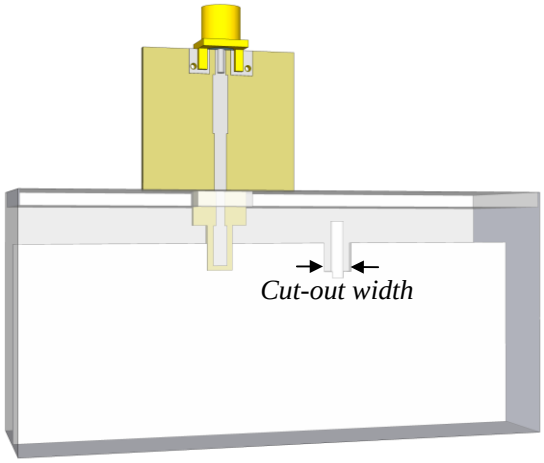

Figure 4.65. Post cut-out width definition.

Figure 4.66 below gives the input impedance for different cut-out widths around the post. The input impedance appears to be highly insensitive to variations in the post cut-out width.

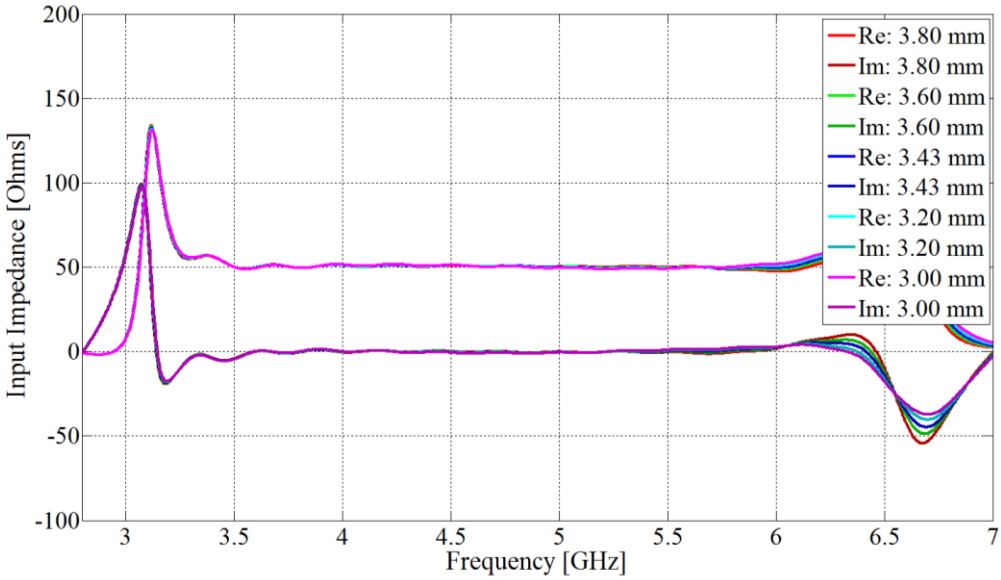

Figure 4.66. Complex input impedance for different post cut-out widths.

The reflection coefficient for the various post cut-out widths are given in figure 4.67 and also confirm that this parameter is highly insensitive to variations.

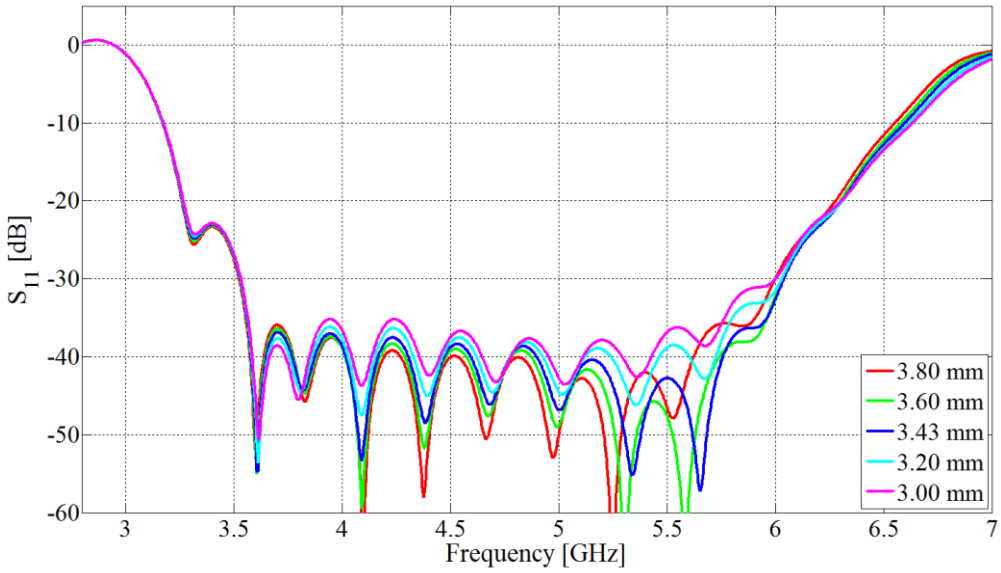

Figure 4.67. Simulated reflection coefficient for different post cut-out widths.

Figure 4.68 shows the effect of different post cut-out widths on the simulated insertion loss.

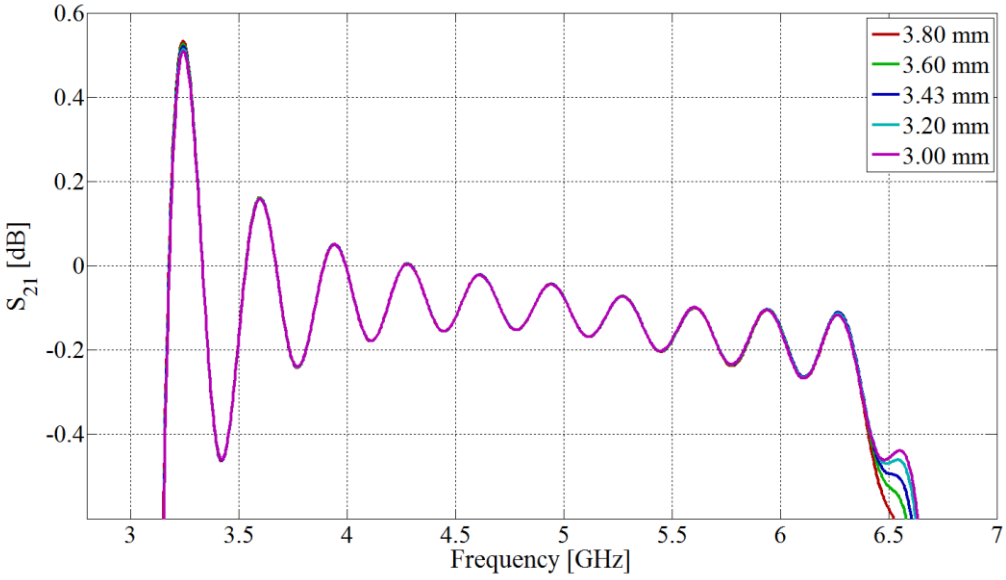

Figure 4.68. Simulated transmission coefficient for different post cut-out widths.

Note that hardly any deviation is visible in the figure above, confirming that this parameter is highly insensitive and it is the least sensitive parameter in this design.

4.3.16 Post diameter

The post diameter dimension is simply the diameter of the rod that forms the tuning post as shown in figure 4.69.

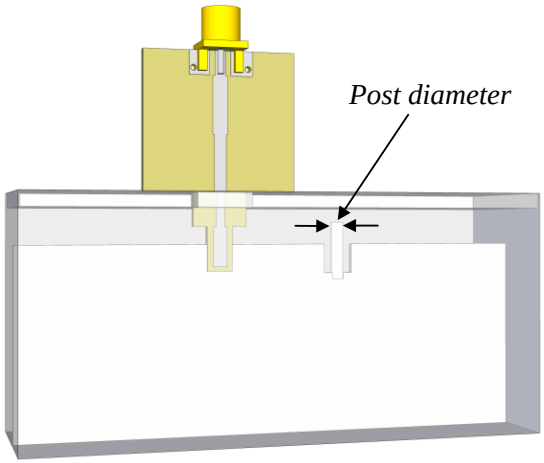

Figure 4.69. Post diameter dimension definition.

Figure 4.70 gives the simulated input impedance for the various post diameters.

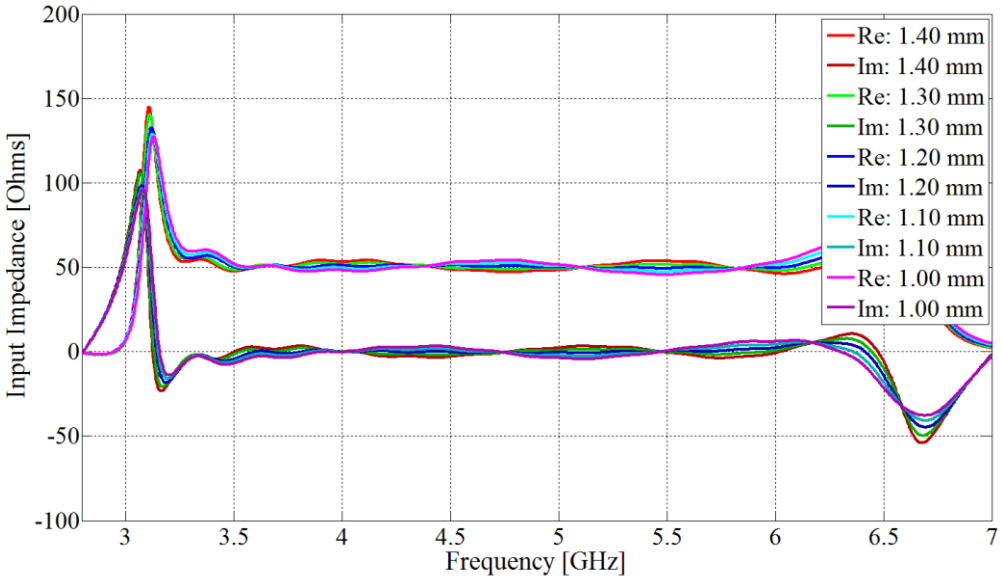

Figure 4.70. Complex input impedance for different post diameters.

Note that the post diameter parameter appears to be fairly sensitive from the input impedance figure above and the following reflection coefficient results in figure 4.71.

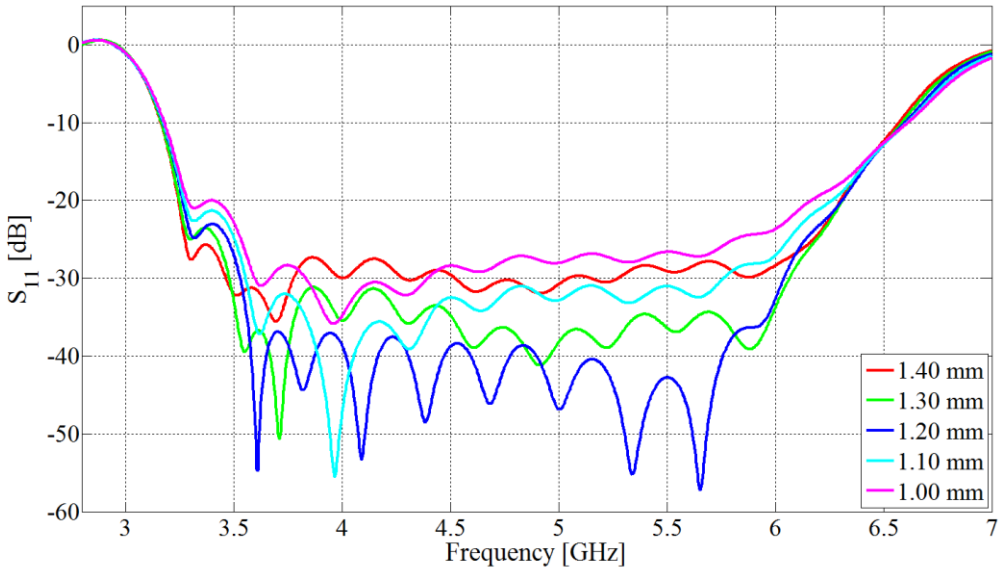

Figure 4.71. Simulated reflection coefficient for different post diameters.

Note that the higher frequencies appear to be more effected by the different post diameter values. Figure 4.72 shows the effect of different post diameters on the simulated insertion loss.

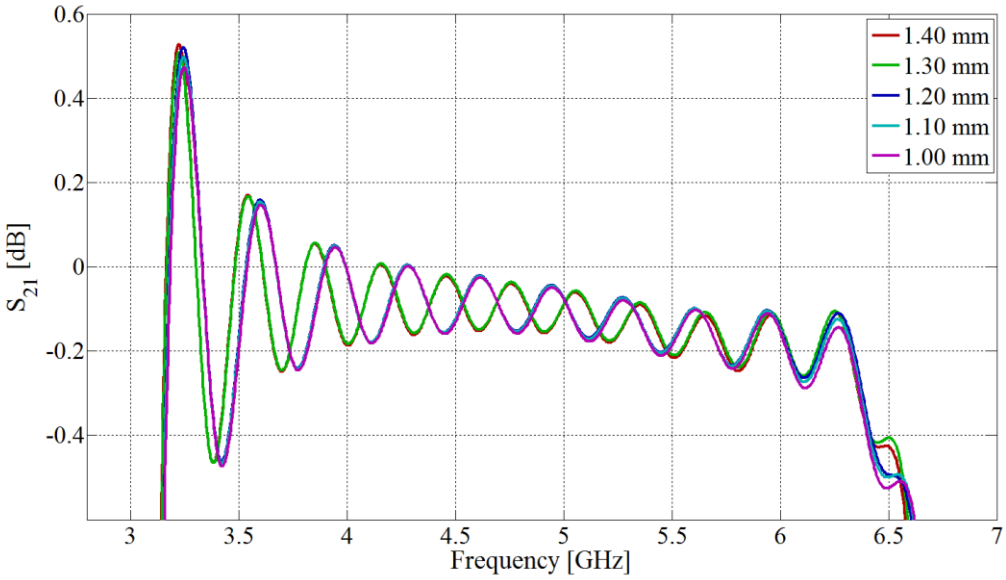

Figure 4.72. Simulated transmission coefficient for different post diameters.

4.3.17 Post end gap

The distance between the end of the post and the waveguide's side wall is defined as post end gap dimension as shown in figure 4.73. The same 0.5 mm constraint was used as in the development of the end-launched coaxial adapter.

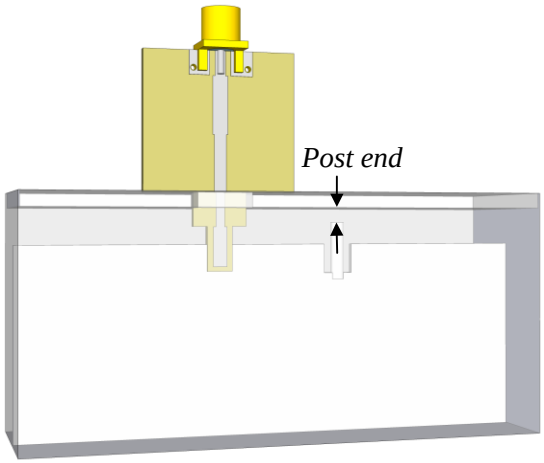

Figure 4.73. Post end gap dimension definition.

Figure 4.74 below gives the input impedance for the various post end gap sizes.

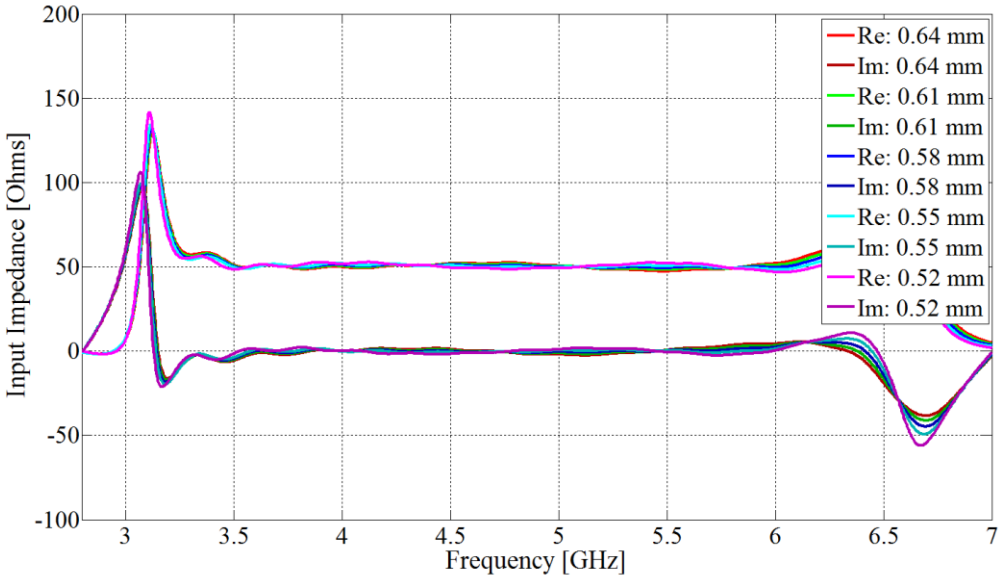

Figure 4.74. Complex input impedance for different post end gap sizes.

Note that the input impedance appears to be fairly insensitive to parameter variations. Figure 4.75 gives the simulated reflection coefficient for the different post end gap sizes.

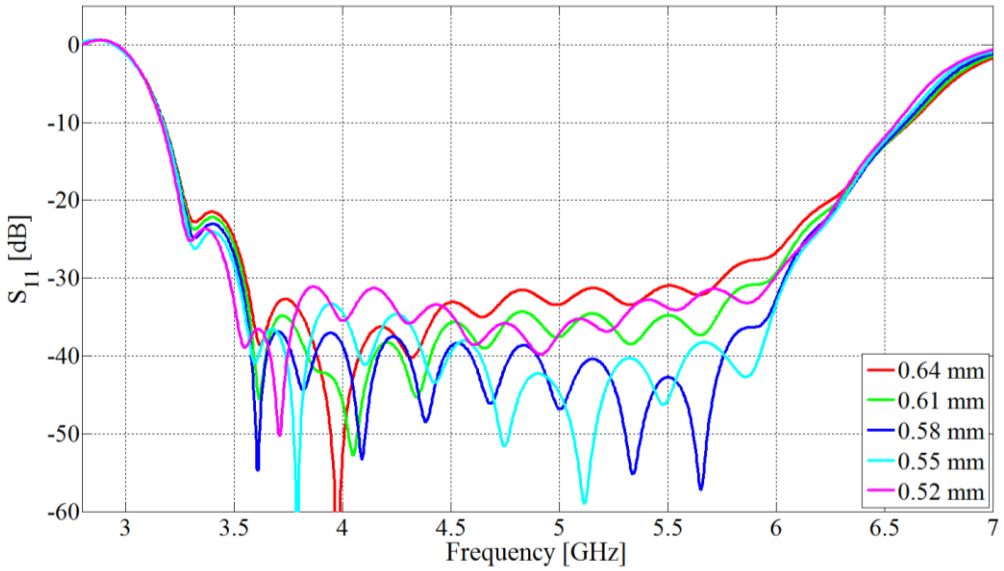

Figure 4.75. Simulated reflection coefficient for different post end gap sizes.

The simulated insertion loss for the various post end gaps are given below in figure 4.76. Note that the higher frequencies are more severely affected by parameter variations, than the lower frequencies.

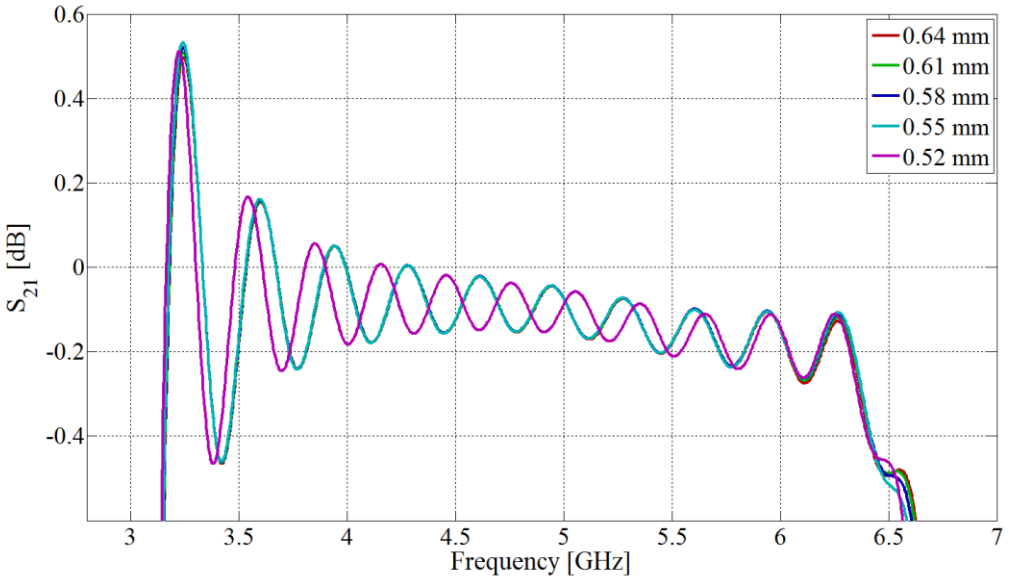

Figure 4.76. Simulated transmission coefficient for different post end gap sizes.

4.3.18 Parametric study summary

Table 4.1 summarises the effect of the various parameters investigated.

Table 4.1. Parameter study summary.

Parameter	Optimum value [mm]	Sensitivity	Notes
Transmission line width	1.78	Moderate	More sensitive at lower frequencies.
Matching length	5.61	Insensitive	Longer sections decrease return losses at mid band.
Matching strip width	1.59	High	Sets the characteristic impedance of the matching section.
Feed-line microstrip width	0.80	Extreme	Most sensitive parameter.
Feed-line gap width	3.59	Insensitive	Width of air gap in the side wall.
Microstrip air gap	2.00	Insensitive	Height of air gap in the side wall.
Feed-line end	2.80	Insensitive	Changes cause absolute phase shifts.
Probe position	19.35	Extreme	Probe position influences the major resonance frequency of the structure
Probe cut-out depth	3.03	High	The cut-out depth sets the length of the probe, which also influences the probe's resonant frequency.
Probe cut-out width	1.93	Moderate	More sensitive at lower frequencies.
Microstrip probe width	1.19	Moderate	Can differ from post diameter, unlike coaxial prototype's design goal .
Post position	28.90	Moderate	Post position influences post resonant frequency.
Post cut-out depth	4.64	Moderate	The cut-out depth sets the length of the post, which also influences the post's resonant frequency.
Post cut-out width	3.43	Insensitive	Least sensitive parameter.
Post diameter	1.20	Moderate	Higher frequencies are more sensitive.
Post end gap	0.58	Moderate	Higher frequencies are more sensitive.

4.4 PROTOTYPE REALISATION

This section describes the process followed to realise the prototype microstrip to partial H-plane waveguide adapter. The purpose of realising the prototypes in hardware is to facilitate measurements to confirm the simulation results. As in the coaxial prototype the microstrip prototype was realised with two adapters in the back-to-back configuration, to facilitate measurements of both the insertion and return losses. The same 6 mm wall and 1 mm vane thicknesses were used in the microstrip and coaxial prototypes. Figure 4.77 below shows a three-dimensional model of the microstrip prototype.

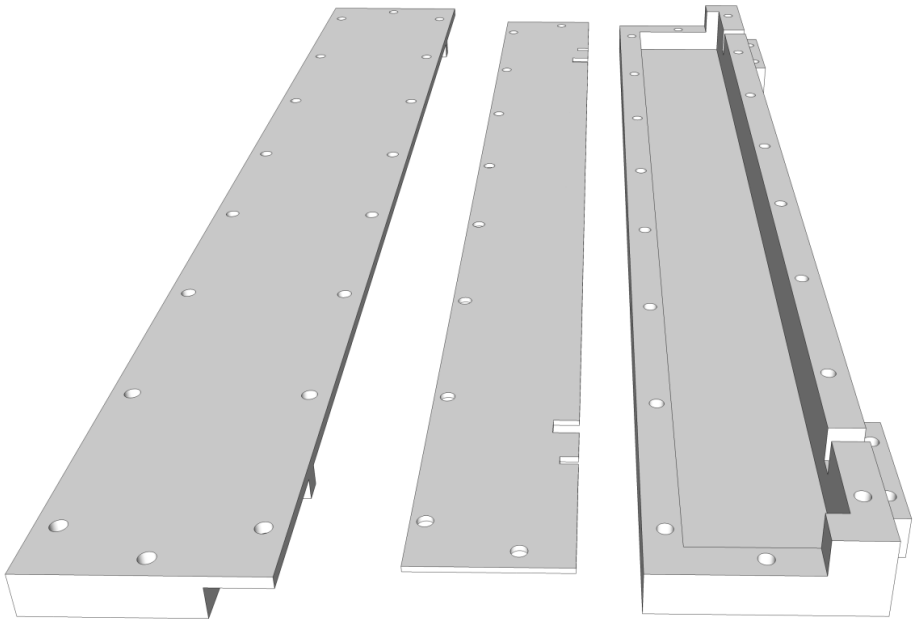

Figure 4.77. CAD model of microstrip prototype's waveguide.

Figure 4.77 shows from left to right, the top cover, H-plane vane and bottom cover. Note that there are two keys on the top cover that extend into the slots cut for the microstrip feed-line to pass into the waveguide in the bottom cover. These keys set the air gap height discussed in section 4.3.7. The microstrip PCB is attached with bolts to the flange that extends beyond the feed-line slot. The length of the partial H-plane waveguide that separates the two prototype adapters was again selected as 237 mm to achieve the desired two guided wavelength separation.

The microstrip printed circuit board artwork is given below in figure 4.78 in a 1:1 scale. Note that the white coloured areas are the copper areas, whilst the black areas are etched away to expose the Rogers RO4003C substrate.

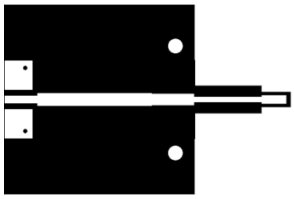

Figure 4.78. Microstrip adapter PCB artwork.

The two vias and reduced strip width at the location of the SMA connector (left hand side) are used to optimise the coaxial to microstrip transition as discussed in section 4.2.1, thereby reducing its effect on the measured results. Note that the difference between the strip widths of the transmission line and matching sections are hardly distinguishable but the width of the matching section is an extremely sensitive parameter as seen in table 4.1. Figure 4.79 below shows the internal structure of the fabricated microstrip prototype including the microstrip PCBs bolted into position.

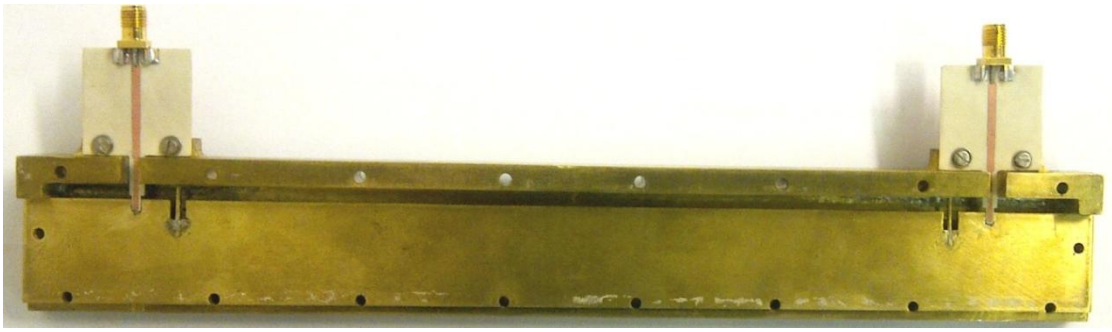

Figure 4.79. Photograph of the inside of the microstrip prototype.

Note that solder was used to attach the post to the H-plane vane, as in the case of the coaxial prototype. The exterior of the assembled prototype is shown in figure 4.80 below.

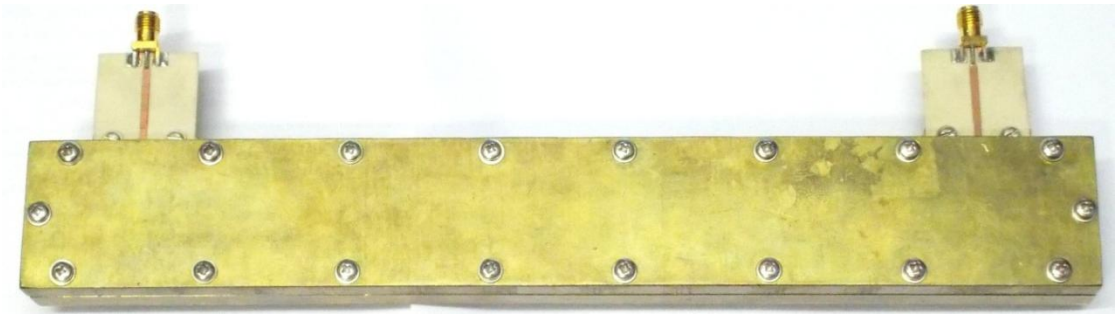

Figure 4.80. Photograph of the exterior of the completed microstrip prototype.

4.5 RESULTS

The results obtained through measurements of the realised microstrip prototype are documented in this section. Figure 4.81 shows the prototype connected to the Rohde & Schwarz ZVA40 vector network analyser.

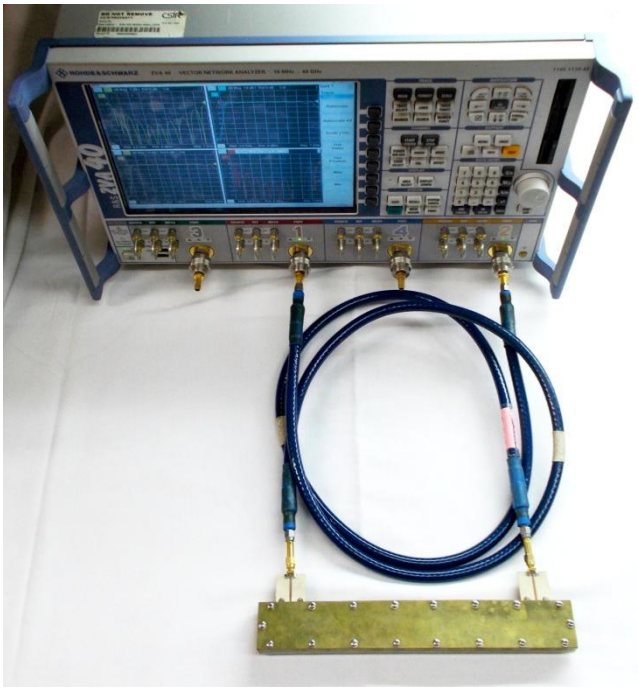

Figure 4.81. Microstrip prototype connected to the vector network analyser.

As with the measurements of the coaxial prototype, the instrument was calibrated using the automatic calibration method with the supplied two port calibration kit.

4.5.1 Back-to-back results

The two port measured results for the back-to-back configuration are given together with simulated results in figure 4.82. The bright solid lines are the measured results, whilst the dull dashed lines represent the simulated results.

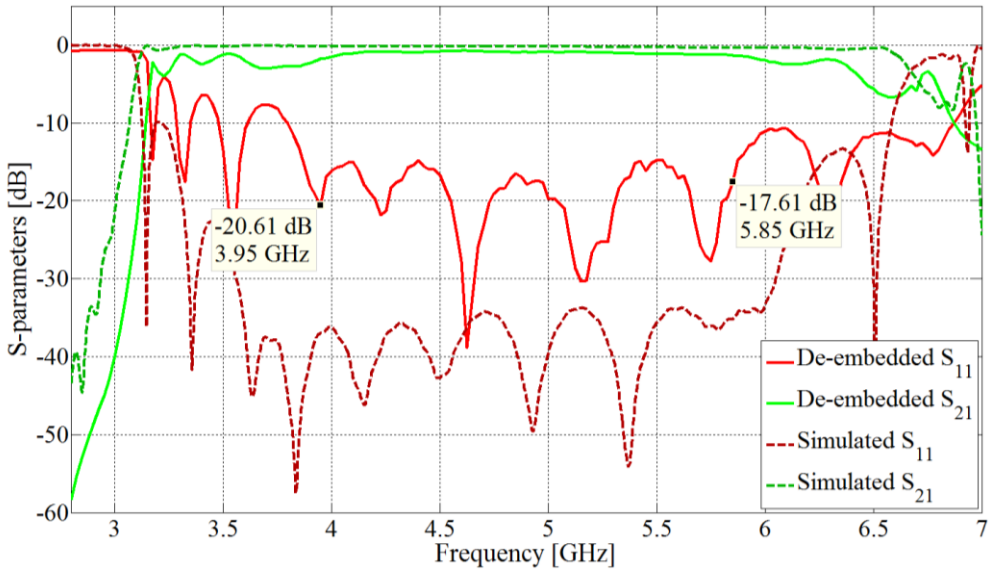

Figure 4.82. Two port back-to-back measured and simulated results.

The maximum measured reflection coefficient and insertion loss within H-band (3.95 to 5.85 GHz) are -15 dB and 1.7 dB respectively. The reason for the large difference between the insertion losses in the figure above is believed to be the result of a small air gap between the ground plane (formed by the waveguide's side wall) of the feed-line and the microstrip substrate inside the hole in waveguide's side wall as shown in figure 4.83.

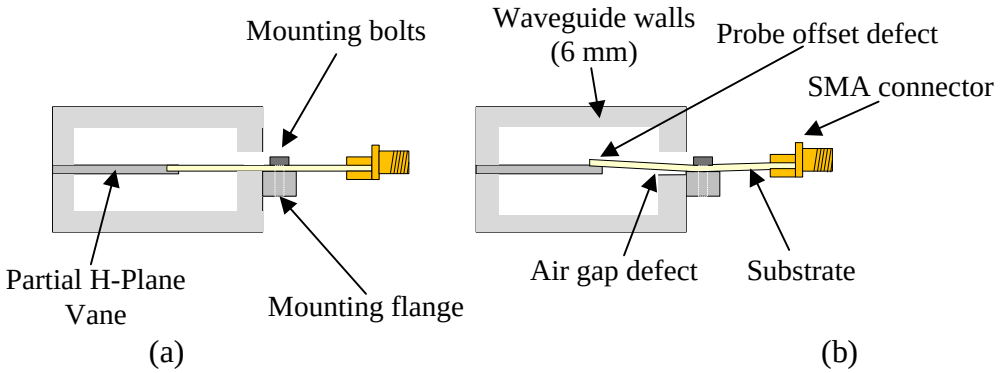

Figure 4.83. Cross-section of ideal (a) and realised (b) prototype waveguide transitions.

Note that in addition to the air gap in the figure above the probe part of the transaction is also slightly displaced in the vertical dimension. The figure above is exaggerated to illustrate the visible defect in the realised hardware and is not to scale.

4.5.2 Propagation constant used for de-embedding

The motivation for requiring knowledge of the propagation constant within the prototype waveguide was previously given in section 3.5.2. The simulated baseline and de-

embedding propagation constant are given in figure 4.84. Note that the de-embedding cut-off frequencies are above the simulated baseline cut-off frequencies in contrast to the coaxial case where the de-embedding cut-off frequencies were below the simulated ones.

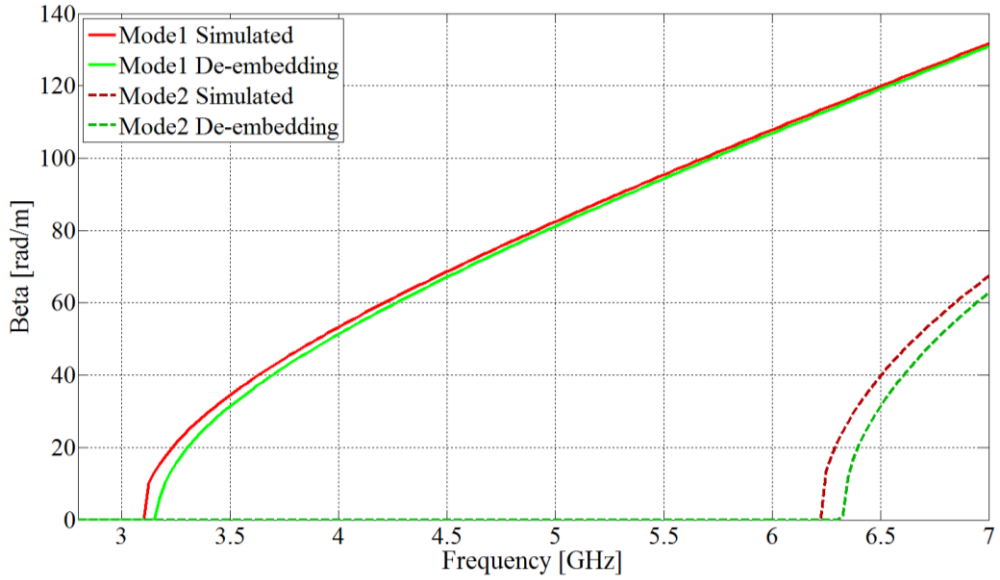

Figure 4.84. Initial simulated baseline and de-embedding propagation constants.

4.5.3 De-embedded single adapter results

The de-embedded approximate single adapter results are given below in figure 4.85.

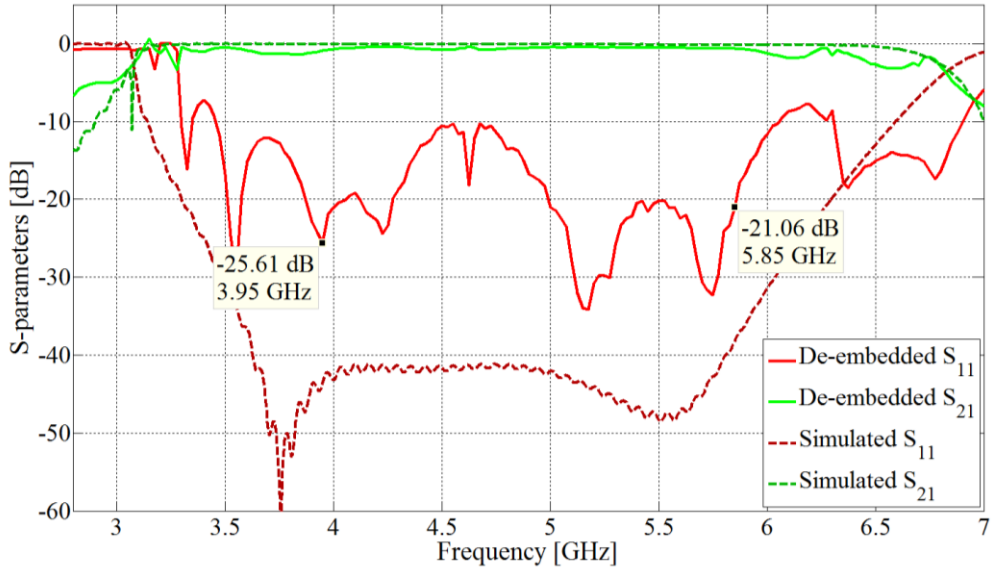

Figure 4.85. Measured and simulated single adapter S-parameters.

The maximum reflection coefficient within H-band is -10 dB and the maximum insertion loss is 0.88 dB.

The de-embedded approximate single adapter input impedance results are given below in figure 4.86. The red lines in the figure represent the real component of the input impedance and the green lines represent the imaginary component.

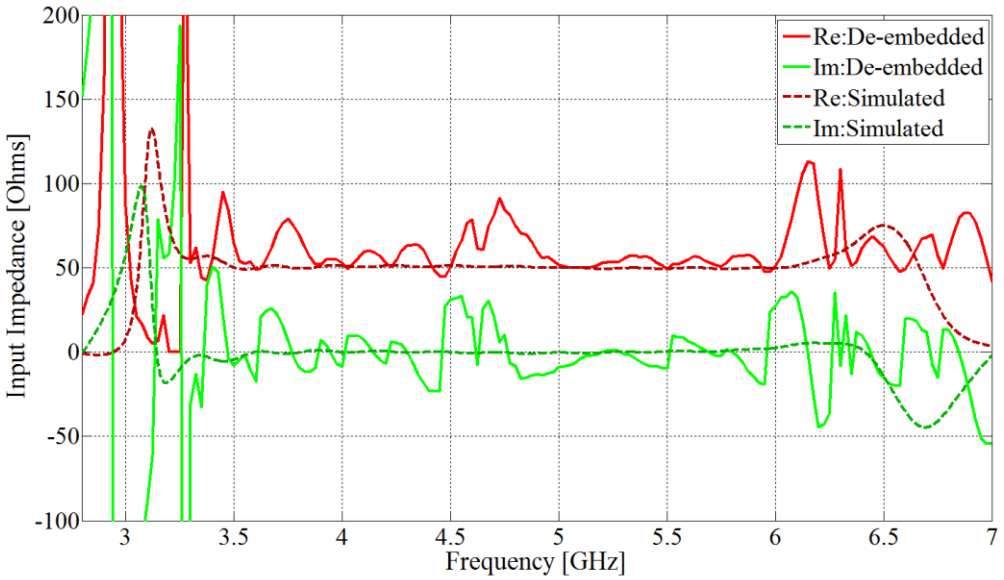

Figure 4.86. Measured and simulated single adapter input impedance.

Note that the real component of the de-embedded input impedance is too high (as in the coaxial case). The real component is approximately centred around 60 Ohms instead of the desired 50 Ohms. As previously mentioned the visible manufacturing defect as depicted in figure 4.83 is believed to be responsible for this offset and poor performance at mid band.

4.6 DISCUSSION

This chapter has documented the development of the microstrip to partial H-plane waveguide adapter from concept development through to measurements of the realised prototype. The concept development started off with a simple microstrip probe extending through an air gap into the waveguide above the H-plane vane, and evolved with the addition of a cut-out to increase the length of the probe. Furth additions of an impedance matching section and finally a tuning post to increase the simulated bandwidth to cover the entire band were added to the design. A parameter study was conducted to determine which parameters were the most sensitive and which parameters are insensitive. The parameter study concludes with a summary table which summarises the sensitivity of all of the parameters, with the feed-line width (microstrip section going through the side wall of the waveguide) and probe position being declared as the most sensitive parameters in the design. CAD design models, microstrip artwork and photographs of the realised prototype were given in section 4.4.

Lastly, the measured results obtained from laboratory measurements of the realised prototype are presented in section 4.5. Note that the microstrip prototype, similar to the coaxial prototype was realised in the back-to-back configuration to facilitate insertion and return loss measurements. The measured two port return and insertion losses are 15 dB and 1.7 dB respectively, note that these are the worst case results over the entire band. The higher insertion loss realised is due to a manufacturing defect as mentioned in section 4.5.1. Despite the simulated results being 33.7 dB and 0.35 dB respectively, the shape and values (to a lesser degree) of the measured results still compare favourably with the simulation results. The approximate single ended adapter response was obtained through de-embedding using the approximate propagation constant in section 4.5.2 and the assumption that the two realised transitions in the prototype are identical. The approximate singled adapter result has an insertion loss of 0.88 dB and a reflection coefficient of -10 dB, compared to the simulated values of 0.2 dB and -38.3 dB respectively. Despite the measured results not having the same fidelity as the simulated results due to manufacturing inaccuracies, the measured results still confirm that the design is functional.

CHAPTER 5 CONCLUSION

5.1 SUMMARY OF THE STUDY

This dissertation has reported on the development and testing of two prototype transitions to partial H-plane waveguide from coaxial and microstrip mediums. The motivation for the development of the prototypes is that only very limited information exists on how to feed the partial H-plane type of compact waveguide. The spiral development process was followed with the two concept waveguide adapters until they achieved the design goals of an insertion and return loss of better than 0.5 dB and 20 dB respectively, over the entire H-band (3.95 to 5.85 GHz). Two prototypes were realised in hardware to facilitate measurements of both the coaxial and microstrip designs.

5.2 SUMMARY OF RESULTS AND CONCLUSIONS

The results obtained with the coaxial and microstrip prototypes were discussed in sections 3.6 and 4.6 respectively. The measured results had higher insertion losses and significantly larger reflection coefficients than the simulated results. Despite this the shape of the measured results compared favourably with the simulated results. Therefore, although not ideal the measured results still confirm that both the designs are functional. The differences between the simulated and measured results are largely attributed to manufacturing tolerances and defects. The use of solder joints are believed to be the main cause of inaccuracies in the assembled prototypes. Since the achieved results in simulation and measurements cover the entire band, they still represent a useful contribution to the field as the previously existing transitions discussed in the literature study were designed for narrow band applications. Additionally the measured reflection coefficients are comparable or better than the previously existing partial H-plane adapters.

5.3 SUGGESTIONS FOR FUTURE RESEARCH

5.3.1 Improved external tuning

The current prototypes have to be disassembled and reassembled whilst tuning the internal components; therefore a method for external tuning would greatly improve tuning results

and significantly decrease the time required to tune the final manufactured transition. One such method would be to realise the post in the format of a tuning screw, whose length can be adjusted through a small hole in the side wall above the post. Additionally, given that the width of the air gap and probe cut-out width are fairly insensitive and that the probe position is the most sensitive parameter, the gap and cut-out width could be made a slightly wider than required to allow for post-production tuning of the microstrip probe's position.

5.3.2 Dielectric loading

The overall size of the partial H-plane waveguide could be further reduced if the waveguide was dielectrically loaded. This is similar to the substrate integrated folded waveguides mentioned in the literature study; however lower frequency waveguides could be fabricated where available substrate thicknesses are a limiting factor.

5.3.3 Phased array antenna

Given that the partial H-plane waveguide has previously been used to implement slot array antennas, a one dimensional phased array antenna with element spacing below one half wavelength spacing should be possible. With the end launched transition, the radiating face would be free of the connector obstruction that the previous antennas experienced.

5.3.4 Single substrate vane and transition

For some filter applications the transitions and vane could be etched as a single microstrip PCB, where the vane is formed from a double sided section of the board with vias along the leading edge of the vane. This would significantly reduce the chance of manufacturing errors.

5.3.5 Embedded active components

Given that the vane can be thicker than the current 1mm thickness (see section 3.3.1), other microwave components could be embedded within the vane, such as active components. An additional advantage of this approach is that the metal waveguide can act as a heat sink whilst significantly reducing the total size of a design, where filters can contribute largely to the overall size.

REFERENCES

[1] D.M. Pozar, *Microwave Engineering*, 3rd ed., John Wiley & Sons, Inc., New Jersey, USA, pp. 106-209, 2005.

[2] D.W. Kim and J.H. Lee, "A partial H-plane waveguide as a new type of compact waveguide," *Microwave and Optical Technology Letters*, Vol. 43, No. 5, pp. 426-428, Dec. 2004.

[3] D.W. Kim and J.H. Lee, "Partial H-Plane Filters with Partially Inserted H-Plane Metal Vane," *IEEE Microwave and Wireless Components Letters*, Vol. 15, No. 5, pp. 351-353, May. 2005.

[4] Z. Wang, D. Shen, R. Xu, B. Yan, W. Lin, Y. Guo, and X. Xie, "Partial H-Plane Bandpass Filters Based on Substrate Integrated Folded Waveguide (SIFW)," in *Asia Pacific Microwave Conference, APMC 2009*, pp.2545-2548, Dec. 2009.

[5] N. Grigoropoulos, B.S. Izqueirdo, and P.R. Young, "Substrate Integrated Folded Waveguides (SIFW) and Filters," *IEEE Microwave and Wireless Components Letters*, Vol. 15, No. 12, pp. 829-831, Dec. 2005.

[6] Y. Rong and K.A.Zaki, "Characteristics of Generalized Rectangular and Circular Ridge Waveguides," *IEEE Transactions on Microwave Theory and Techniques*, Vol. 48, No. 2, pp. 258-264, Feb. 2000.

[7] B. Sanz Izqueirdo, N. Grigoropoulos, and P.R. Young, "Ultra-Wideband Multilayer Substrate Integrated Folded Waveguides," in *Microwave Symposium Digest, 2006. IEEE MTT-S International*, pp. 610-612, June 2006.

[8] R. Rezaiesarlak, E. Mehrshahi, and M. Gharib, "Dispersion Characteristics of Partial H-Plane Waveguides," *Progress In Electromagnetics Research Letters*, Vol. 24, pp. 51-58, 2011.

[9] D.J. Kim, J.G. Lee, K.D. Kim, and J.H. Lee, "Quarter Wavelength Resonator Partial H-plane Filter," in *36th European Microwave Conference, 2006*, pp. 991-991, Sept. 2006.

[10] D.W. Kim, D.J. Kim, and J.H. Lee, "Compact Partial H-Plane Filters," *IEEE Transactions on Microwave Theory and Techniques*, Vol. 54, No. 11, pp. 3923-3929, Nov. 2006.

[11] D.J. Kim and J.H. Lee, "Partial H-plane filter with attenuation pole," in *IEEE Antennas and Propagation Society International Symposium 2007*, pp. 4260-4263, June. 2007.

[12] D.J. Kim and J.H. Lee, "Partial H-Plane Filters With Multiple Transmission Zeros," *IEEE Transactions on Microwave Theory and Techniques*, Vol. 56, No. 7, pp. 1693-1698, July 2008.

[13] L.S. Wu, X.L. Zhou, and W.Y. Yin, "A Novel Multilayer Partial H-Plane Filter Implemented With Folded Substrate Integrated Waveguide (FSIW)," *IEEE Microwave and Wireless Components Letters*, Vol. 19, No. 8, pp. 494-496, Aug. 2009.

[14] D.J. Kim and J.H. Lee, "Slot Array Antenna using Partial H-Plane Waveguide," in *IEEE Antennas and Propagation Society International Symposium 2009*, APSURSI'09, pp. 1-4, June 2009.

[15] D.J. Kim and J.H. Lee, "Resonant array antenna using inclined sidewall slot in partial h-plane waveguide," in *34th International Conference on Infrared, Millimeter, and Terahertz Waves, IRMMW-THz 2009*, pp. 1-2, Sept. 2009.

[16] D.J. Kim and J.H. Lee, "Compact Resonant Slot Array Antenna Using Partial H-Plane Waveguide," *IEEE Antennas and Wireless Propagation Letters*, Vol. 9, pp. 530-533, 2010.

[17] Z.G. Wang, X.Q. Li, S.P. Zhou, B. Yan, and R.M. Xu, W.G. Lin, "Half Mode Substrate Integrated Folded Waveguide (HMSIFW) and Partial H-Plane Bandpass Filter," *Progress In Electromagnetics Research Letters*, Vol. 101, pp. 203-216, 2010.

[18] L.D. Simmons and F.L. Ace, *Electronics Technician: Volume 7 - Antennas and Wave Propagation*, NAVEDTRA 14092, Naval Education and Training Professional Development and Technology Center, USA, pp 3-18 to 3-21, Oct. 1995.

[19] R.E. Collin, *Field Theory of guided waves*, McGraw-Hill book Company, Inc., New York, USA, pp. 258-285, 1960.

[20] R.F. Harrington, *Time-Harmonic Electromagnetic Fields*, McGraw-Hill book Company, Inc., New York, USA, pp. 425-428, 1961.

[21] W.W. Mumford, "The Optimum Piston Position for Wide-Band Coaxial-to-Waveguide Transducers," *Proceedings of the I.R.E.*, Vol. 41, No. 2, pp. 256-261, Feb. 1953.

[22] M.E. Bialkowski, "Analysis of a Coaxial-to-waveguide Adapter Including a Discended Probe and a Tuning Post," *IEEE transactions on Microwave Theory and Techniques*, Vol. 43, No. 2, pp. 344-349, Feb. 1995.

[23] M. Hajian, D.P. Tran, and L.P. Ligthart, "Modelling the transition between a coaxial line and a flat rectangular Waveguide," in *Ninth International Conference on Antennas and Propagation*, Conf. Publ. No. 407, Vol. 1, pp. 269-272, April 1995.

[24] A. Liao, Q. Wang, B. Wang, and Z. Wang, "Broad-band Transition from a Coaxial-line to a Rectangular Waveguide with Reduced-height," in *International Conference on Microwave and Millimeter Wave Technology 2008*, ICMMT 2008, Vol. 1, pp. 333-334, April 2008.

[25] M.E. Bialkowski, "Analysis of a Coaxial-to-Waveguide Adaptor Incorporating a Dielectric Coated Probe," *IEEE Microwave and Guided Wave Letters*, Vol. 1, No. 8, pp. 211-214, Aug. 1991.

[26] A.M. Helaly and J.M. Jarem, "Input impedance of a probe excited semi-infinite rectangular waveguide with a tuning post," in *Twenty-Second South-eastern Symposium on System Theory*, pp. 161-167, Mar. 1990.

[27] D.K. Cheng, *Field and Wave Electromagnetics*, 2nd Ed., Addison-Wesley Publishing Company, Inc., Massachusetts, USA, pp. 497-561, 1989.

[28] V. Galdi, G. Gerini, M. Guglielmi, H.J. Visser, and F. D'Agostino, "CAD of Coaxially End-Fed Waveguide Phased-Array Antennas," *Microwave and Optical Technology Letters*, Vol. 34, No. 4, pp. 276-281 , Aug. 2002.

[29] G.J. Wheeler, "Broadband waveguide-to-coax transitions," *IRE International Convention Record*, Vol. 5, pp. 182-185, Mar. 1957.

[30] S.M. Saad, "A More Accurate Analysis and Design of Coaxial-to-Rectangular Waveguide End Launcher," *IEEE Transactions on Microwave Theory and Techniques*, Vol. 38, No. 2, pp. 129-134, Feb. 1990.

[31] R.M. Chisholm, "The Characteristic Impedance of Trough and Slab Lines," *IRE transactions on Microwave Theory and Techniques*, Vol. 4, No, 3, pp. 166-172, July 1956.

[32] B.N. Das and G.S. Sanyal, " Coaxial-to-waveguide transition (end-launcher type)," *Proceedings of the Institution of Electrical Engineers*, Vol. 123, No. 10, pp. 984-986, Oct. 1976.

[33] M.D. Deshpande, B.N. Das, and G.S. Sanyal, "Analysis of an End Launcher for an X-band Rectangular Waveguide," *IEEE Transactions on Microwave Theory and Techniques*, Vol. 27, No. 8, pp. 731-735, Aug. 1979.

[34] M. Simeoni, C.I. Coman, and I.E. Lager, "Compact Colinear end-launcher for rectangular waveguides," in *IEEE MTT-S 2005 International Microwave Symposium Digest*, pp. 1199-1202, June 2005.

[35] W.L. Stutzman and G.A. Thiele, *Antenna Theory and Design*, 2nd Ed., John Wiley & Sons, Inc., New Jersey, USA, pp. 210-216, 1998.

[36] K. Wang, Z. Chen, Y. Zhou, and J. Hao, "A novel coaxial probe waveguide to microstrip transition," in *APMC 2005 Microwave Conference Proceedings*, Vol. 1, pp. 1-3, Dec, 2005.

[37] K. Ogawa, T. Ishizaki, K. Hashimoto, M. Sakakura, and T. Uwano, "A 50 GHz GaAs FET MIC Transmitter/Receiver Using Hermetic Miniature Probe Transitions," *IEEE Transactions on Microwave Theory and Techniques*, Vol. 37, No. 9, pp. 1434-1440, Sept 1989.

[38] Y.C. Shih, T.N. Ton, and L.Q. Bui, "Waveguide-To-Microstrip Transition for Millimeter-Wave Applications," in *IEEE MTT-S 1988 International Microwave Symposium Digest*, Vol. 1, pp. 473-475, May 1988.

[39] W. Peng, Z. Yong, W.Z. Gang, S.S. Chun, and X.R. Min, "Waveguide to microstrip probe transition for millimetre wave applications using LTCC technology," in *APEMC 2010 Asia-Pacific Symposium on Electromagnetic Compatibility*, pp. 1387-1389, April 2010.

[40] J. Wang, W. Zhong, "Development of a Ka-band waveguide to microstrip transition," in *ICMMT 2012 International Conference on Microwave and Millimeter Wave Technology*, Vol. 2, pp. 1-4, May 2012.

[41] S.A. Schelkunoff, *Electromagnetic Waves*, D. Van Nostrand Company, Inc., New Jersey, USA, pp. 480-496 , 1960.

[42] H.W. Yao and K.A. Zaki, "Modelling of Generalized Coaxial Probes in Rectangular Waveguides," *IEEE transactions on Microwave Theory and Techniques*, Vol. 43, No. 12, pp. 2805-2810, Dec. 1995.

[43] Unknown Author, "CST Microwave Studio: Workflow & Solver Overview," *CST Studio Suite 2012*, Computer Simulation Technology AG, pp. 108, 2012.

[44] A.J. Lozano-Guerrero, F.J. Clemente-Fernández, J. Monzó-Cabrera, J.L. Pedreño-Molina, and A. Díaz-Morcillo, "Precise Evaluation of Coaxial to Waveguide Transitions by Means of Inverse Techniques," *IEEE transactions on Microwave Theory and Techniques*, Vol. 58, No. 1, pp. 229-235, Jan. 2010.

[45] R.F. Bauer and P. Penfield, "De-Embedding and Unterminating," *IEEE transactions on Microwave Theory and Techniques*, Vol. 22, No. 3, pp. 282-288, March 1974.

[46] M.N. Sadiku and C.M. Akujuobi, "S-Parameters for Three and Four Cascaded Two-Ports," in *IEEE SoutheastCon 2004 proceedings*, pp. 410-412, March 2004.

[47] S.M. Wentworth, *Fundamentals of Electromagnetics with Engineering Applications*, John Wiley & Sons, Inc., New Jersey, USA, pp. 510-511, 2005.

[48] D.A. Frickey, "Conversion Between S, Z, Y, h, ABCD, and T Parameters which are Valid for Complex Source and Load Impedances," *IEEE transactions on Microwave Theory and Techniques*, Vol. 42, No. 2, pp. 205-211, Feb. 1994.